Events with Isolated Leptons and Missing Transverse Momentum in e^+p Collisions at HERA

David Michael South

April 2003

THE UNIVERSITY
of MANCHESTER

High Energy Group
Department of Physics and Astronomy

A thesis submitted to The University of Manchester for the degree of Doctor of Philosophy in the Faculty of Science and Engineering

Contents

Abstract

A search for events containing isolated electrons or muons and missing transverse momentum has been performed on the complete HERA I e^+p data set, corresponding to an integrated luminosity of 104.7 pb^{-1}. The main Standard Model process expected to contribute to such events is the production of real W bosons with subsequent leptonic decay, with a small further contribution from Z° production. A series of background enriched selections are employed to enable improved rejection of background processes. The design of a new trigger for future use in this and other H1 analyses is also described.

A total of 18 events are observed in the data compared to an expectation of 12.43 ± 1.59, of which 9.24 ± 1.45 are due to signal processes. The observed excess is due to events at large values of hadronic transverse momentum. In this kinematic region, 10 events are observed compared to a total expectation of 2.89 ± 0.51, of which 2.49 ± 0.51 are due to signal processes. The total cross section for events containing isolated electrons or muons with missing transverse momentum is measured to be $0.308 \pm 0.098(\text{stat}) \pm 0.041(\text{sys})$ pb. At large hadronic transverse momentum the measured cross section exceeds the Standard Model prediction from signal processes.

No portion of the work referred to in this thesis has been submitted in support of an application for another degree or qualification of this or any other university or other institute of learning.

This work was supported financially by the Particle Physics and Astronomy Research Council (PPARC) between October 1999 and September 2002.

Dedicated to Vera Harrison, my grandmother

Chapter 1

Introduction

The HERA facility located at DESY in Hamburg is unique in that it is the only electron-proton collider in the world. Since 1992 the collision experiments H1 and ZEUS have recorded over 100 pb^{-1} of data, at a centre of mass energy of up to 319 GeV[1,2]. Through analysis of these data a deeper understanding of the structure of the proton has been made possible, across a larger kinematic region than previously available to fixed target experiments.

As well as the study of the proton structure, the accumulation of a large quantity of data has allowed rare processes to be examined. The study of events containing isolated charged leptons and large missing transverse momentum has been of interest throughout the past decade at HERA and is the subject of several H1 publications [1–4]. The Standard Model predicts that the majority of such events arise from the production of real $W^{\pm}$ bosons, proceeding via photoproduction, with subsequent leptonic decay. Previous analyses have focussed on this particular process [3].

The analysis presented in this thesis is extended to include all Standard Model processes producing isolated charged leptons and large missing transverse momen-

[1]From 1992 to 1997, the centre of mass energy was 301 GeV.
[2]Natural units are used throughout this thesis, i.e. $\hbar = c = 1$.

tum in the final state. However, due to the low cross section and branching ratios of such processes, only a handful of events are expected in the analysed data, which includes the full HERA I e^+p data sample. In order to obtain an understanding of the dominant background processes, a series of background "enriched" selections are also performed. Furthermore, a new calculation of the Standard Model W production cross section is included in the presented results.

This thesis is organised as follows. Chapter 2 contains an introduction to HERA and a description of the H1 detector. This is followed by a theoretical overview of HERA physics in chapter 3. The kinematics of ep scattering are first introduced, followed by a brief description of Deep Inelastic Scattering (DIS). The main part of this chapter is dedicated to the signal processes examined in this thesis, predominantly W production. Background processes are also examined. Chapter 4 describes the basic criteria applied to all subsequent selections employed in this analysis. The design of a new trigger for future use in this and other H1 analyses is described in chapter 5. Chapter 6 examines particle identification and introduces the kinematic variables used to perform the presented event selections. Background studies are presented in chapter 7. The final event selections are described in chapter 8 and the results are presented and discussed in chapter 9. A summary is given in chapter 10.

Chapter 2

The H1 Experiment at HERA

2.1 HERA

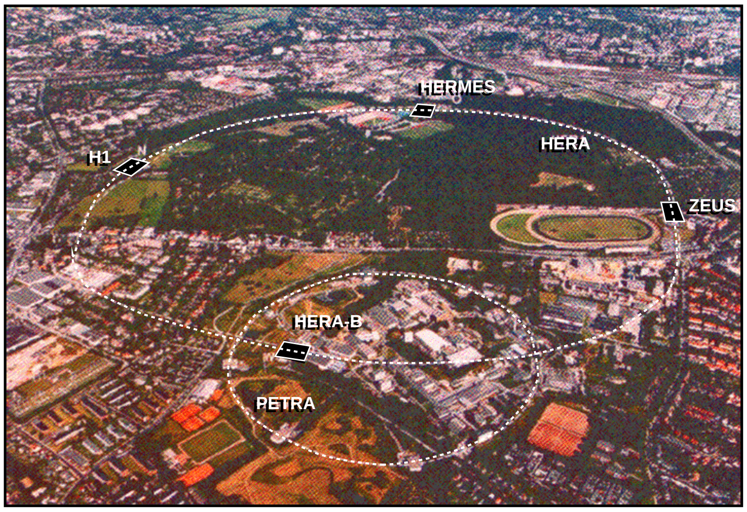

Figure 2.1: The HERA accelerator at DESY, showing the location of the four experiments.

The HERA particle accelerator is an integral part of the DESY (Deutsches Elektron Synchrotron) research centre in Hamburg, Germany. HERA (Hadron-Elektron-Ring-Anlage) is composed of two concentric, almost circular evacuated beam-pipes and is 6.3km in circumference. In one beam-pipe, protons are accelerated to an energy of 920 GeV[1] and in the other, electrons[2] are accelerated to 27.6 GeV. Beam currents are typically $\approx$ 30 mA and $\approx$ 80 mA for the electron and proton beams respectively.

The two counter-rotating beams intersect head-on at two points on the ring, where the *ep* collision experiments H1 and ZEUS are located. Two further experiments, HERMES and HERA-B each use only one of the HERA beams. The beams are accelerated as a series of short "bunches", crossing every 96 ns at the interaction points. Up to 220 bunches are stored in the two rings, although typically only 175 of them are used in collisions. The remaining non-colliding *pilot* bunches are employed to study background rates arising from interactions with residual beam-gas or the beam-pipe wall (see section 2.6). When the proton bunches are compressed by HERA small secondary or *satellite* bunches may be formed separated from the main bunch by up to 8 ns.

2.2 The H1 Detector

The H1 detector [5], illustrated in figure 2.2, is located within the North Hall of HERA. The detector measures approximately 12 m $\times$ 10 m $\times$ 15 m and weighs $\approx$ 2800 tonnes. It is described using a right handed cartesian coordinate system (x, y, z) with the nominal interaction point defined as the origin, $+x$ pointing towards the centre of the ring, $+y$ pointing vertically upwards and $+z$ in the direction of the incoming proton beam (also referred to as the "forward" direction). The corresponding spherical coordinate system (r, θ, ϕ) is defined so that $\theta = 0°$ is in the

[1] From 1992 to 1997, the proton beam energy was 820 GeV.

[2] HERA has mainly accelerated positrons since collisions began in 1992. Only in 1998 and the early part of 1999 were electrons used. For the remainder of this work, the term *electron* will be used to refer generically to the beam lepton, unless otherwise stated.

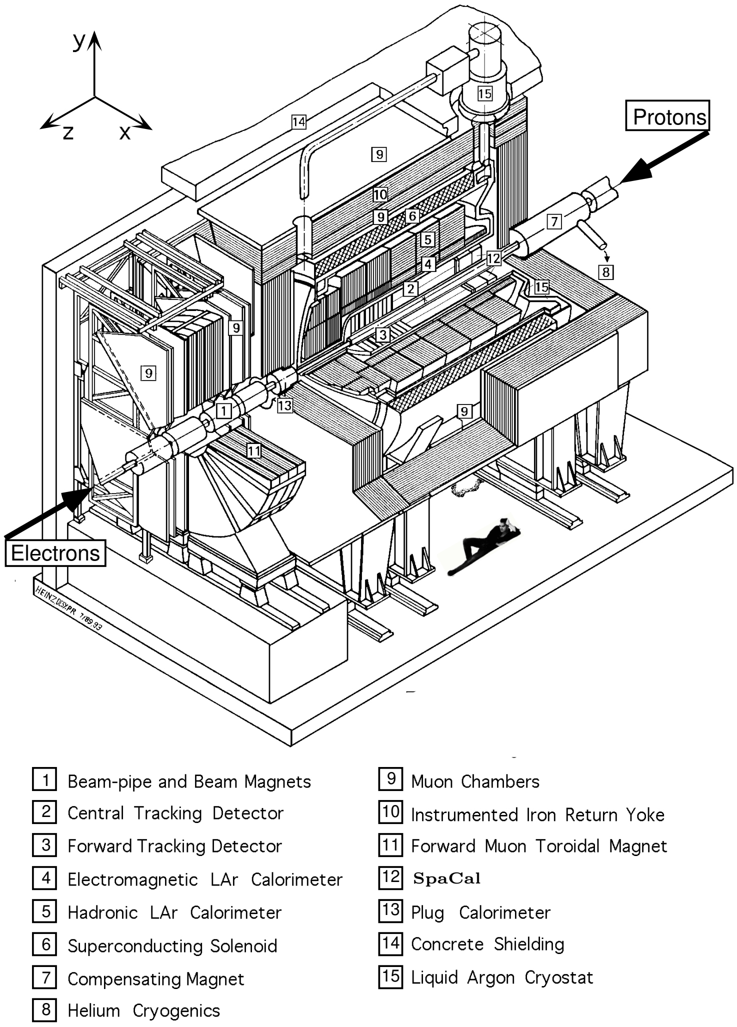

Figure 2.2: A schematic diagram of the H1 Detector.

proton direction and consequently $\theta = 180^{\circ}$ is in the electron ("backward") direction. The two beams are brought together by focussing magnets at the interaction point and the role of the detector is to record as much information as possible from the resulting collisions. The design of H1 has two striking features reflecting the nature of this role.

Firstly, almost complete coverage is achieved around the interaction point, the main limitation coming from the beam-pipe itself. This enables the particles produced from the ep interaction to be almost completely contained. This is important if the final state of a collision includes neutrinos, which are not directly detectable, and can only be inferred by a net transverse momentum imbalance.

Secondly, the design is very asymmetric reflecting the corresponding asymmetry in the beam energies. Due to the higher proton beam energy, most of the higher energy particles produced in a collision are boosted forward in the $+z$ direction. Hence the backward region is dedicated mainly to the detection of the scattered electron, whereas the larger number of detector components in the forward region and the deeper coverage provided correspond to the topology of a typical event.

The two main methods of particle detection employed by H1 are tracking and calorimetry. Surrounding the beam-pipe in a cylindrical arrangement are the tracking detectors (see section 2.3). These are contained in a magnetic field produced by a 1.15 T superconducting solenoid so that the momentum and charge of particles produced in collisions may be measured from the curvature of their tracks. Outside the trackers are the calorimeters, which absorb the energy of almost all incident particles (see section 2.4). A high level of granularity enables good position and energy resolution. The detector is then encased in a layer of instrumented iron to provide the return yoke for the magnetic field and further particle detection (see sections 2.4.4 and 2.5.1). A separate system for the detection of muons at low polar (θ) angles is situated outside the iron in the forward direction (see section 2.5.2).

The remainder of this chapter describes the individual detector components of H1 in 1999-2000, as the majority of the data presented in this thesis was taken in this running period.

2.3 Tracking

The measurement of the path (called the *track*) of charged particles through the H1 detector is made using three different detection methods. Drift chambers are used to provide accurate reconstruction and multiwire proportional chambers (MWPCs) provide a method of triggering because of their faster readout time. Silicon detectors are also employed to provide information on the primary vertex and track measurement at high polar angles.

Drift chambers are gas-filled cells, containing one or more anode *sense* wires and further *field* wires which form the cathode. A high voltage is applied to the cathode to create an almost uniform electric field within the volume of the cell except near the sense wires, where the field strength increases dramatically. When a charged particle passes through the chamber the gas is ionised; the positive ions "drift" towards the cathode and the electrons towards the anode wires. As the electrons approach the wire, the increased field strength induces secondary collisions with the gas atoms. This *avalanche* of collisions in the vicinity of the anode induces a current and a resulting pulse along the wire. The timing of this pulse, calculated using the known drift velocity within the cell, yields information about the original trajectory of the charged particle. The pulse is measured at both ends of the wire to determine the distance along the wire the particle crossed (the *charge division technique* [6]). These methods enable a 3D space point for the track to be calculated.

MWPCs are similar to drift chambers, except the anode wires are much closer together so that there are essentially no drift regions. This ensures any traversing charged particle will pass through a region of strong electric field, resulting in a fast particle multiplication process. Readout pads are located around the outside of the cell and form the cathode. The overlap of the avalanche regions of the wires results in a coarse spatial resolution, but due to the short drift time the hits can be readout in a time of $\mathcal{O}$(10ns), providing fast trigger information.

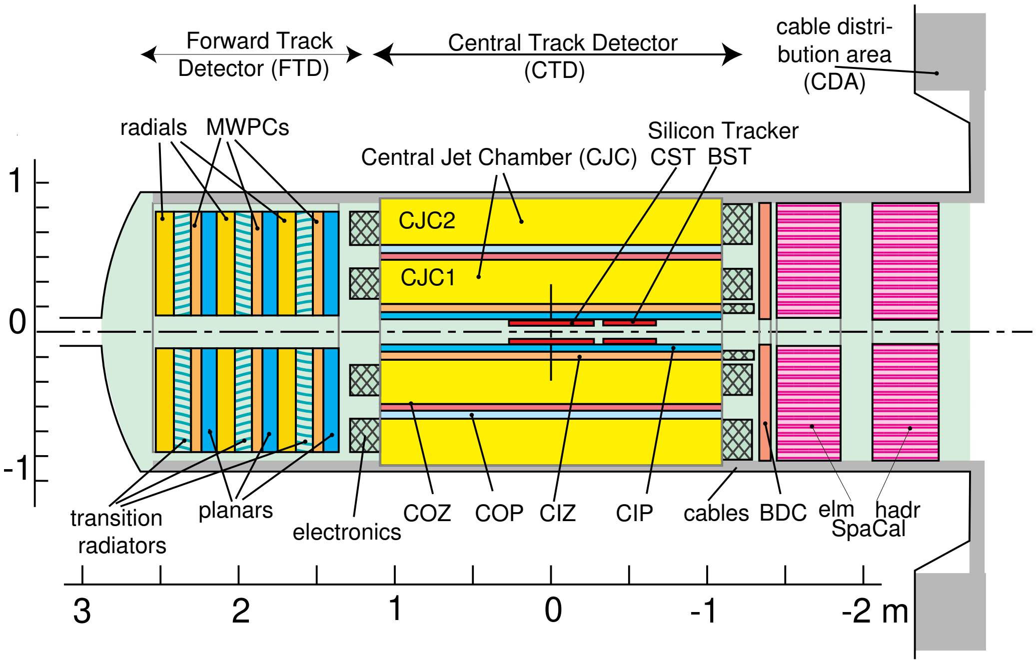

Figure 2.3: The H1 Tracking System.

The H1 tracking system is shown in figure 2.3 and covers the angular range $7° \leq \theta \leq 165°$. The whole system is contained within the magnetic field of the central solenoid, which is parallel to the z axis. This enables the momentum measurement of charged particle tracks due to the bending of the tracks under the influence of the magnetic field. The charge of the particle may also be ascertained from the direction of the curvature. Accurate measurement of the tracks in an event provides spatial information on the interaction vertex. The system is divided into two regions, the Central (CTD) (see section 2.3.1) and Forward (FTD) (see section 2.3.2) Track Detectors, both of which contain drift chambers and MWPCs. At the very centre of the detector are the Central (CST) and Backward (BST) Silicon Trackers. Additional track reconstruction is provided in the backward region by the Backward Drift Chamber (BDC) (see section 2.3.3).

2.3.1 The Central Track Detector

The CTD covers the range $15° \leq \theta \leq 165°$ and consists of many concentric parts, as illustrated in figure 2.4. Innermost is the central inner proportional chamber (CIP), followed by the central inner z chamber (CIZ). The two Central Jet Chambers (CJC1) and (CJC2) are divided by the central outer z chamber (COZ) and the central outer proportional chamber (COP). These detectors are described in the following.

The two main detectors in the CTD are the inner (CJC1) and outer (CJC2) central jet chambers [7]. The anode sense wires are strung parallel to the beam axis, resulting in excellent spatial resolution for track reconstruction in the r-ϕ plane. Limited resolution in the z plane is obtained by sampling the currents at both ends of the wires. The chambers are segmented in the ϕ plane into 30 cells in CJC1 and 60 cells in CJC2. In CJC1 (CJC2) there are 24 (32) sense wires in each cell, all tilted at an angle of $\approx 30°$ relative to the radial plane. This tilt ensures that even stiff (high momentum) tracks will cross a wire plane in one of the cells and the track crosses multiple cells to avoid spatial ambiguities.

To complement the Central Jet Chambers, the CIZ and COZ [8] located either side of CJC1, provide an accurate z coordinate measurement. In order to provide this information, the sense wires in these detectors are strung perpendicular to the beam axis. The r-ϕ plane of the CIZ takes the form of a 16 sided regular polygon, and is divided into 15 cells in the z direction, each cell containing 4 concentric sense wires. A low resolution spatial measurement in the r-ϕ plane using the central z chambers is also possible from the charge division technique. The COZ is of a similar design to the CIZ, except that it forms a 24 sided regular polygon in the r-ϕ plane, and is divided into 23 cells in z.

In order to trigger events at a high rate the design of the CTD includes two MWPCs, the CIP and the COP [9], positioned adjacent to the CIZ and the COZ.

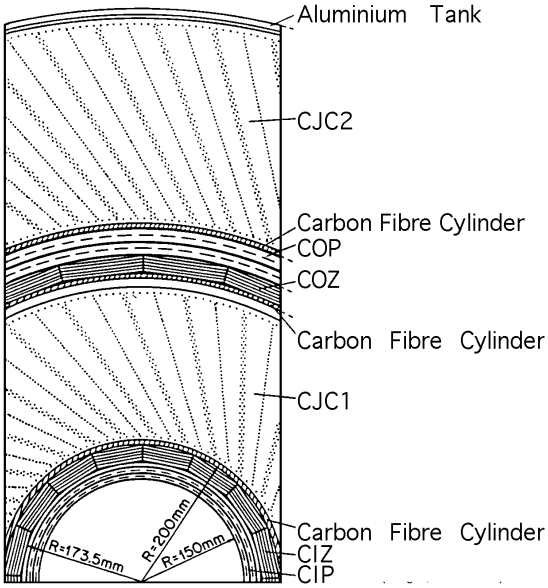

Figure 2.4: A cross sectional view of the Central Track Detector.

A double chamber design is employed with a $\frac{\pi}{16}$ rotation in ϕ with respect to each other. As in the central jet chambers the wires run parallel to the beam-pipe. The CIP is divided into 8 sections in ϕ each containing 60 wires per chamber. In the z direction there are 60 readout pads around the outside forming the cathode. The resulting timing resolution is faster than the time between two successive HERA bunch crossings. The COP is constructed in a similar way, except that there are 16 sections in ϕ each containing ≈ 100 wires, and each section is divided into 18 pads in z.

2.3.2 The Forward Track Detector

The FTD [10], pictured on the left hand side of figure 2.3, covers the angular range $7^\circ \leq \theta \leq 25^\circ$. It is composed of three identical *supermodules* as detailed in figure 2.5, each containing (in order of increasing z) Planar Drift Chambers, MWPCs, Transition Radiators and Radial Drift Chambers. All wires are strung perpendicular to the beam axis and are arranged in parallel.

In each supermodule there are three adjacent Planar Drift Chambers, each rotated by $\frac{\pi}{3}$ with respect to each other. Each chamber is made up of 32 parallel cells, each containing 4 wires. Signals are read out from one end only, hence only the drift coordinate is measured. The Forward MWPCs, located immediately after the Planars in each supermodule, provide fast triggering in the forward region. They consist of two wire planes, each containing 362 parallel wires and three interleaved cathode readout planes, arranged with a radial offset. The Transition Radiators provide the potential for particle identification, using specific ionisation (dE/dX) techniques. Finally, the Radial Drift Chambers are divided into 48 wedges in ϕ, each sector containing 12 parallel sense wires. Signals are read out at both ends, enabling the coordinate along the wire to be determined via charge division.

2.3.3 The Backward Drift Chamber

The BDC [11] is mounted on the inner side of the SpaCal[3] (see section 2.4.2) as shown on the right hand side of figure 2.3 and covers the angular range $155° \leq \theta \leq 177.5°$. It was installed after the 1995 upgrade[4], to provide accurate track reconstruction for electrons scattered through small angles. The detector is constructed from 8 layers in the z direction, each layer divided into octants and each octant containing 32 drift cells. Each cell contains 32 wires strung perpendicular to the beam axis to provide an accurate z coordinate measurement. The layers are arranged in pairs and each pair is rotated by $\frac{\pi}{16}$ with respect to the others.

[3] The name originates from the long thin scintillating fibres used as the active layer, hence "Spaghetti" Calorimeter.

[4] The BDC replaced the Backward Proportional Chamber (BPC), a description of which can be found in [5].

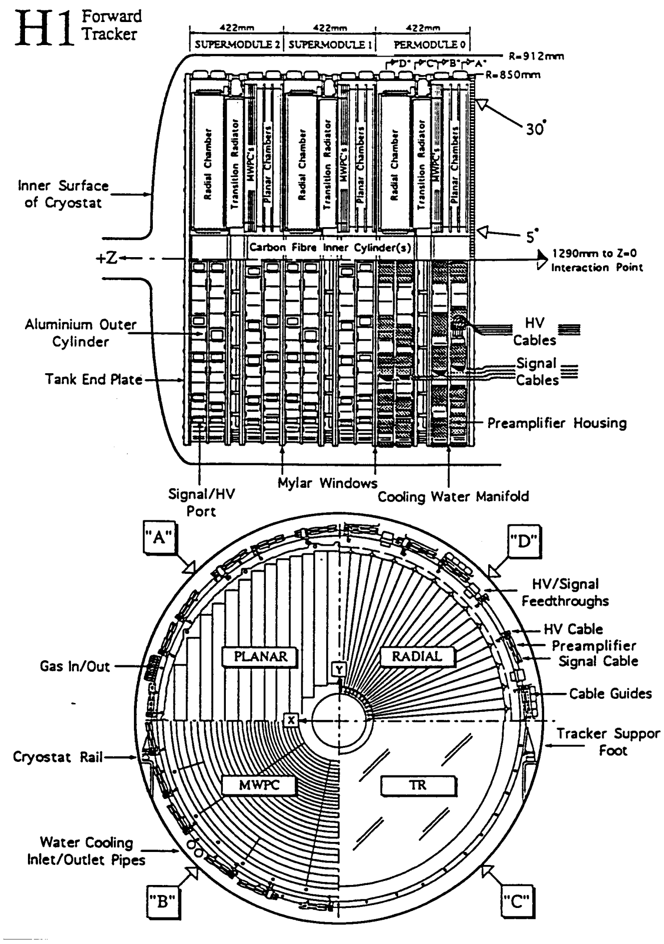

Figure 2.5: The Forward Track Detector. Top: The r-z plane, showing the structure of the supermodules. Bottom: The r-ϕ plane, showing the basic cell structure of each supermodule component.

2.4 Calorimetry

All of the calorimeters used within H1 rely on the same detection principle. Each detector consists of two main components: a series of absorbing (*passive*) layers interleaved with sampling (*active*) layers. High energy particles entering an absorbing layer undergo multiple interactions with the constituent atoms, resulting in the production of secondary particles. These in turn interact with the next absorbing layer, resulting in a shower of charged particles that continues into the active layers. This process carries on until all of the energy of the original incident particle is lost to the shower. Charged particles produced in the shower ionise the atoms of the sampling layer and the energy produced forms the signal that is read out. The energy of the readout signal is proportional to the energy of the original incident particle.

Electrons and photons lose energy in a calorimeter via electromagnetic interactions with the atomic nuclei in the absorbing layers. This occurs rapidly via the bremsstrahlung and pair-production processes. The resulting shower consists of electrons, positrons and photons. The longitudinal progress of an electromagnetic shower is characterised by the *radiation length* of the absorbing layer, X_o, which is the mean distance over which all but $\frac{1}{e}$ of the particle's initial energy is lost.

Hadrons interact strongly with the nuclei of the absorbing layers, elastically and inelastically, resulting in a shower composed of secondary hadrons. The characteristic length of a hadronic shower is given by the *interaction length* of the absorbing layer, λ_i. This is typically much larger than X_o for the same material and hence a hadronic shower will develop much more slowly. The energy contained within the shower consists of a prompt component formed from π^0 mesons produced in the nuclear interactions decaying to photon pairs, which then shower electromagnetically. The secondary charged hadrons (mainly $\pi^{\pm}$ mesons) also undergo Coulomb scattering in the absorber giving rise to a broader shower shape. These features make a hadronic shower topologically distinguishable from an electromagnetic shower. Furthermore, about 30% of the energy involved in the hadronic shower development is lost in nuclear excitation and breakup [12].

The calorimetry within H1 can be separated into 4 different detectors. The main calorimeter is the Liquid Argon Calorimeter (LAr), which covers the forward and central regions. This is complemented in the backward region by the SpaCal and in the very forward region by the Plug, which fills the gap between the LAr and the beam-pipe. Finally, the Tail-Catcher (TC) is situated within the the return yoke of the solenoid. These calorimeters give almost complete solid angle coverage and are described individually in the following sections.

2.4.1 The Liquid Argon Calorimeter

The LAr [13] is the main calorimeter in the H1 detector, with an angular range of $4° \leq \theta \leq 153°$ and complete coverage in ϕ. The main function of this calorimeter is to provide electron identification and detection of the hadronic final state. The LAr is composed of two sections, an electromagnetic calorimeter (EMC) and a hadronic calorimeter (HAC). The passive layers of the EMC are formed from 2.4mm thick lead plates, whereas the HAC uses 16mm thick plates of stainless steel. Liquid argon forms the common sampling layer for both the EMC and the HAC. Charged particles produced in the shower ionise the argon atoms and the resulting electrons are converted to a signal and read out. The LAr is a *non-compensating* calorimeter, resulting in a 30% loss of the initial hadronic energy to the showering process. To account for this, an offline software technique is employed [14].

The calorimeter is divided into several symmetric sections in z called "wheels", each of which is highly segmented, resulting in very fine granulation and 45000 individual readout channels. This granulation allows isolated, low energy deposits and noisy (hot) cells to be rejected. The sections are deeper in the forward region, the EMC and HAC being $\approx 30\ X_o$ and $\approx 8\ \lambda_i$ deep respectively, as events more commonly occur in the forward direction as described in section 2.2. In the backward region, these values fall to $\approx 20\ X_o$ (EMC) and $\approx 5\ \lambda_i$ (HAC). The readout channels are grouped together into 256 "towers", all with a common origin at the nominal interaction point. The energy in each tower is summed and used as the basis of the LAr trigger (see section 4.4.1).

The energy resolution of the LAr has been obtained using test beams. For electrons in the EMC it is found to be $\frac{\sigma_E}{E} = \frac{0.12}{\sqrt{E/GeV}} \oplus 0.01$ GeV [15] and for charged pions it is $\frac{\sigma_E}{E} = \frac{0.50}{\sqrt{E/GeV}} \oplus 0.02$ GeV [16] for both parts of the calorimeter.

(a)

(b)

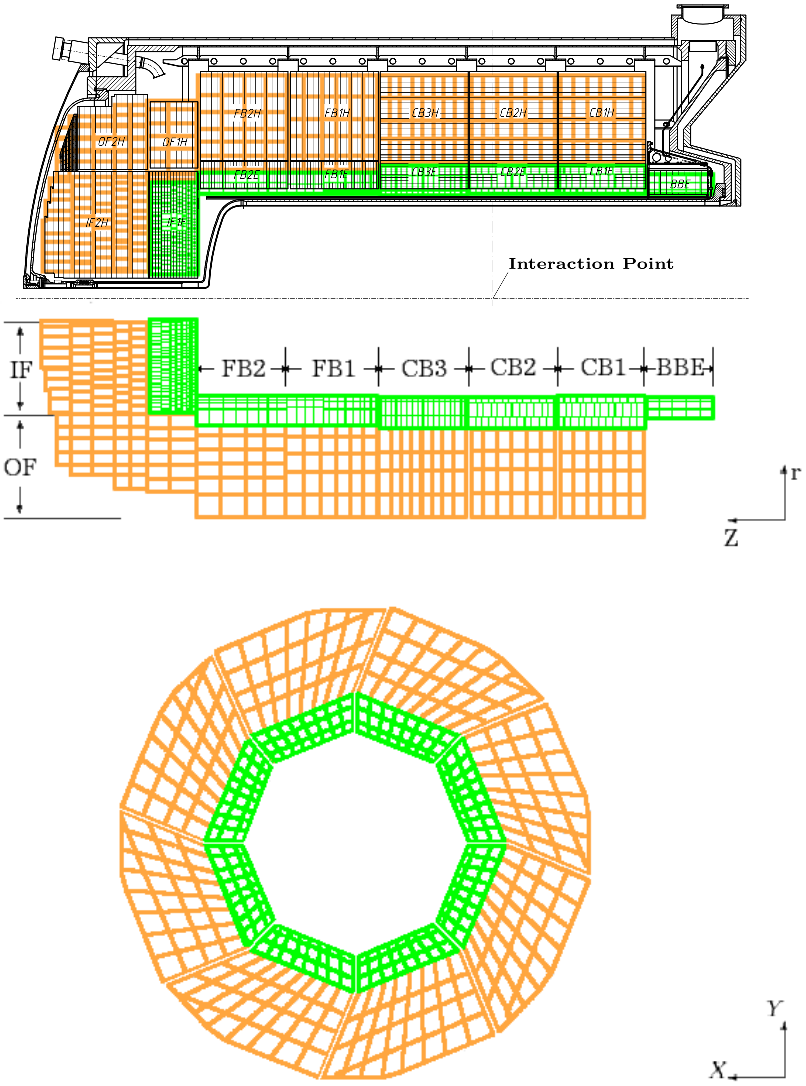

Figure 2.6: The Liquid Argon Calorimeter. (a) The r-z plane, (b) the x-y plane.

The LAr is illustrated in figure 2.6, where the EMC is coloured green and the HAC is coloured orange. An r-z projection is shown in part 2.6a. The top half of 2.6a details the individual plates in each section; in the central region the plates are parallel to the beam axis, whereas in the forward and backward region they are arranged in a perpendicular orientation. The bottom half of 2.6a displays the names of the wheels as IF (Inner Forward), OF (Outer Forward), FB (Forward Barrel) and CB (Central Barrel). The Backward region consists only of the BBE

(Backward Barrel Electromagnetic calorimeter) and has no corresponding hadronic section. Figure 2.6b shows a central wheel in the x-y plane.

2.4.2 The SpaCal

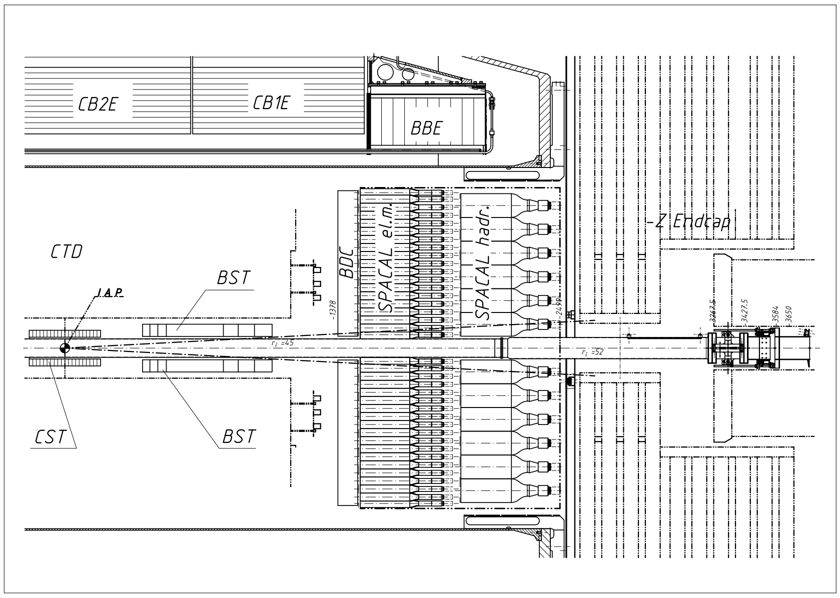

Figure 2.7: The location of the SpaCal in the backward region of H1.

The SpaCal[5] [17] provides calorimetric coverage in the backward region of H1 for the angular range $153° \leq \theta \leq 177.5°$, as shown in figure 2.7. Like the LAr, it is divided into electromagnetic and hadronic sections, although its primary function is the detection of electrons scattered through low angles. Both sections consist of scintillating fibres (the sampling material) embedded in a lead matrix absorber. Charged particles produced from showering in the lead cause the fibres to scintillate. The light produced in the fibres is carried via light guides to photomultipliers, where the signal is read out. The time resolution of the signal is of $\mathcal{O}(1\text{ns})$, allowing the SpaCal to be used for veto purposes (see section 2.6).

[5]The SpaCal replaced Backward Electromagnetic calorimeter (BEMC) after the 1995 upgrade, details of the BEMC can be found in [5].

The active regions in each section, which contain the sampling material, are both 250mm deep. In the electromagnetic section this corresponds to $\approx 28\ X_o$ or equivalently $\approx 1\ \lambda_i$. The fibres are 0.5mm in diameter and signals are read out from 1192 individual channels. The hadronic section provides a further interaction length and contains fibres of 1.0mm diameter. The hadronic signal is read out from 136 channels, reflecting the greater lateral extent of the showers.

The energy resolution of the SpaCal has been determined using test beams. The response to electrons is given by $\frac{\sigma_E}{E} = \frac{0.07}{\sqrt{E/GeV}} \oplus 0.01$ and $\frac{\sigma_E}{E} = \frac{0.13}{\sqrt{E/GeV}} \oplus 0.04$ for the electromagnetic [18] and hadronic [19] sections respectively. The hadronic resolution is determined using a charged pion beam and the resulting energy resolution for the combined response is $\frac{\sigma_E}{E} = 0.29 \pm 0.02$ [20].

2.4.3 The Plug Calorimeter

The Plug calorimeter [21] is positioned within the instrumented iron in the forward region (labelled 13 in figure 2.2). It covers the angular range from $0.75^\circ \leq \theta \leq 3.4^\circ$, in the gap between the LAr calorimeter and the beam pipe. The Plug is a silicon instrumented sandwich calorimeter and consists of eight passive layers of absorbing copper, interleaved by plane silicon detector modules. Each of the silicon planes consists of 84 mainly square (5cm $\times$ 5cm) detectors, which serve as the active layers and are read out in pairs. The energy resolution suffers from this course granularity and from shower leakage, resulting in a relatively poor resolution of $\frac{\sigma_E}{E} = \frac{1.5}{\sqrt{E/GeV}}$ [5].

2.4.4 The Tail Catcher

As previously stated in section 2.2, the iron layer (labelled 10 in figure 2.2) of the detector is instrumented to provide further particle detection. Contained within the iron are sixteen layers of limited streamer tubes (LST's) and the layout of one such layer is displayed in figure 2.8. Each of the LST's are filled with gas and contain a single sense wire running down the centre. A high voltage is applied across the individual cells.

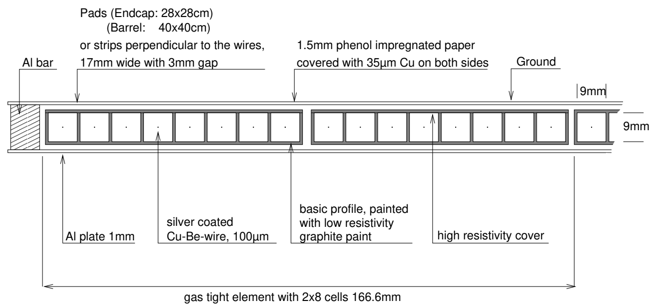

Figure 2.8: Cross-sectional structure of a layer of LST's.

Eleven of the layers are fitted with calorimetric readout pads, the iron itself acting as the absorbing material. The function of these detectors is to detect hadronic energy that leaks out of the LAr or SpaCal, hence the name "Tail Catcher" [22]. When a charged particle passes through the tube it causes a *streamer*, which produces a current in the readout pad. The energy resolution of the Tail Catcher is $\frac{\sigma_E}{E} = \frac{1.0}{\sqrt{E/GeV}}$ [5]. The remaining five layers are used for the detection of muons, detailed in section 2.5.1.

2.5 Muon Detection

Muons do not interact like hadrons via the strong force and do not radiate as much as electrons (via the bremsstrahlung process) due to their heavier mass. For these reasons they escape the main calorimeters and further detectors are required around the outside of H1. Two muon detection systems are used: the instrumented iron (labelled 10 in figure 2.2) for central muons, $6^\circ \leq \theta_\mu \leq 172^\circ$ and the forward muon system (labelled 9 in figure 2.2) for the range $3^\circ \leq \theta_\mu \leq 17^\circ$. These two systems are described in the following sections.

2.5.1 Central Muons

The detection of muons in the central region is achieved using up to five out of the sixteen layers of LST's [23] within the instrumented iron. These LST's are fitted with thin metal strips arranged perpendicular to the wire running through the centre instead of the calorimetric readout pads as used in the tail catcher design. An illustration of a section of the instrumented iron, showing the location of the strip and pad detectors, is shown in figure 2.9.

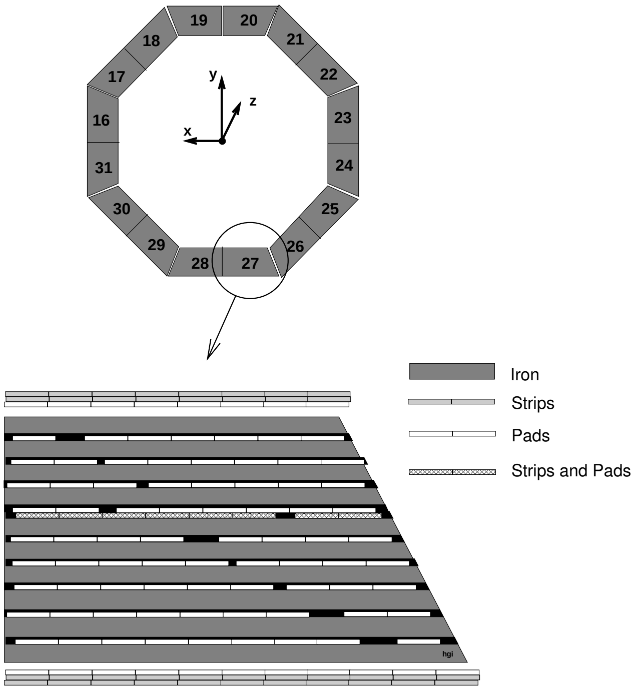

Figure 2.9: The structure of an Instrumented Iron module.

When the streamer occurs within the LST, pulses generated on the strips give a signal or "hit" in the instrumented iron. These hits are then combined by the central muon trigger to reconstruct the muon track. In the central (barrel) region, at least 2 hits in the inner 4 layers are required. In the endcaps, which complete the iron shell around the detector, at least 3/5 hits are required.[6]

[6]In the inner region of the forward endcap 4/5 hits are required due to the higher rate from the result of ep collisions and from the beam-halo background.

2.5.2 Forward Muons

The high multiplicity of tracks present in the forward region makes track linking of potential muon candidates between the FTD and the instrumented iron difficult. In the forward direction, outside of the main body of the H1 detector, the Forward Muon Detector (FMD) [24] provides additional muon identification. The FMD is able to provide a secondary momentum (p) measurement to complement the measurement from the FTD, increasing the probability of a correct track link. Furthermore, the FMD can be used in conjunction with the instrumented iron to minimise the misidentification of non-muon tracks arising from the proton remnant.

The FMD, shown in figure 2.10, is composed of six double layers of drift chambers, three either side of a central 1.5 T toroidal magnet. Within the individual drift chambers, all sense wires are strung perpendicular to the beam pipe. The drift chambers are arranged concentrically in four layers to measure in θ and radially in two layers to measure in ϕ. This gives rise to the naming convention of the layers; a "theta" layer is shown in figure 2.10b. The double layers are arranged in parallel, although the drift chambers are offset as illustrated in figure 2.10c. Each layer is divided into octants and a total of 1520 drift chambers are used in the detector, varying in length from 0.40m to 2.40m.

The field of the main H1 solenoid has little effect at such low θ angles and so the toroidal magnet is used to bend the path of traversing muons, enabling an independent momentum measurement. This measurement is limited to the range $5 \leq p \leq 100$ GeV. The lower bound is set due to the absorption of low energy muons in the magnet itself, or in material between the interaction point and the FMD. At momenta above 100 GeV, the measurement is limited by resolution effects and the strength of the toroid magnet.

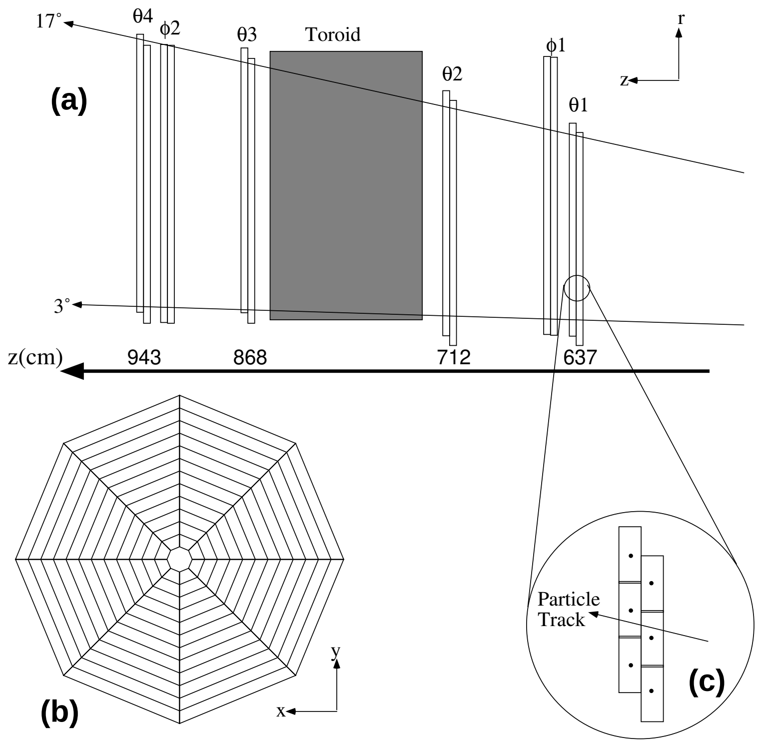

Figure 2.10: The Forward Muon Detector. (a) The r-z plane, (b) A theta layer, (c) A close up of the double-layer structure.

2.6 The Time of Flight Systems

The rate of background events at HERA is much larger than that of events produced from *ep* collisions. The rejection of this background, mainly associated with the proton beam[7], is vital if genuine physics interactions are to be efficiently recorded. Beam-gas or beam-wall interactions are rejected using plastic scintillation detectors placed either side of the interaction point. Figure 2.11 (top) shows a beam gas event detected within H1.

The Time of Flight (ToF) system [25] is comprised of separate scintillators all located close to the beam pipe: within the backward iron endcap *(BToF)*; within

[7]The electron beam is a source of background synchrotron radiation, due to the last bending magnet before the interaction point. More details on this background can be found in [5].

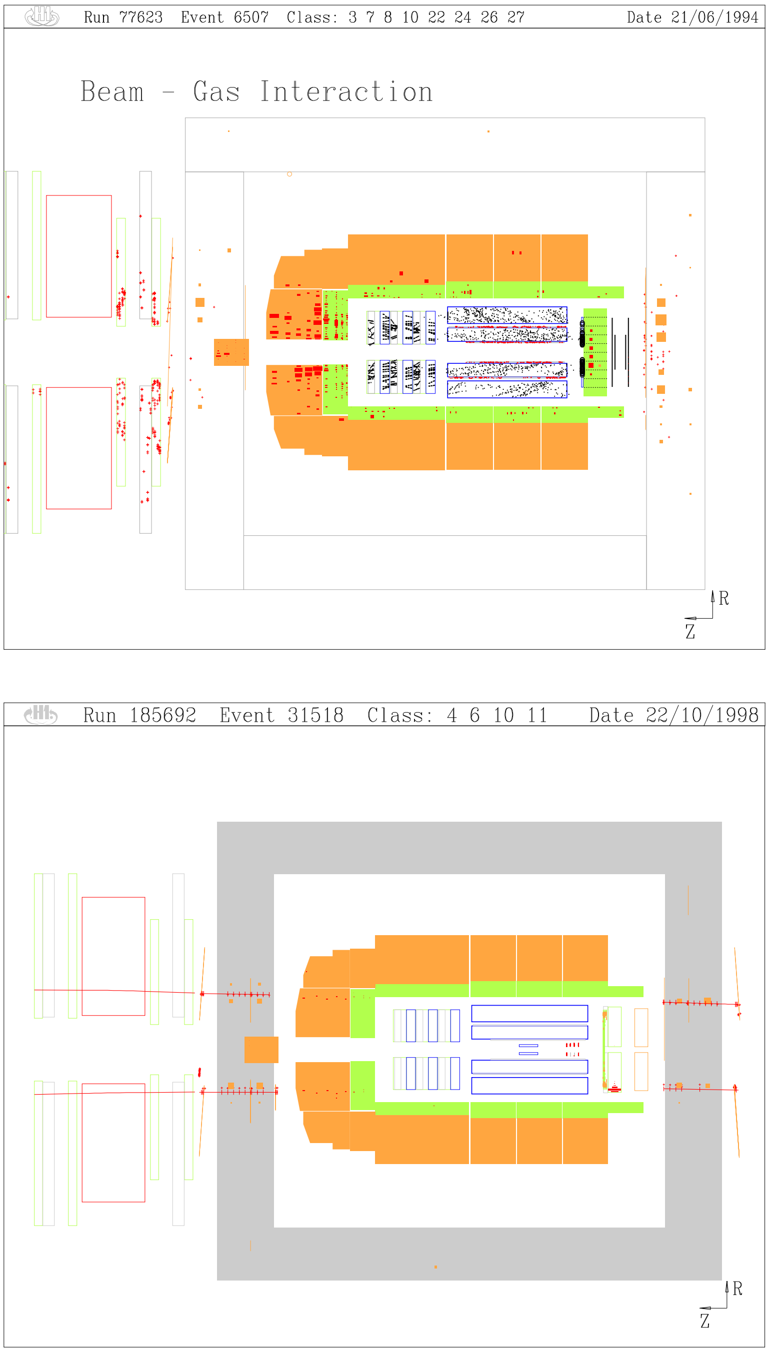

Figure 2.11: Proton beam induced background within H1: a beam-gas event (top); a muon beam-halo event (bottom).

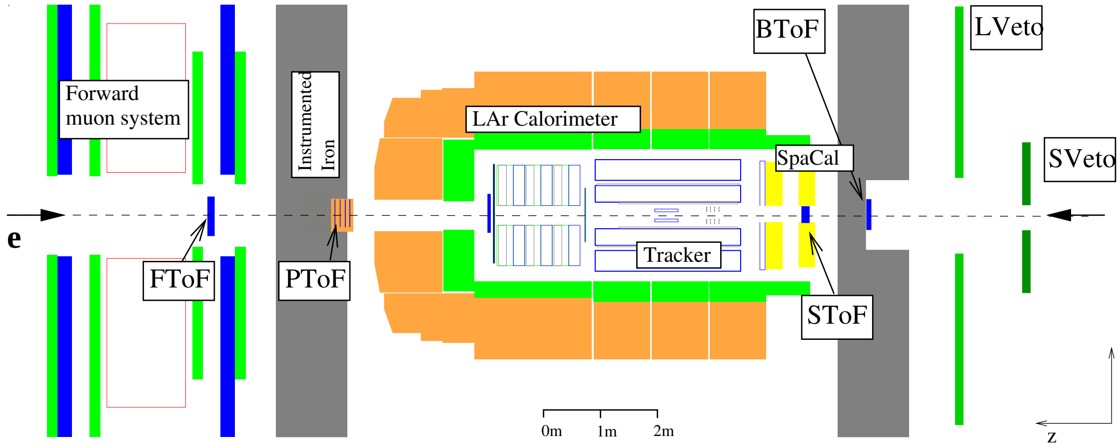

Figure 2.12: The Time of Flight Systems.

the Plug calorimeter *(PToF)* and close to the FMD *(FToF)* as shown in figure 2.12. As previously mentioned in section 2.4.2, the SpaCal is also used to provide further ToF information in the backward region *(SToF)*. The principle behind the ToF system is that particles produced via non-ep interactions will arrive earlier[8] at these detectors, at approximately the same time as the proton bunch. However, beam-gas and beam-wall events near the interaction point cannot be rejected using timing information alone.

A further background source arises from the beam-halo, a shower of particles (mainly muons) which accompanies the proton beam. These particles are caused by the inelastic collisions of protons with residual beam-gas or hardware outside of the H1 detector. Figure 2.11 (bottom) illustrates the detection of the halo within the detector. To combat this background, the Veto Wall complements the ToF system. This detector comprises of two large scintillators located outside of the iron at $z = -6.5m$ *(LVeto)* and $z = -8.1m$ *(SVeto)* to detect the halo before the proton beam enters the detector.

[8]This time difference is easily calculable as $\approx 2\Delta z$, where Δz is the distance between the interaction point and the scintillator.

The use of non-colliding pilot bunches allows the rate of these processes to be studied without the presence of ep collisions and by employing these methods the background rate is reduced by $\approx 99\%$.

2.7 The Luminosity System

In order to calculate cross sections and event rates, the luminosity delivered by HERA to H1 must be accurately measured. A fast online system is employed by HERA in order to steer the beams and ensure the conditions are optimised within the detector. This is the role of the luminosity system [26] illustrated in figure 2.13. The system is comprised of two components: an electron tagger (ET) and a photon detector (PD) located close to the beam-pipe at $z = -33.4m$ and $z = -102.9m$ respectively. Both the ET and PD are square arrays of TlCl/TlBr crystals and 22 radiation lengths deep. The energy resolution of each detector is $\frac{\sigma(E)}{E} \sim \frac{0.10}{\sqrt{E/GeV}} \oplus 0.01$.

A luminosity measurement is determined by observing the rate of the *Bethe-Heitler* process [27], $ep \rightarrow ep\gamma$, whose signal is coincident hits in the two separate components of the system. The sum of the energy of the detected photon and electron is required to be similar to that of the electron beam. The cross section for this process is precisely known, enabling an accurate online calculation. The acceptance of the ET changes with beam optics and individual run conditions, introducing a systematic error into the calculation. The main background source is bremsstrahlung interactions with the residual beam-gas. The luminosity, $\mathcal{L}$, is given by the following equation in terms of the total (R_{tot}) and background (R_{bg}) bremsstrahlung rates:

$$\mathcal{L} = \frac{R_{tot} - (I_{tot}/I_{bg})R_{bg}}{\sigma^{visible}_{ep\rightarrow ep\gamma}} \tag{2.1}$$

where I_{tot} (I_{bg}) is the total (background) current and $\sigma^{visible}_{ep\rightarrow ep\gamma}$ is the cross section

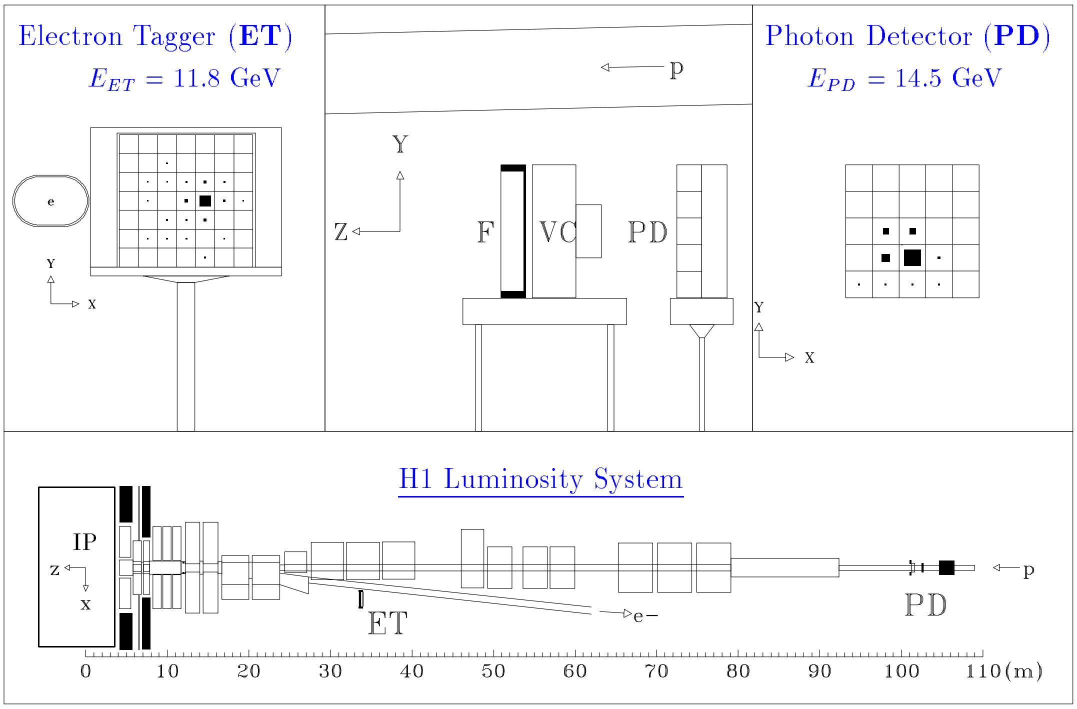

Figure 2.13: The Luminosity System.

for the $ep \rightarrow ep\gamma$ process with the ET acceptance and trigger efficiency included. The background rate is determined from pilot bunch information.

An offline measurement of the luminosity is carried out for use in physics analyses. This method involves only the rate of detection of the scattered photon and hence removes the uncertainty from the acceptance of the ET. Further corrections are made to account for the contribution to the proton current from satellite bunches, which can be as large as 10%.

2.8 Triggering and Readout

The H1 detector contains approximately 270,000 readout channels, which combined with the HERA bunch crossing frequency of 96 ns (equivalent to ≈ 10 MHz) provides a potential rate of data flow that is too high for modern detector components and electronics to process. Furthermore, the readout time of some detector components is more than an order of magnitude longer than the crossing interval. To combat this, a pipelined multi-layered trigger system is employed, as illustrated in figure 2.14, to record only those events of interest.

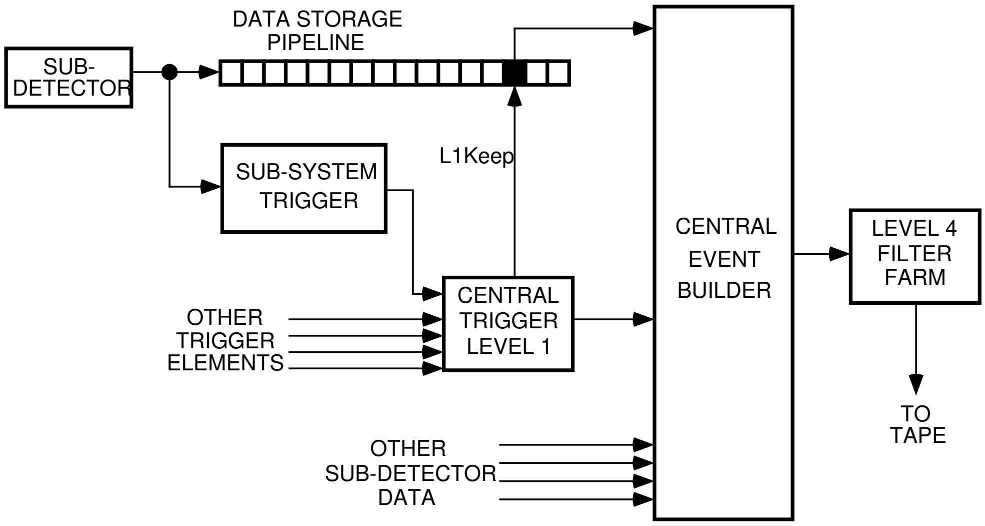

Figure 2.14: The H1 Trigger System showing the Central Trigger (CTL1), Central Event Builder (CEB) and Data Storage Pipeline. L2 is not shown.

The level one (L1) central trigger consists of ≈ 200 *trigger elements* providing information from different parts of the detector. These elements are combined into 128 *subtriggers*, the majority of which are designed to trigger a variety of different physics processes, although some are used to monitor backgrounds and trigger efficiencies. If a subtrigger fires, then an L1 keep signal is sent to the central trigger (CTL1) [28]. The L1 decision takes ≈ 24 bunch crossings, so all of the information from subsequent bunch crossings is kept in a pipeline, ensuring new data is constantly taken. This results in a negligible deadtime on L1. The subtriggers fired by more common physics processes are only accepted by the central trigger a fraction of the time using a technique called *prescaling*. For a trigger with a prescale of p, only 1 in p events are kept. This prevents the rate into level two (L2) being dominated by a few common physics subtriggers or those used to monitor background rates.

The L2 trigger combines different subtriggers, often utilising different subdetectors, to give more detailed information on the event. There are two components: a topological trigger (L2TT) [29], which employs pattern recognition using a 2D projection (or *topology*) of the event in θ and ϕ and a neural network based system (L2NN) [30]. Once a keep decision has been reached, the whole event is sent to the Central Event Builder (CEB). This process takes $\approx$ 1-2 ms, during which the pipeline is stopped, creating deadtime. The overall deadtime of the experiment in normal operation is usually about 10%.

Level three (L3) has not yet been implemented at H1. The proposed Fast Track Trigger (FTT) [31], part of the ongoing H1 upgrade program [32], will use this level to perform particle identification. L1 and L2 of the FTT are employed in the design of a new trigger, which is discussed in chapter 5.

The level four (L4) trigger runs on a filter farm of 30 PC's providing more detailed reconstruction and selection of tracks and clusters. The L4 farm can process events at a rate of up to 50 Hz, above which further deadtime accumulates. By this stage most background events have been removed and L4 writes the events to tape at a rate of about 10 Hz. The final stage, level five (L5), is performed offline and includes full event reconstruction and classification using the `H1REC` software package [33]. The full output is written to Production Output Tapes (POTs) and a simplified version to Data Summary Tapes (DSTs). DSTs contain a reduced set of information, each event typically about 10 kB in size. In order to carry out analysis, DSTs are then further processed by a physics analysis package. The trigger selection used in this analysis is described in section 4.4.

2.9 Monte Carlo Simulation

To study different physics models and in particular compare these models with experimental data, stochastic techniques are employed. These techniques, which use random numbers and probability distributions, are termed *Monte Carlo*[9] methods.

The simulation of real physics processes may be divided into two sections. Firstly, event generators produce all final state partons for a given interaction, using all relevant diagrams and parton density functions. The interactions of any unstable partons produced (mainly quarks and gluons) are further simulated until only long lived stable particles exist. An "event" then consists of a list of 4-vectors, describing the final state. This is termed the *Generator Level* of the simulation. To then make a useful comparison to the data, the interaction of the generated final state within the H1 detector is modelled using the `H1SIM` [35] package based on the simulation package GEANT3 [36]. This models the interaction of the particles in each of the subdetectors. Finally, full reconstruction of the event is carried out using the reconstruction software package `H1REC` to provide a level of simulation which is directly comparable to the recorded DST data described in the previous section. This final stage is the *Reconstructed Level*. The differences between the two levels of simulation also provide a method of correcting detector acceptances and resolution effects in the data.

The Monte Carlo model used to describe the signal process in this analysis is described in detail in section 3.4.2. Models used to describe background processes are introduced in section 3.6.

[9] The name was originally used in the Manhattan Project at Los Alamos in the 1940's and was suggested by the gambling casinos in Monte Carlo, Monaco as a suitable name to describe the random number method used in numerical integrations [34].

Chapter 3

Theoretical Overview

A wide range of *ep* physics is currently studied at HERA. This chapter details the necessary background material needed to understand the theory behind the work in this thesis. The kinematical variables used to describe *ep* scattering are introduced in the next section, followed by a brief discussion of photoproduction and DIS. The Standard Model (SM) signal processes in this analysis are then introduced, including a description of the Monte Carlo generator used to model them. This is followed by a short section on the areas of Beyond the Standard Model (BSM) physics relevant to this analysis. Finally, the background processes contributing to this analysis are examined and further Monte Carlos introduced.

3.1 The Kinematics of *ep* Scattering

The two contributions to *ep* scattering at HERA are the *Neutral Current* (NC) process ($ep \rightarrow eX$) and the *Charged Current* (CC) process ($ep \rightarrow \nu X$), as illustrated in figure 3.1. The incident electron (e) and proton (p) have four-momenta $k^{\mu} = (E_e, \mathbf{k})$ and $p^{\mu} = (E_p, \mathbf{p})$ respectively. The "scatter" involves the exchange of a single *gauge boson*, resulting in a transfer of four-momentum between the particles.

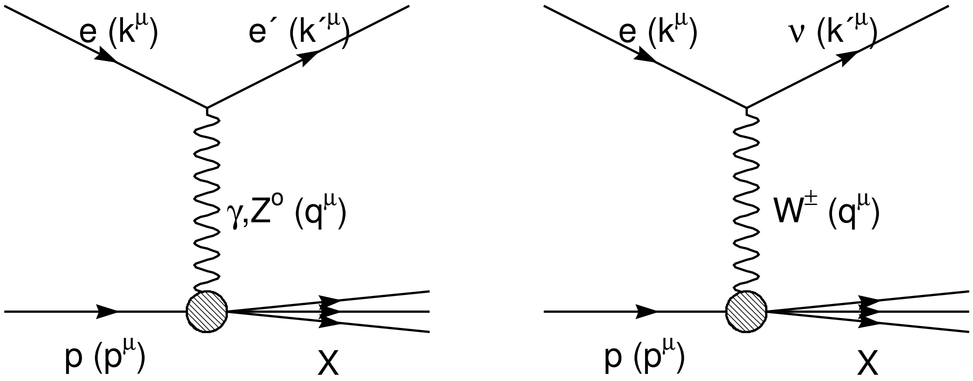

Figure 3.1: Virtual boson exchange in *ep* scattering via NC (left) and CC (right) interactions.

The square of the four-momentum transfer is defined as

$$Q^2 = -q^2 = -(k^\mu - k'^\mu)^2 \tag{3.1}$$

where $k'^\mu = (E_l', \mathbf{k}')$ is the four-momentum of the scattered lepton. In NC events this boson is neutral, either a photon (γ) or Z°, whereas in CC events a $W^\pm$ is exchanged. The names NC and CC refer to the *lepton current* across the vertex of the exchange boson [37]. The scattered lepton is consequently the original electron (e') in NC events and a neutrino (ν) in CC events. The hadronic state, labelled X, consists of the original proton if the scatter was elastic or a combination of the struck quark and the proton remnant if the interaction was inelastic.

The kinematics of the interaction are further described using several other Lorentz scalars formed from combinations of the above mentioned four-vectors. The centre of mass (COM) energy squared of the interaction is given by

$$s = (k^\mu + p^\mu)^2 \approx 4E_eE_p \tag{3.2}$$

where the approximation neglects the masses of the incident particles[1]. The fraction of the proton's momentum carried by the struck quark is given by the quantity *Bjorken*[2] x, where

$$x = \frac{Q^2}{2p^\mu \cdot q^\mu} \tag{3.3}$$

assuming the quark is massless and carries no transverse momentum. This is the basis of the *Quark Parton Model* (QPM) [39], where the quarks are considered to be independent point-like entities called *partons*, travelling co-linearly within the proton. An inelastic electron-proton scatter is then viewed as an elastic electron-parton scattering. This theory is tested by measurement of the *structure function* F_2, discussed later in this chapter. Finally, the *inelasticity* of the interaction, y, is given by

$$y = \frac{p^\mu \cdot q^\mu}{k^\mu \cdot p^\mu} \tag{3.4}$$

and is equal to the fraction of the incident electron's momentum carried by the exchange boson in the rest frame of the proton. Both x and y are constrained to take values between 0 and 1 as a result of four-momentum conservation. The above quantities are related by

$$Q^2 \approx sxy \tag{3.5}$$

resulting in a maximum squared four-momentum exchange equal to the centre of mass energy squared, s. The value of Q^2 is a measure of the *virtuality* of the exchange boson, providing an interaction resolution scale. The size of the proton

[1]This approximation is appropriate at HERA, as the masses of the colliding particles are negligible compared to their momenta. The energy of a particle, p, is related to its mass and momentum by $E_p^2 = p_p^2 + m_p^2$.

[2]J. D. Bjorken. See [38].

is $\mathcal{O}(10^{-15}\text{m})$, equivalent to $Q^2 \approx 1$ GeV^2. For Q^2 much less than this value, the exchange photon is considered to be almost real, or *on mass shell.* This type of interaction is termed photoproduction. At much larger values of Q^2, the highly virtual photon probes the structure of the proton, enabling the internal constituents to be investigated. This type of interaction is called Deep Inelastic Scattering. These two regimes are discussed in the following sections.

The rate $\mathcal{R}_I$ of a given ep interaction I is defined as

$$\mathcal{R}_I = \mathcal{L}\sigma_I \tag{3.6}$$

where the *cross section* σ_I is a measure of the probability of interaction I occurring. The luminosity $\mathcal{L}$ is given by

$$\mathcal{L} = N_e N_p \ f \ / \ W_x W_y \tag{3.7}$$

where N_e and N_p are the number of particles in each colliding bunch, f is the frequency of rotation in HERA and W_x and W_y are parameters defined from the 2D profiles of each beam. If the particle densities in each beam are assumed to be Gaussian, along the same axis and the same in x and y then

$$W_x W_y = 2\pi(V_e + V_p) \tag{3.8}$$

where V_e and V_p are the variances of the Gaussians of the electron and proton beams respectively. The luminosity measurement at H1 is described in section 2.7.

3.2 Photoproduction

In the true photoproduction regime Q^2 is zero, although the definition is usually taken to be $Q^2 \ll 1$ GeV^2, since the exchange momentum is never equal to zero. In fact, interactions occuring within H1 are classified using the geometrical acceptance of the detector and are termed photoproduction if the scattered electron is detected in either the 33m or 44m electron tagger, equivalent to $Q^2 < 0.01$ GeV^2.

Photoproduction is divided into two regions depending on the average transverse momentum P_T of the final state. Low transverse momentum, low energy (*soft*) processes typically involve the production of vector mesons, for example a ρ, ω or ϕ. The photon fluctuates into an off-shell meson that is then put on-shell by a small momentum transfer from the proton. Processes involving higher transverse momenta are an indication of some *hard* sub-process and may be classified into two further categories. In *direct* photoproduction the photon couples directly to the hard sub-process, as illustrated in figure 3.2 (left). In *resolved* photoproduction, shown in figure 3.2 (right), the photon fluctuates into a $q\overline{q}$ pair, one of which then participates in the hard sub-process.

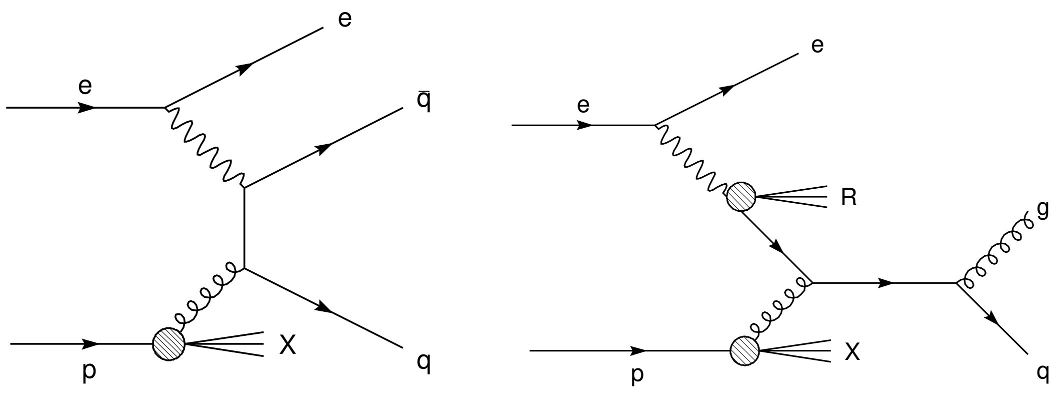

Figure 3.2: Direct (left) and resolved (right) photoproduction in *ep* scattering.

A key difference between the two processes is that in direct events all of the photon's momentum contributes to the hard sub-process, whereas in a resolved interaction some momentum is retained by the photon remnant, R. This remnant contains a mixture of quarks and gluons and by measuring the P_T of jets produced in the resolved processes, the partonic content of the photon can be measured [40].

3.3 DIS: Probing the Structure of the Proton

For values of $Q^2 \geq 1$ GeV^2, the (virtual) photon is able to resolve the internal substructure of the proton. This is the transition from photoproduction to the DIS regime, where the constituent partons are probed as illustrated in figure 3.3. As Q^2 increases to $\mathcal{O}(M^2_{Z^\circ}, M^2_{W^\pm})$, the heavier Z° and $W^\pm$ exchange bosons also contribute to the DIS process.

A series of *structure functions* are used to parameterise the cross sections of ep interactions, a summary of which is presented in the following section. A more rigorous derivation is given in [41].

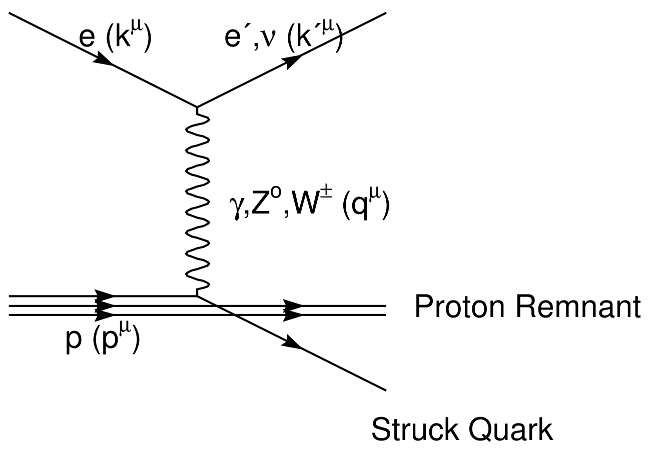

Figure 3.3: Deep Inelastic Scattering. The incident electron, scattered lepton, exchange boson and proton have four-momenta k^μ, k'^μ, q^μ and p^μ respectively.

3.3.1 Cross Sections and Structure Functions

The NC cross section as a function of x and Q^2 is given by

$$\frac{d^2\sigma_{NC}^{e^\pm p}}{dxdQ^2} = \frac{e^4}{8\pi x} \left(\frac{1}{Q^2}\right)^2 \phi_{NC}^{\pm}(x, Q^2) \tag{3.9}$$

to lowest order in Quantum Electrodynamics (QED). The first term includes the electromagnetic coupling constant, where e is simply the charge of the electron. The main Q^2 dependence of the cross section comes from the $\frac{1}{Q^4}$ *propagator* term. This strong dependence means that the total *ep* cross section is dominated by photoproduction. Finally, the *structure function* term is defined as

$$\phi_{NC}^{\pm} = Y_+ \ \tilde{F}_2^{\pm}(x, Q^2) - y^2 \ \tilde{F}_L^{\pm}(x, Q^2) \mp Y_- \ x \ \tilde{F}_3^{\pm}(x, Q^2) \tag{3.10}$$

and is a linear combination of three different structure functions: $\tilde{F}_2$, $\tilde{F}_L$ and $x\tilde{F}_3$. The helicity dependence term is given by

$$Y_\pm = 1 \pm (1-y)^2 \tag{3.11}$$

$\tilde{F}_2$ is composed of 3 further structure functions, describing pure γ exchange (F_2), pure Z° exchange ($F_2^{Z^\circ}$) and γZ° interference ($F_2^{\gamma Z^\circ}$). $x\tilde{F}_3$ similarly contains pure Z° exchange and γZ° interference structure functions. These further structure functions include sum terms over the quark and anti-quark densities in the proton, $q_f(x,Q^2)$, where f represents all quark and anti-quark flavours. The QPM predicts that these *parton density functions* depend only on x. This is addressed in section 3.3.2. The $\tilde{F}_2$ structure functions sum the quark and anti-quark densities, whereas $x\tilde{F}_3$ structure functions take their difference. $\tilde{F}_L$ is the longitudinal structure function, which has an identically zero contribution to the cross section at leading order (LO).

The cross section of the CC process is similarly defined as

$$\frac{d^2\sigma_{CC}^{e^\pm p}}{dxdQ^2} = \frac{g^4}{64\pi x}\left(\frac{1}{Q^2+M_{W^\pm}^2}\right)^2 \phi_{CC}^{\pm}(x,Q^2) \tag{3.12}$$

where

$$\phi_{CC}^{\pm} = Y_+\ \tilde{W}_2^{\pm}(x,Q^2) - y^2\ \tilde{W}_L^{\pm}(x,Q^2) \mp Y_-\ x\ \tilde{W}_3^{\pm}(x,Q^2) \tag{3.13}$$

and g is the weak coupling constant and $\tilde{W}_2$, $\tilde{W}_L$ and $x\tilde{W}_3$ are the equivalent CC structure functions. The propagator term now also includes the mass of the W boson $M_{W^\pm}$ and the CC cross section is subsequently suppressed at low Q^2 with respect to the NC process. The weak and electromagnetic coupling constants are related by the unification equation

$$g^2 = \frac{e^2}{\sin^2\theta_W} \approx 4e^2 \tag{3.14}$$

where θ_W is the *weak mixing angle*[3]. The relative cross section suppression factor can be expressed as

$$\frac{\sigma(Z^o,W^\pm)}{\sigma(\gamma)} \propto \left|\frac{Q^2}{Q^2+M_{Z^o,W^\pm}^2}\right|^2 \tag{3.15}$$

At the electroweak unification scale, where $Q^2 \gtrsim M_{W^\pm}^2 \approx M_{Z^\circ}^2 \approx 10^4$ GeV^2, the NC and CC cross sections are of the same order. This is observed in the measured cross sections, as shown in figure 3.4. In the high Q^2 domain, Z° exchange also contributes significantly to the NC process causing constructive (destructive) γZ° interference in e^-p (e^+p) interactions. In CC, the e^-p cross section is larger with respect to the e^+p process at higher Q^2. This is due to the charged W^- (W^+) boson coupling to the u (d) valence quarks in the proton.

[3]A recent measurement of the weak mixing angle is $\sin^2\theta_W = 0.2277 \pm 0.0013$ (stat) $\pm$ 0.0009 (syst) [42].

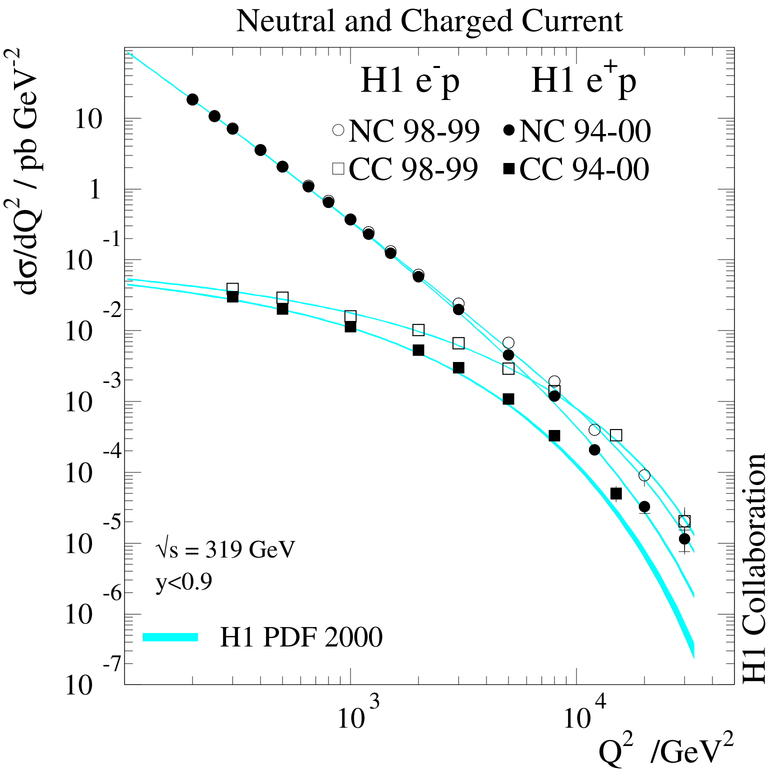

Figure 3.4: The differential NC and CC cross sections for e^+p and e^-p scattering as a function of Q^2. The data are compared to the SM expectations determined from the H1 2000 PDF Fit. Taken from [43].

3.3.2 Scaling, Scaling Violations and QCD

The NC differential cross section is measured by H1 and from it the $F_2(x, Q^2)$ structure function may be extracted, which describes pure γ exchange. Details of how this quantity is extracted from the total NC cross section can be found in [43]. This measurement is shown over a range of x and Q^2 in figure 3.5. According to the QPM, the parton density functions are dependent only on x, and $F_2(x, Q^2)$ is given by

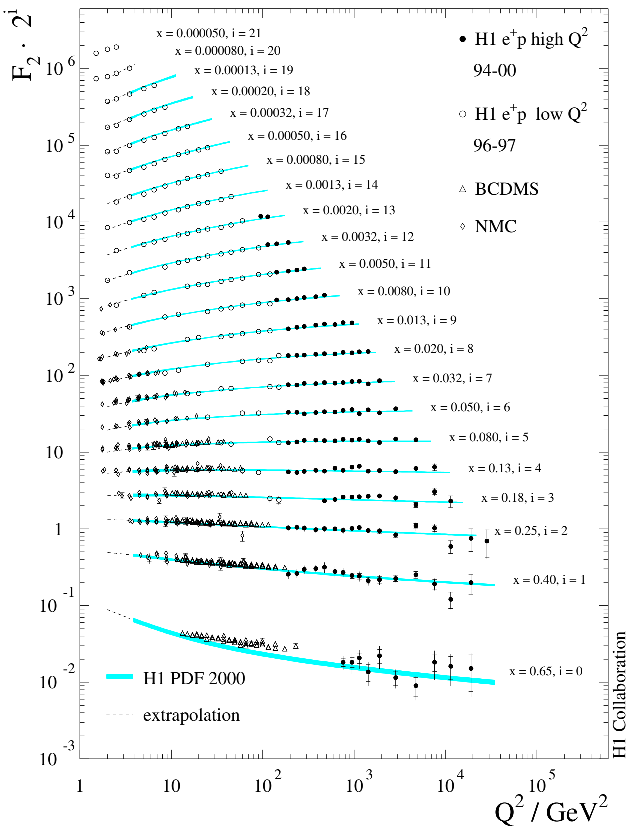

Figure 3.5: The proton structure function $F_2(x, Q^2)$ as a function of Q^2 for a range of different x values. The H1 data presented are compared to the H1 2000 PDF Fit [43]. In addition, data from the fixed target experiments BCDMS [44] and NMC [45] are also displayed.

$$F_2(x, Q^2) = x \sum_f e_f^2 q_f(x) \tag{3.16}$$

where e_f is the charge of quark flavour f and the sum is over all quark and anti-quark flavours. In this model, the quarks are point-like entities so that no length scale is involved and consequently F_2 is not expected to vary with Q^2, a phenomenon known as *scaling* [46].

However, deviations from scaling are seen in the data across a wider range of x

and Q^2, a behaviour known as *scaling violation*. The results of the early fixed target experiments BCDMS [44] and NMC [45] are also shown in figure 3.5, where the first evidence of scaling violation was observed. At low x F_2 is seen to rise with Q^2 and to a lesser degree fall with Q^2 at high x. This rise of F_2 at low x can be explained by considering the effect of the gluons in the proton. The density of gluons in the proton $xg(x)$ is seen to rise with falling x, as shown in figure 3.6. That is, the number of gluons in the proton carrying a fraction x of the proton's momentum increases as x decreases. The rise at low x of F_2 with increasing Q^2 is then attributed to the increase in the resolving power of the photon probe to detect the partonic content of the proton, and that the parton density functions do indeed depend on Q^2.

The sum of all parton momenta must be equal to the sum of the momentum of the proton, from the momentum sum rule

$$\sum_f \int_0^1 dx\ x\ q_f(x) = 1 \tag{3.17}$$

If the sum is performed over only the quarks as in equation 3.17, approximately 50% of the proton's momentum is unaccounted for. This deficit is attributed to the gluons. The momentum sum rule also constrains F_2 to fall at high x with increasing Q^2.

Scaling violations are described by introducing corrections to the QPM using Quantum Chromodynamics (QCD), the theory which describes the interactions between quarks and gluons. The QPM is equivalent to the zeroth order of QCD; higher order corrections are introduced as a perturbative expansion in orders of the strong coupling constant, α_s. Leading order corrections are formulated using the Alterelli-Parisi splitting functions [48], resulting in logarithmic terms in $\alpha_s \ln Q^2$ and $\alpha_s \ln \frac{1}{x}$. These functions express the probability that a parton will "split", either a quark radiating a gluon or a gluon converting to a $q\overline{q}$ pair, as illustrated in figure 3.7.

Further iterations of the splitting functions employ more complex perturbative

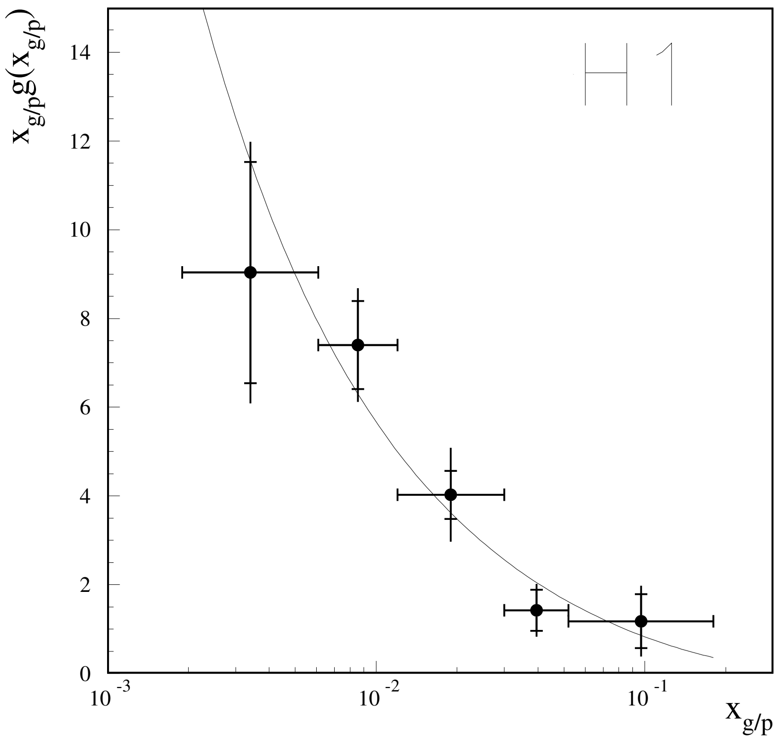

Figure 3.6: The measured gluon density $xg(x)$ as a function of fractional gluon momentum at an average Q^2 of 30 GeV^2. The solid curve shows a fit to the data points. Taken from [47].

QCD (pQCD) calculations to describe the evolution of F_2, such as the DGLAP [48, 49] and BFKL [50] schemes. At HERA, the DGLAP evolution scheme can be tested across the whole kinematic plane; BFKL may also be tested in the low x domain [51]. A more detailed description of QCD and the perturbative approach can be found in [52].

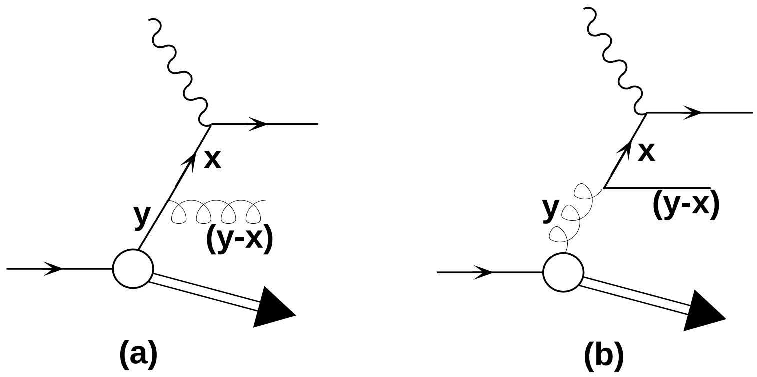

Figure 3.7: Diagrams showing leading order QCD corrections to the QPM. The quark coupling to the photon carries a fraction $\left(\frac{x}{y}\right)$ of the momentum of the original parton, which is in (a) a quark and (b) a gluon.

3.4 Standard Model Signal Processes

In this analysis a search is performed for events containing isolated, high P_T leptons and missing transverse momentum. An event is hence termed "signal" if this topology is present in the final state, and is furthermore present due to genuine physics processes. Within the SM, such events are produced mainly via W production with subsequent leptonic decay. A small contribution is also produced via Z° production. This section presents a review of W production at HERA, with emphasis on the dominant production mechanism, the calculation of the cross section (see section 3.4.2) and the subsequent decay channels that contribute to the signal process in this analysis (see section 3.4.3). The contribution from Z° production is addressed in section 3.4.4.

3.4.1 W Production

In addition to the virtual W bosons involved in high Q^2 CC DIS, the high centre of mass energy of ep collisions at HERA allows the *electroproduction* of real W bosons.

However, the total cross section for W production is much smaller than those of the NC and CC interactions, making it a comparatively rare event. Two different channels contribute to the W production mechanism,

$$ep \rightarrow eWX \tag{3.18}$$

and

$$ep \rightarrow \nu WX \tag{3.19}$$

where the final state includes the W boson, an electron (eW production) or neutrino (νW production) and the hadronic system X, as defined earlier. The process is dominated by eW production, which has a cross section an order of magnitude higher [53].

At the parton level, eW production proceeds via the Feynman diagrams displayed in figure 3.8 and the related crossing diagrams with an antiquark in the initial state. Diagrams 3.8(a) and (b) can be viewed as extensions of the NC interaction with the additional radiation of a W boson from the quark line, sometimes referred to as *W-strahlung*. If the W is radiated from the initial state quark as in figure 3.8(a), then the diagram includes both a *t-channel* photon and *u-channel* fermion, so that this particular production mechanism dominates the cross section. The calculation of the cross section is described in section 3.4.2. Diagram (c) includes a $WW\gamma$ triple boson coupling (TBC). This is addressed in section 3.5. Diagrams (d) and (e) contain off-shell W propagators and are required to preserve electromagnetic gauge invariance when considering the $W \rightarrow f\bar{f}'$ decay [54]. Finally, diagrams (f) and (g) feature a W radiated from the lepton line. These processes are greatly suppressed due to the presence of a second heavy propagator.

The equivalent set of diagrams for the $ep \rightarrow \nu WX$ process is shown in figure 3.9.

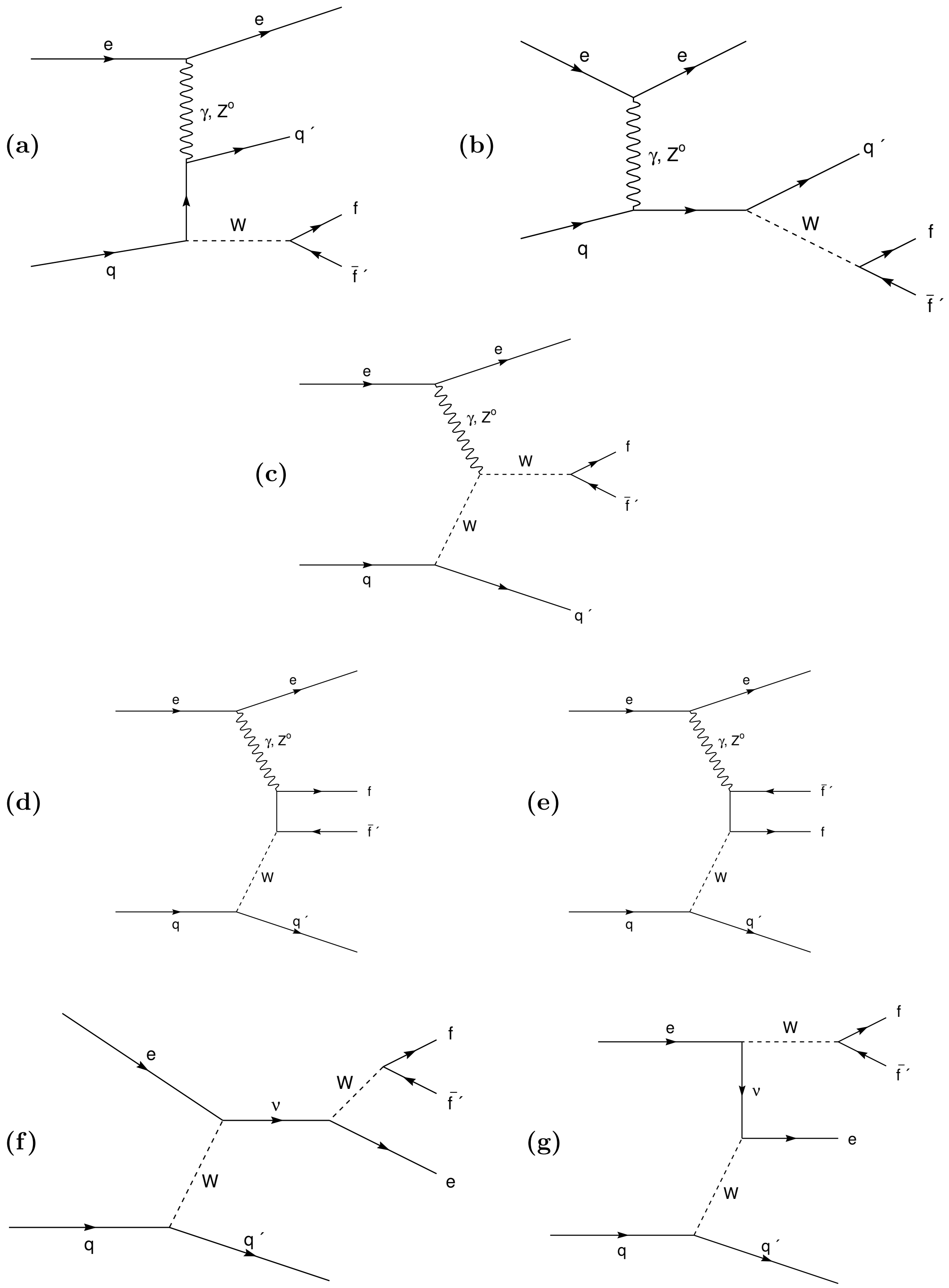

Figure 3.8: Diagrams for the process $ep \to eW^{\pm}X$, including the subsequent decay $W \to f\overline{f'}$.

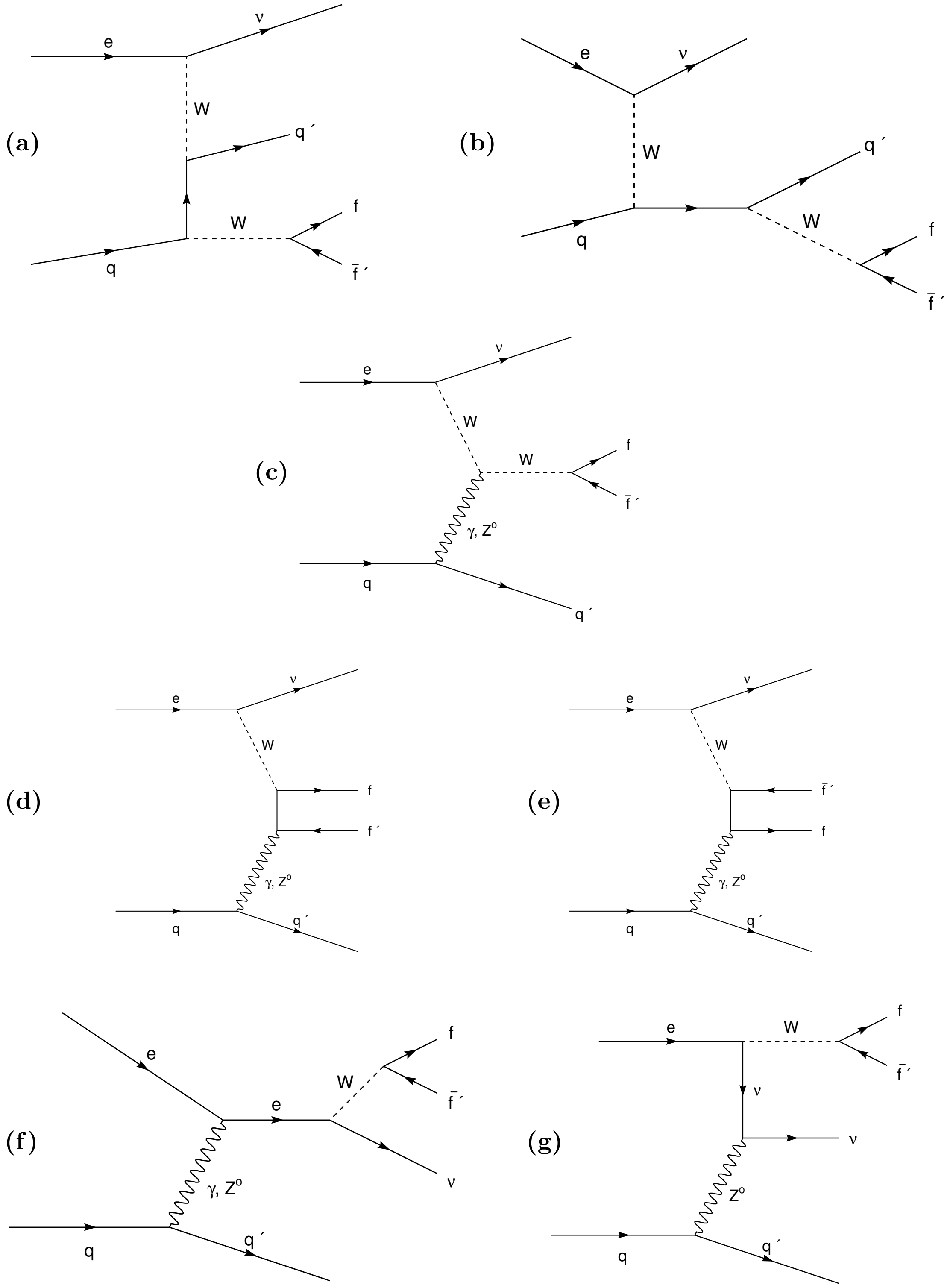

Figure 3.9: Diagrams for the process $ep \rightarrow \nu W^{\pm} X$, including the subsequent decay $W \rightarrow f\overline{f'}$.

A diagram analogous to the dominant u and t-channel diagram in eW production does not contribute to this process, resulting in the lower cross section for νW production. Approximately 50% of the total cross section arises from elastic or quasi-elastic scattering, where the interaction proceeds via diagrams 3.9(c)-(f). In elastic scattering the proton remains intact and the quark line is replaced by a proton line. The quasi-elastic domain is similar to low energy photoproduction, as described in section 3.2. The remainder of the cross section is attributed to DIS processes and involves all diagrams in figure 3.9. Similarly to figure 3.8, diagrams (a) and (b) are extensions of the CC interaction, with the additional radiation of a W boson. Unlike diagram (f), only the Z° propagator contributes to diagram (g) due to the neutrino vertex.

3.4.2 W Cross Section Calculation

The treatment of the W cross section at leading order (LO) is outlined as performed by the authors of the Monte Carlo generator EPVEC [54, 55]. The stages of Monte Carlo simulation are summarised in section 2.9. Discussion of the calculation is limited here to the more dominant eW production channel; a more complete description can be found in [54]. Additionally, a new next to leading order (NLO) cross section calculation has been performed [56], and is included in the results presented in this thesis.

EPVEC simulates all eight parton level diagrams shown in figure 3.8; each involving an electron and proton in the initial state, the production of the W boson and its subsequent decay to a fermion-antifermion pair. Diagrams involving a t-channel photon drive the cross section, due to the corresponding $\frac{1}{t}$ pole term in the scattering amplitude. In such diagrams, $|t| \equiv Q^2$ and consequently the photoproduction regime dominates. This t-channel phenomenology appears in diagrams 3.8(a)-(e), but as previously stated the main contribution to the cross section arises from figure

3.8(a). In this diagram, a further $\frac{1}{u}$ pole term is induced in the amplitude due to the u-channel quark propagator where

$$u = (p_q - p_W)^2 = (p_k - p_{q'})^2 \tag{3.20}$$

p_q ($p_{q'}$) is the four vector of the initial (final) state quark and p_k (p_W) is the four vector of the photon (W boson). As $u \to 0$, QCD corrections become large and the partonic structure of the photon must be included in the calculation. It is therefore useful to introduce two distinct regions of phase space that are analytically different: the DIS regime at high $|u|$ and the photoproduction regime at low $|u|$. This is done by dividing the cross section into two regions of phase space, dependent on the magnitude of the momentum transfer $|u|$, so that

$$\sigma = \sigma(|u| > u_{cut}) + \int_{-u_{cut}}^{u_{cut}} d|u| \frac{d\sigma}{d|u|} \tag{3.21}$$

The phase space may also be divided using Q^2, details of which can be found in [56]. Calculation of the DIS regime, where $|u| > u_{cut}$, is performed for the full set of diagrams in figure 3.8 using helicity amplitudes for the process $eq \to eWq^{'}$, $W \to f\overline{f'}$ [57]. The photoproduction regime, where $|u| < u_{cut}$, is calculated by folding the $\gamma q \to Wq^{'}$, $W \to f\overline{f'}$ cross section with the Weizsäcker-Williams splitting function [58]. In the resolved mechanism the W is produced via the standard Drell-Yan process [59] $q\overline{q} \to W$, where one quark originates from the photon and the other from the proton.

The above discussion assumes an on-shell W. In order to provide a realistic simulation including finite width effects, each amplitude is multiplied by a Breit-Wigner propagator term given by

$$\frac{p_W^2 - m_W^2}{p_W^2 - m_W^2 + im_W\Gamma_W} \tag{3.22}$$

where m_W (Γ_W) is the mass (width) of the W boson. Final state parton showering is simulated within the H1 computing environment using the PYTHIA generator [60].

The LO cross section from [54,55] is corrected to the NLO calculation described in [56]. Briefly, this is done by reweighting each EPVEC event using the NLO cross section depending on the transverse momentum and rapidity of the W boson. The ACFGP [61] and CTEQ4M [62] parameterisations are used for the photon and proton structure functions respectively. The renormalisation and factorisation scales used are fixed to the W mass. The NLO corrections modify the LO cross section by $\pm\mathcal{O}(10\%)$, and significantly reduce the factorisation scale dependencies present in the original calculation. The theoretical uncertainty at NLO is 15% compared to 30% at LO. This error is attributed to the remaining uncertainties in the parton densities and the scale at which the calculation is performed [56].

The contribution of the charged current W production mechanism (given in equation 3.19 and illustrated in figure 3.9) is also calculated using EPVEC and included in the presented results. As previously stated, the total cross section is dominated by eW production, and the νW component is found to contribute less than 10% of the predicted signal rate.

The total W production cross section is $\mathcal{O}(1 \text{ pb})$ [53,54,56]. This figure is the sum of the contributions from $eW^{\pm}$ and $\nu W^{\pm}$ production, including all fermion decay channels in the subsequent process $W \rightarrow f\bar{f}'$.

3.4.3 W Decay Channels and Event Characteristics

The decay $W \rightarrow f\overline{f'}$ gives rise to final state particles in addition to those originating from the struck quark in the proton. The dominant branching ratio produces a quark – antiquark pair, $Br(W \rightarrow q\bar{q}) \approx 70\%$, which then form jets through the process of hadronisation. However, the identification of this decay channel suffers from a large QCD photoproduction background and the isolation of the W contribution is further complicated by three jet final states [63, 64].

The remainder of the branching ratio comes from the $W \to l\nu$ channel, where the W decays to leptons: an electron, muon or tau along with the corresponding neutrino, each leptonic decay channel contributing $\approx 10\%$. However, the unstable τ particle subsequently undergoes further (predominantly hadronic) decay making this particular channel difficult to identify. A search has been performed using the more common "1-prong" decay mode of the tau [63], but the results are dominated by CC background.

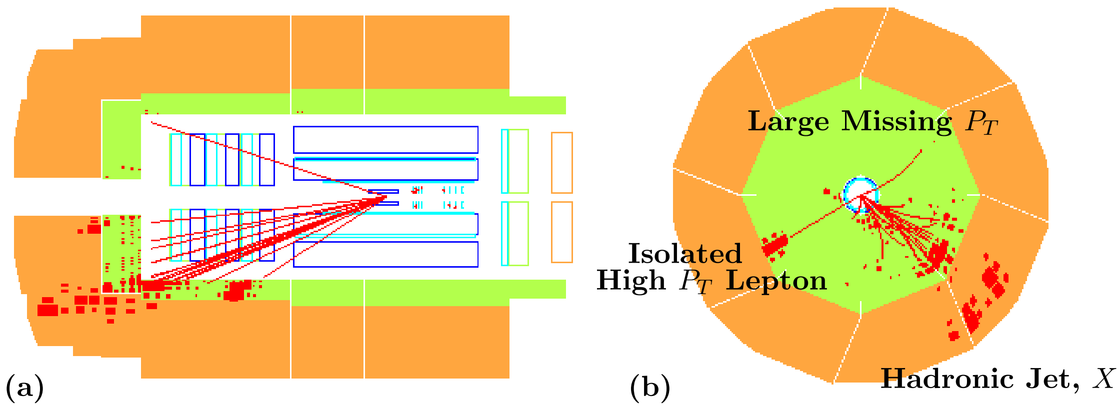

Figure 3.10: An $ep \to eWX$, $W \to e\nu$ candidate event recorded by the H1 detector. (a) The $r - z$ plane and (b) the $x - y$ plane.

In contrast to the above, the electronic and muonic decay channels provide a clean experimental signature, as illustrated in figure 3.10. The quark involved in the hard sub-process produces a hadronic jet, labelled X, most commonly in the forward direction. The decay products of the W are well separated from the X system, having originated from a different coupling vertex. The lepton is subsequently produced with a substantial P_T and is isolated with respect to X as seen in figure 3.10(b). Finally, a large missing P_T is present in the final state due to the neutrino, which passes straight out of the detector and remains undetected. The electron and muon W decay channels thus provide the signal process examined in this analysis.

The $W \rightarrow \tau\nu_\tau$ decay channel may also contribute to the signal rate via the leptonic tau decays $\tau \rightarrow \nu_\tau e \nu_e$ and $\tau \rightarrow \nu_\tau \mu \nu_\mu$. However, the low branching ratio limits this process to $< 10\%$ of the total signal contribution from W production, as confirmed by previous studies [65].

3.4.4 Z° Production

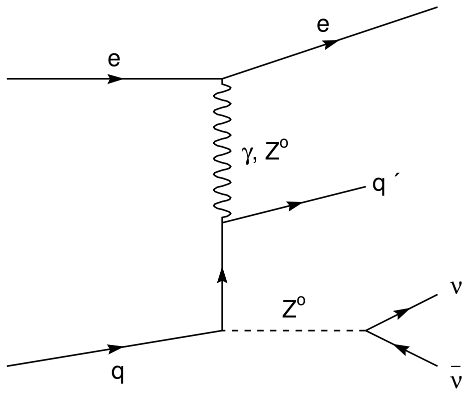

Figure 3.11: The leading order diagram for the process $ep \rightarrow eZ^\circ X$, including the subsequent decay $Z^\circ \rightarrow \nu\overline{\nu}$.

The electroproduction of Z°s may also contribute to the signal process of this analysis if the Z° decays to neutrinos, as illustrated in figure 3.11. This decay mode represents $\approx 20\%$ of the total Z° production cross section. Figure 3.11 may be viewed as an extension of the NC process with the additional *Z-strahlung* of the vector boson from the quark line. The outgoing electron may scatter into the detector providing the isolated lepton, while the neutrinos provide missing P_T. However, a combination of the low Q^2 dominance of the NC process (see figure 3.4) and the phase space cuts imposed in this analysis (see section 6.3) means that the main Z° contribution comes from the Cabbibo-Parisi process [66], as illustrated in figure 3.12. In this process a photon from the proton converts to an e^+e^- pair, one of which annihilates with the beam lepton forming the Z° boson, the other providing the isolated lepton.

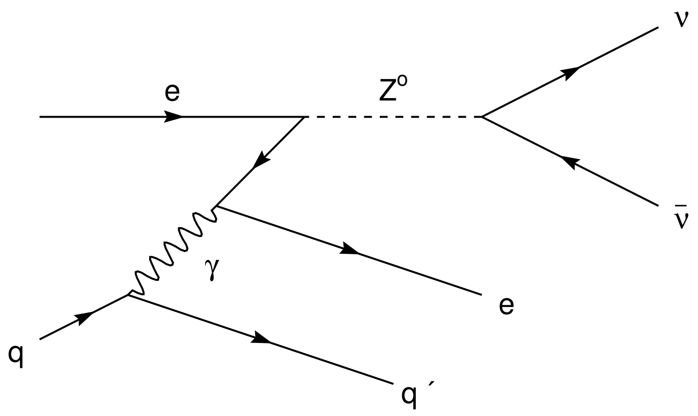

Figure 3.12: The Cabbibo-Parisi process, with subsequent $Z^\circ \rightarrow \nu\overline{\nu}$ decay.

The prediction from the $Z^\circ \rightarrow \nu\overline{\nu}$ process is calculated using the EPVEC generator and is added to that from W production. This contribution is found to contribute less than 5% of the total signal rate.

3.5 Beyond the Standard Model

This section briefly outlines two areas of interest in the study of W production at HERA. Firstly, the $WW\gamma$ coupling is discussed, followed by a description of the production of single top quarks. Further discussion of BSM processes relevant to this field may be found in [67–72].

3.5.1 The $WW\gamma$ Coupling

The sensitivity of the W production mechanism to triple boson couplings (TBCs) allows this particular corner of the electroweak sector of the SM to be tested. At

HERA, the dominant production mechanism involves gamma exchange due to the large mass of the Z° boson, so that the TBC eW production process is sensitive only to the $WW\gamma$ coupling. As depicted in figure 3.8(c), the photon couples to a virtual W from the proton and the real W decays to a fermion pair. This coupling may also be tested in W pair production at LEP, in combination with the WWZ coupling, which contributes equally to the $e^+e^- \rightarrow W^+W^-$ s-channel process [73].

The $WW\gamma$ coupling is parametrised in terms of a general Lorentz invariant Lagrangian, containing seven independent complex couplings [74]. This number is reduced to two, κ_γ and λ_γ when electromagnetic gauge invariance and CP conservation are assumed. In the SM,

$$\kappa_\gamma = 1 \quad \text{and} \quad \lambda_\gamma = 0 \tag{3.23}$$

so deviations from these equalities, referred to as *anomalous gauge couplings*, may be a sign of new physics. Recent combined results from the four LEP experiments [75] found no significant deviation from the SM values, with limits set as

$$\kappa_\gamma = 0.943^{+0.055}_{-0.055} \quad \text{and} \quad \lambda_\gamma = -0.020^{+0.024}_{-0.024} \tag{3.24}$$

3.5.2 Single Top Production

The production of single top quarks in ep collisions may proceed via two different production mechanisms. The top quark subsequently weak decays to a b quark, which then hadronises forming a jet. The decay products of the W boson and the scattered lepton complete the final state. Within the SM, top quarks may be produced singly in CC interactions as illustrated in figure 3.13(left). However, due to the W propagator term and the small quark coupling constants given by the CKM matrix [76] elements V_{td} and V_{ts}, this interaction is completely negligible at

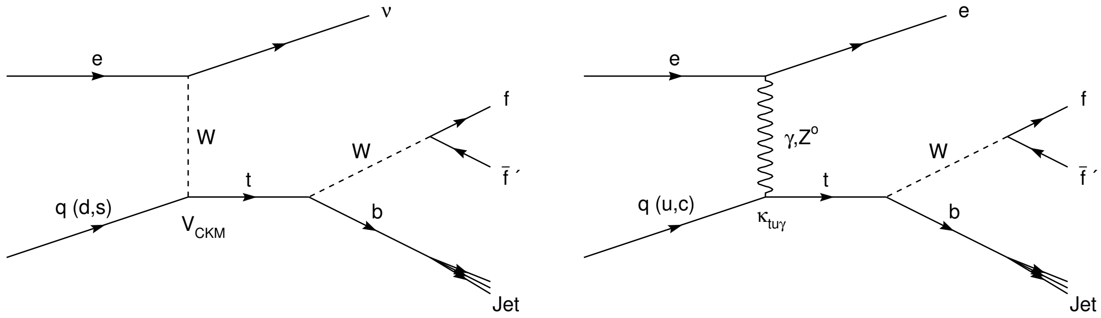

Figure 3.13: Standard Model (left) and FCNC (right) single top production.

HERA.

Several publications [77] discussing Flavour Changing Neutral Current (FCNC) interactions have pointed to a significant single top contribution at HERA from the process shown in figure 3.13(right). The b quark jet is expected to have significant hadronic transverse momenta, having originated from a top decay. Therefore at large values of hadronic transverse momentum, P_T^X, W production will be a significant background to this process. A recent H1 measurement [78] placed an upper limit on the anomalous magnetic coupling $\kappa_{tu\gamma} < 0.27$, equivalent to a cross section limit of

$$\sigma(ep \to e + t + X, \sqrt{s} = 319GeV) < 0.55pb \qquad \text{at } 95\% \;\; \text{CL} \tag{3.25}$$

This limit is competitive with results at other high energy colliders [79, 80], as shown in figure 3.14. Furthermore, the upper limit on the cross section does not rule out the detection of FCNC interactions at HERA.

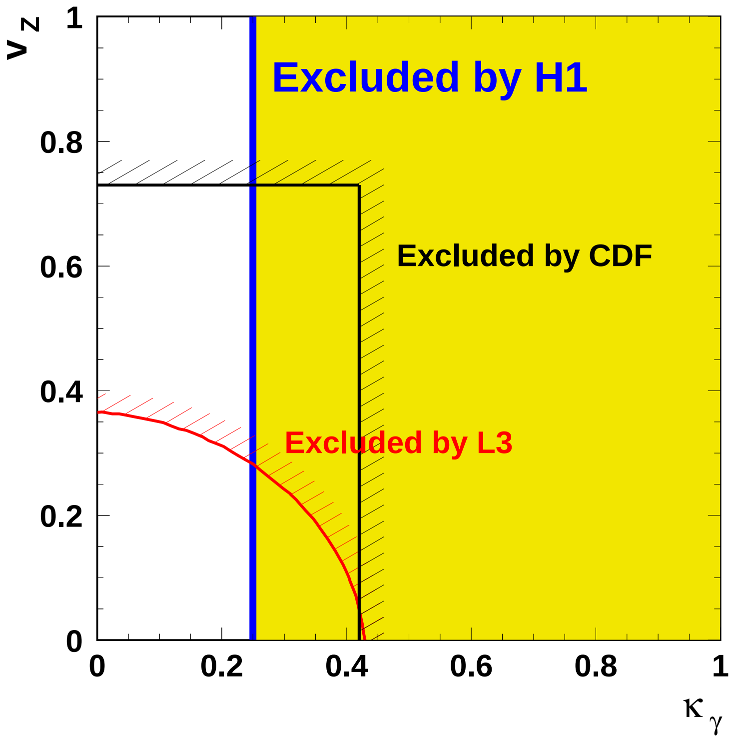

Figure 3.14: Exclusion limits at 95% CL on the anomalous magnetic coupling $\kappa_{tu\gamma}$ obtained at HERA (H1) [78], TeVatron (CDF) [79] and LEP (L3) [80]. The CDF and L3 limits on the anomalous tqZ vector coupling v_Z are also shown. Taken from [78].

3.6 Background Processes

This section presents a summary of other physics processes expected to contribute as background to this analysis, including how they may mimic the topology of signal events. Reduction of this background is vital in order to obtain a clean sample of such a relatively rare process. Background study selections are discussed in chapter 7. The Monte Carlos used for the simulation of each background process are also introduced here; the Monte Carlo used to model signal events is discussed in section 3.4.2.

3.6.1 Neutral Current

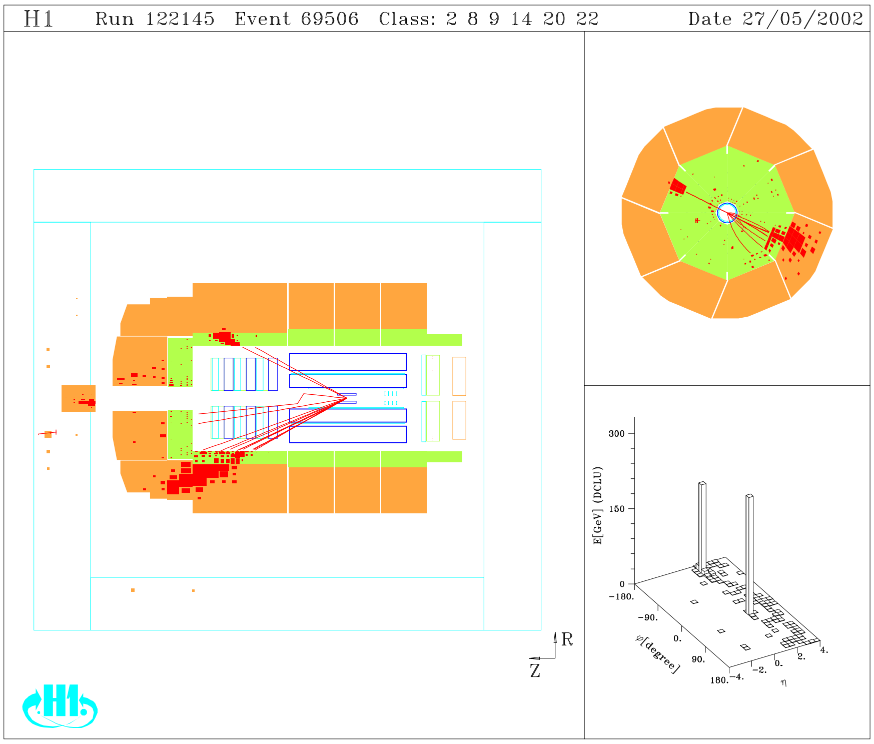

Figure 3.15: A typical NC event recorded at H1.

The NC process, as illustrated in figure 3.1(left), is a potential source of background to signal events containing isolated electrons. A typical event is displayed in figure 3.15. Since the scattered electron is well separated from the hadronic jet, it could be misinterpreted as a W decay electron. However, from the $x - y$ view of figure 3.15 it can be seen that the event is intrinsically balanced in P_T. Therefore, missing P_T can only be introduced into the event through limited geometrical acceptance of the detector or fluctuations in the shower development of the final state particles. The event generator RAPGAP [81] was used to calculate the NC contribution to the background rate.

3.6.2 Charged Current

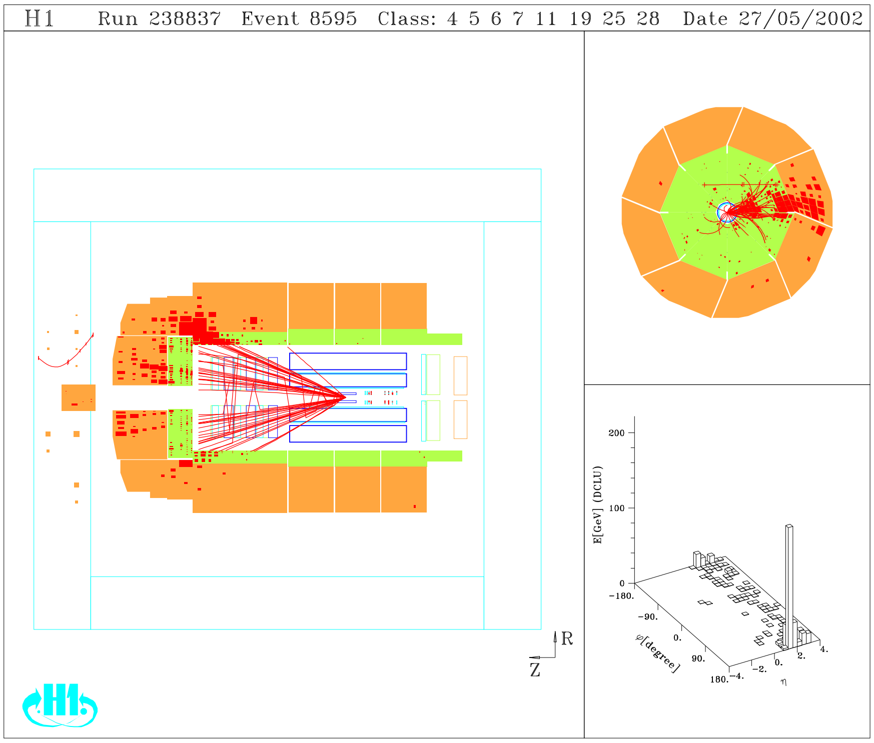

Figure 3.16: A typical CC event recorded at H1.

CC events are much rarer than NC events (see section 3.3.1), but contain a neutrino in the final state as shown in figure 3.1(right), leading to an intrinsic P_T imbalance. This can be seen in the x-y view of figure 3.16, in stark contrast to the equivalent NC picture in figure 3.15. If a particle produced in the hadronisation process is separated from the main body of the jet it may be misidentified as an isolated lepton, enabling the event to enter the signal sample. Therefore, the CC process is a source of background to both electron and muon signal events. The event generator DJANGO [82] was used to calculate this background contribution.

3.6.3 Photoproduction

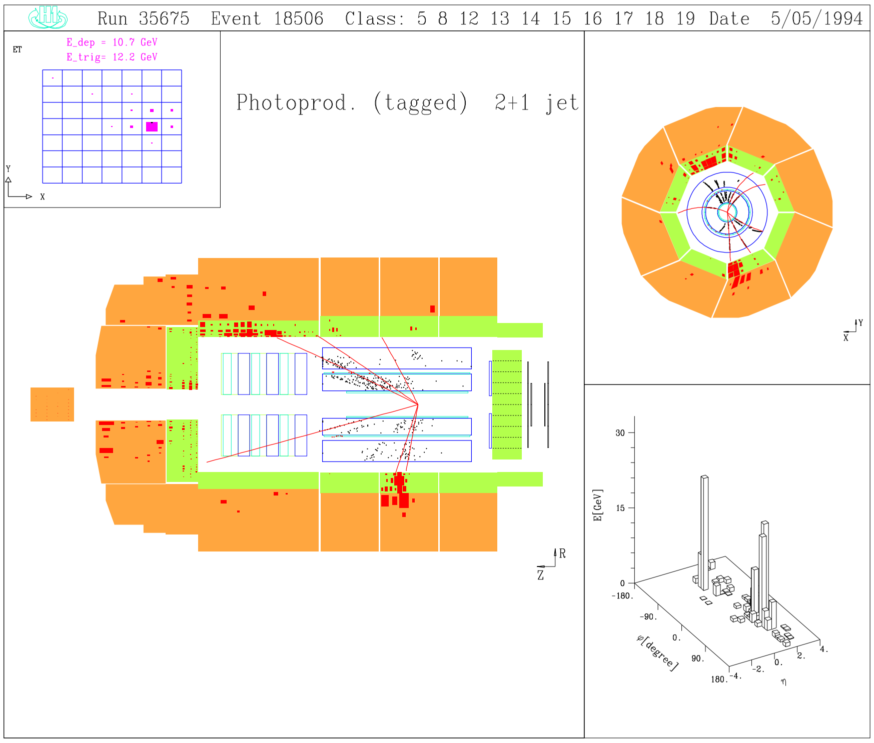

Figure 3.17: A typical tagged-photoproduction event recorded at H1.

Photoproduction events (figure 3.2) may enter the signal sample if there is reconstructed missing transverse momentum. One of the hadronic jets may consist of a single isolated hadron, which is subsequently misidentified as a lepton. This signature may be generated by the hadronic particle decaying to a muon or from a particle traversing the detector without significant hadronic interaction. A typical photoproduction event is shown in figure 3.17, featuring two hadronic jets and a tagged electron. The event generator PYTHIA [60] is used to calculate the SM prediction from photoproduction, including the prompt-photon contribution. If a heavy quark pair (for example $b\bar{b}$) is produced, then leptonic weak decays are possible with associated missing P_T. Therefore a further event generator, AROMA [83], is also included to model this specific scenario. All photoproduction contributions are reweighted as described in section 6.4.

3.6.4 Lepton Pair Production

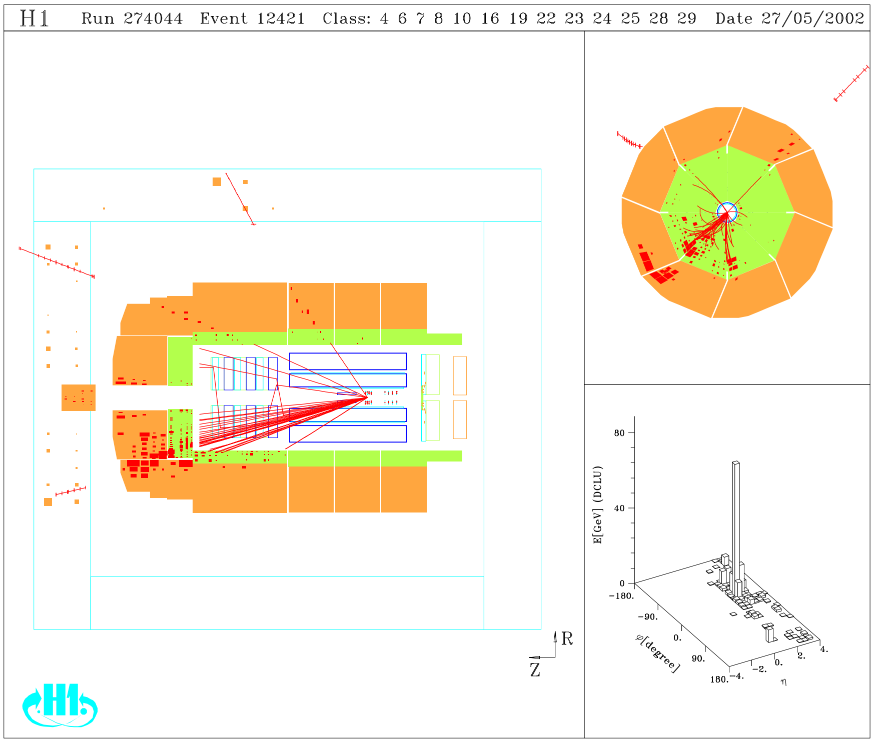

Figure 3.18: A typical inelastic muon pair production event recorded at H1.

Lepton pair production via photon-photon interactions can contribute to the background if one lepton escapes detection. This process is illustrated in figure 3.19. A typical inelastic event is shown in figure 3.18, where a $\mu^+\mu^-$ pair is produced, and is detected along with the hadronic jet from the interacting quark. If one lepton is undetected, a momentum imbalance is introduced into the event and the topology is thus similar to the signal process. More details on lepton pair production at HERA may be found in [84, 85].

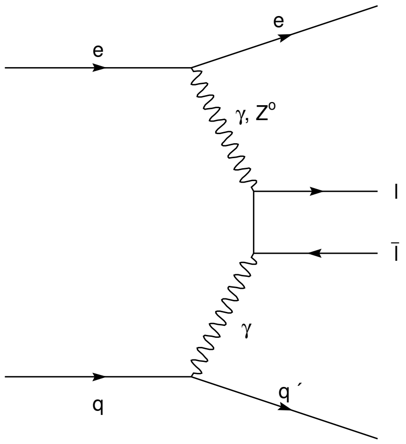

Figure 3.19: An example of lepton pair production in ep scattering.

The event generator GRAPE [86], which includes all diagrams and NLO corrections, is used to calculate the predicted rate from this process. The dominant contribution, lepton pair production via photon-photon processes, is found to be compatible with the prediction given by a second generator, LPAIR [87]. Di-lepton J/ψ events are also included in this contribution, calculated using the event generator EPJPSI [88].

Chapter 4

Initial Selection Criteria

This chapter outlines the basic criteria applied to all subsequent selections employed in this analysis to obtain a clean physics sample.

4.1 Run Selection

Each HERA *fill* of colliding protons and electrons (see section 2.1) is recorded by H1 in a series of data taking *runs*. Detector conditions may vary during runs and luminosity fills, so a *good run* selection is performed on all of the recorded data used in this analysis. This selection is based mainly on high voltage (HV) conditions of certain detectors essential for this analysis. The central tracker HV must be on, namely the central jet chambers CJC1/2 and the central proportional chambers COP/CIP. The LAr must also be on, as well as the ToF system and the Lumi system. Additionally, any runs lasting less than 30 seconds are also excluded.

4.2 Vertex Position

The interaction vertex is required to be in the region -40cm $< Z_{vtx} <$ 100cm, reconstructed from either central or forward tracks in the event. This cut has been extended into the forward region after investigating events with low track multiplicities or primarily forward tracks [89]. In such events, some of the MC models employed in this analysis show a shift of the reconstructed vertex to higher values, resulting in an extended tail in the vertex distribution. This is shown in figure 4.1 for the DJANGO CC Monte Carlo.

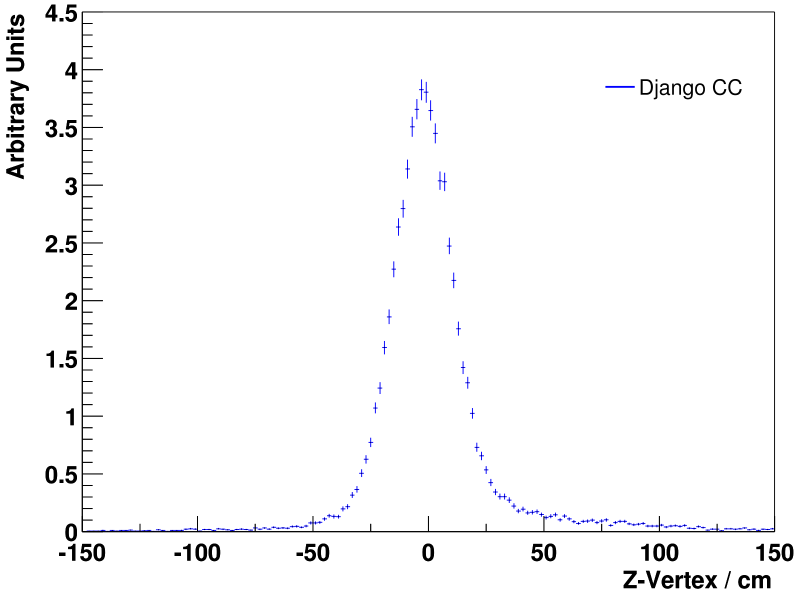

Figure 4.1: The reconstructed z-vertex distribution of Django CC events with low central track multiplicities or forward tracks only.

The data sample may also suffer from poor reconstruction, resulting in a wrong primary vertex assignment. Therefore, the upper cut limit is extended to accept vertices in the forward region. This also results in an increase in data luminosity of $\approx 5\%$.

4.3 Non *ep* Background Rejection

The vast majority (over 99%) of non *ep* background is removed using the Time of Flight detectors, as outlined in section 2.6. However, two further methods are employed to minimise this unwanted contribution to the data sample.

The first of these uses timing information from the CJC. The drift time to the wires in the CJC provides a measurement of when the event took place, referred to as its T0. Events with a T0 not within $\pm$ 5ns of a bunch crossing are unlikely to have originated from an *ep* collision and are therefore rejected.

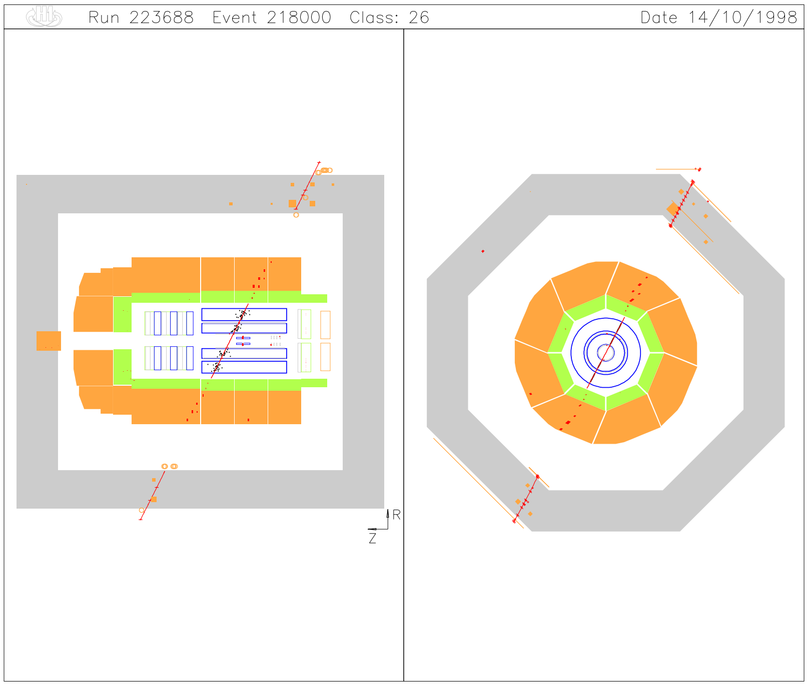

Figure 4.2: A cosmic muon event within H1.

The remainder of the non *ep* background comes from cosmic muon events, an example of which is shown in figure 4.2, and any remaining beam-halo muons (see figure 2.11 (bottom)). A set of topological background finders [90] is employed to perform this background rejection, using pattern recognition in different sub-detectors. Beam-halo muons are tagged using hits parallel to the beam axis in the Iron, LAr and SpaCal. Cosmic muons are tagged using reconstructed track information from the LAr, Iron and CTD. Both methods similarly define a cylinder around the candidate background muon, where the energy outside this cylinder must be much less than that contained within it. The background finders are also applied to the Monte Carlos used in this analysis. Those finders firing more than $\approx 1\%$ of EPVEC events are not used to maintain a high selection efficiency for the signal process.

4.4 Trigger Selection

A triggering system is employed at H1, as described in section 2.8, to select only genuine physics events of interest. The following outlines the triggers used in this analysis and describes the calculation of the corresponding trigger efficiency, ε, where the generic formula is given by[1]

$$\varepsilon = \frac{\text{Sum of all weights of selected events firing at least one subtrigger}}{\text{Sum of all weights of selected events}} \tag{4.1}$$

4.4.1 LAr Triggers

The main trigger selection used in this analysis was developed for the H1 Charged Current analysis [41, 43]. The principal trigger elements are based on an imbalance of energy deposits or a high energy deposit in the LAr, indicating missing transverse momentum or an electron signature respectively. These elements are combined with event timing information from the proportional chambers or the LAr to form the L1 subtriggers[2]. No prescales (see section 2.8) are applied to the LAr triggers due

[1] The event "weight" is equal to 1 for data events, whereas MC events are weighted with respect to the luminosity of the data.

[2] One of the subtriggers, namely ST71, has an additional L2 condition. See [41].

the rare nature of CC (and signal) events.

The evaluation of the trigger efficiency of the LAr triggers is performed using a *pseudo-CC* data sample [91], due to the infrequent nature of CC events (see section 3.3.1). Pseudo-CC events are formed by removing the scattered electron in a large sample of independently triggered NC events from all subdetectors, leaving the event indistinguishable from a real CC event. Each event is then reweighted with respect to the CC cross section, to ensure kinematic quantities are reproduced correctly. This method relies on the similarity of the hadronic final state in NC and CC events; independent studies have verified this assumption [92]. The trigger efficiency is given by the following, modified version of equation 4.1 as

$$\varepsilon = \frac{\text{Sum of all weights of selected pseudo-CC events firing at least one subtrigger}}{\text{Sum of all weights of selected pseudo-CC events}} \tag{4.2}$$

The trigger efficiency of the LAr triggers is greater than 98% for events containing electrons with transverse momentum greater than 10 GeV. For events with an imbalance of calorimetric transverse momentum greater than 12 GeV the trigger efficiency is 60%, rising to 90% for an imbalance greater than 25 GeV [43].

The LAr trigger efficiency is shown for pseudo-CC events compared with the CC Monte Carlo (see section 3.6.2) as a function of hadronic transverse momentum and angle in figure 4.3. It is clear that that the data are not described by the simulation, so the trigger efficiency is always determined from the pseudo-CC data events and all Monte Carlos are reweighted accordingly, to allow an accurate comparison to the data. This reweight is done by fitting a 2D function to the data in bins of hadronic transverse momentum and angle. Different fit parameters are used for each of the major data taking periods to take into account small differences in the trigger definitions.

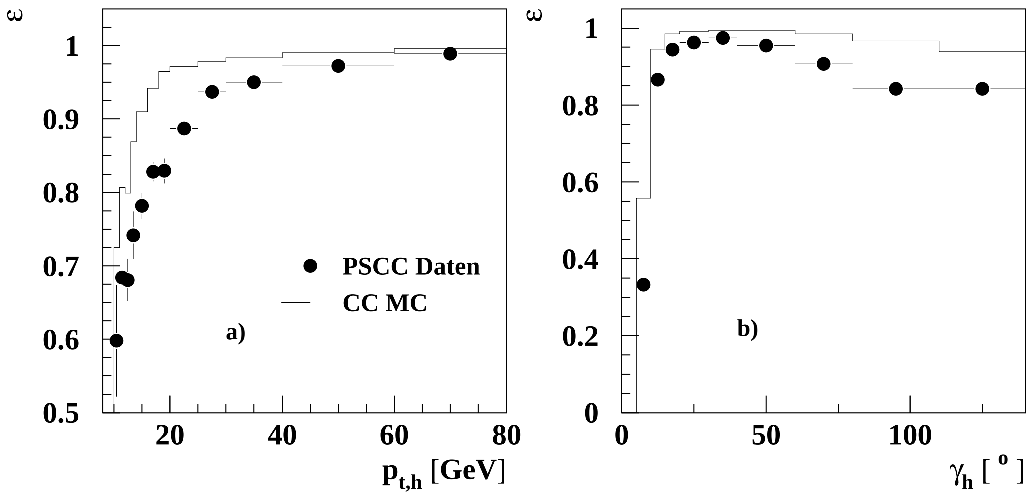

Figure 4.3: The combined trigger efficiency of the LAr triggers, as a function of a) hadronic transverse momentum, $p_{t,h}$ and b) hadronic angle, γ_h. Taken from [93].

4.4.2 Muon Triggers

In addition to the LAr triggers a set of muon triggers are also employed, a full description of which can be found in [85]. The triggers are based on the coincidence of a signal in the muon system with z-vertex and limited central track information to form several muon L1 subtriggers. During periods of high luminosity, prescales (see section 2.8) are applied to the muon triggers due to the higher background rates. These prescales are taken into account in simulated events by applying an appropriate reweight.

The efficiency of the three muon trigger elements used in these subtriggers is shown in figure 4.4 as a function of muon polar angle. The data are compared to the LPAIR Monte Carlo and are found to be in good agreement. The z-vertex and track trigger elements are also found to be well described by the simulation [85]. The efficiency of the muon triggers to trigger muon signal events is calculated using EPVEC and from equation 4.1 is estimated to be 31%, rising to 52% in the central region of the detector and falling to 13% in the forward region.

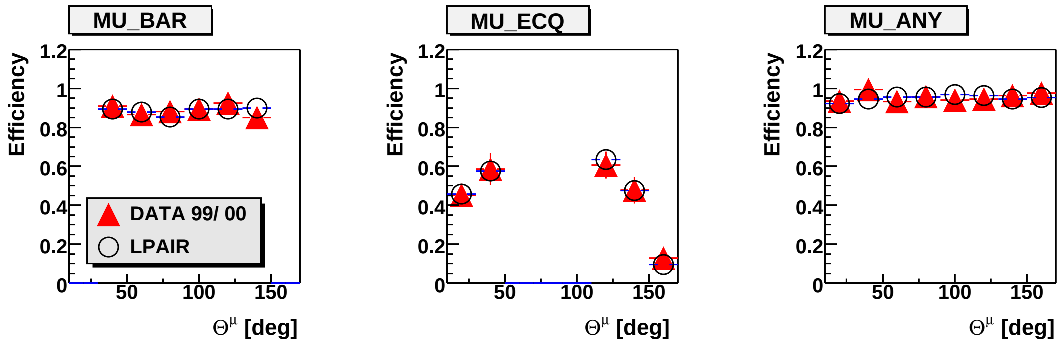

Figure 4.4: Trigger efficiencies of the muon trigger elements used by the muon subtriggers applied in this analysis as a function of muon polar angle, θ^{μ}. Taken from [85].

4.4.3 Trigger Selection Summary

Trigger	Description of Main Criteria
LAr_electron	A high energy LAr electron signature in coincidence with timing information from the LAr or proportional chambers
LAr_Etmiss	An imbalance of LAr energy deposits in coincidence with timing information from the LAr or proportional chambers
Muon	A signal in the muon system in coincidence with central track and z-vertex information

Table 4.1: A summary of the triggers used in this analysis. Further details of the LAr triggers may be found in [41]; further details of the muon triggers may be found in [85].

Chapter 5

Studies for a New High P_T Muon Trigger

This chapter describes feasibility studies performed for a new dedicated high P_T muon trigger. The design presented incorporates the new Fast Track Trigger (FTT), part of the HERA II upgrade at H1, which is entering final commissioning at the time of writing. The use of the FTT to trigger high P_T charged particles, including those produced in signal events in this analysis, was originally considered in [31].

The need for such a trigger is first introduced, followed by a brief description of the FTT, focussing on the parameters relevant to this study. The new proposed trigger selection is then described and the expected performance compared to the existing triggers used in this analysis. Finally, the results of this study are summarised and future work is outlined.

The Monte Carlo generator EPVEC (see section 3.4.2) is used in this study to simulate W production events with subsequent leptonic decay, providing the signal topology of interest. All trigger efficiencies are calculated using equation 4.1, which includes all geometrical and acceptance effects.

5.1 Triggering Muon Signal Events at Low P_T^X

The efficiency of the LAr triggers used in this analysis to trigger signal events is displayed as a function of P_T^X in figure 5.1. The efficiency to trigger all events is shown in figure 5.1(a), where a notable drop is visible towards low values of P_T^X. This distribution may be further examined by selecting events containing high P_T leptons[1]. As detailed in section 4.4.1, the LAr trigger selection includes electron triggers with very high efficiencies as well as triggers based on missing calorimetric energy. This can be seen in figure 5.1(b), where the efficiency to trigger signal events containing high P_T electrons is almost 100% except at very low P_T^X. This may be contrasted with figure 5.1(c), the equivalent distribution for events containing high P_T muons, where the trigger efficiency falls to 14% for events with $P_T^X < 12$ GeV.

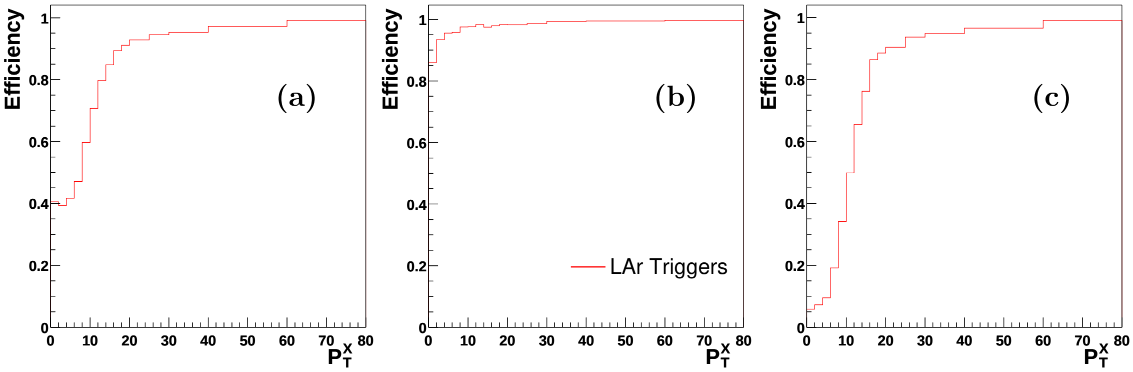

Figure 5.1: Trigger efficiency for EPVEC events of the LAr triggers as a function of P_T^X: (a) All events, (b) events containing a $P_T^e > 10$ GeV electron and (b) events containing a $P_T^\mu > 10$ GeV muon. P_T^X is measured in GeV.

As explained in section 2.5, muons largely escape detection in the calorimeter. Consequently, in muon signal events only the hadronic system will deposit significant energy in the LAr, so that any missing calorimetric transverse momentum is approximately equal to P_T^X. As calorimetric energy is the basis of the LAr triggers,

[1]Lepton identification is described in section 6.1.

the total missing P_T in high P_T muon events is small at low P_T^X, leading to the observed fall in trigger efficiency in figure 5.1(c). Several muon triggers are also included in this analysis to increase the selection efficiency of muon signal events at low P_T^X (see section 4.4.2). However, the efficiency of these triggers to trigger muon signal events is estimated to be only 31% on average, falling to 25% for events with $P_T^X < 6$ GeV.

The remainder of this study examines signal events containing a $P_T^\mu > 10$ GeV muon, describing the design and expected performance of a new trigger for future use in this analysis.

5.2 The Fast Track Trigger

The FTT [31] is a new track based trigger system, designed to improve selectivity in order to cope with the expected higher event rates in H1 due to the HERA II upgrade. The FTT will provide 3D reconstruction of charged particle tracks in the CJC and has a high efficiency for tracks with P_T as low as 100 MeV [94]. It also has a much improved resolution compared to the existing DCRϕ trigger [95].

The triggering process is based on hits in four groups of three layers of wires in each CJC cell; three groups in CJC1 and one in CJC2, as illustrated in figure 5.2. Up to 48 tracks per event may be reconstucted and used in trigger algorithms by the three stage trigger system, in the angular range $25° < \theta^{track} < 155°$. Level 1 (L1) will provide coarse $r - \phi$ position resolution and track segment finding in order to make trigger decisions within 2.3 μs of the interaction. Level 2 (L2), which has a longer latency of 23 μs, will perform track segment linking and provide trigger decisions on kinematic quantities and vector meson resonances based on combinations of the reconstructed tracks. Level 3 (L3) will give partial event reconstruction and particle identification of, for example, D* mesons on a timescale of < 100 μs.

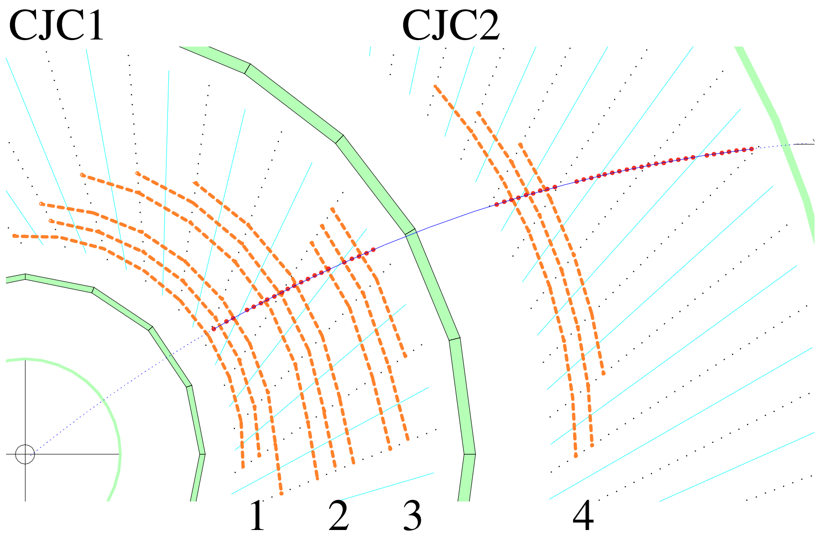

Figure 5.2: A charged particle track traversing the four layers of the CJC used to trigger tracks by the FTT.

The performance of the FTT is simulated using a dedicated software package [96] to determine the expected efficiencies and resolutions from the new trigger. Those relevant to this study are discussed below.

The L1 track finding efficiency of the FTT within the previously stated angular range is found to be greater than 90% for 100 MeV tracks, using a single hit efficiency of 95% [31]. For tracks with $P_T^{track} \geq 1$ GeV, this increases to greater than 99%. The track finding efficiency is reduced by up to 10% if the single hit efficiency is reduced to 90%, although this reduction is not expected during normal running [97]. For this study, which is concerned with high P_T tracks in a suitable θ range, the track finding efficiency is assumed to be 100%.

The momentum resolution of the FTT in $(1/P_T)$ is also derived from the simulation and is given as $\sigma(1/P_T) = 0.3$ GeV^{-1} on L1 and $\sigma(1/P_T) = 0.015$ GeV^{-1} on L2 [98][2]. These resolutions are used to calculate the P_T^{track} thresholds used in the

[2]It should be noted that these are the latest estimated resolutions and differ from those in [31,97],

new trigger.

5.3 A New High P_T Muon Trigger

A new trigger is simulated by selecting events containing "good" high P_T tracks[3] in the angular range of the FTT, assuming an 100% track selection efficiency. However, due to the finite momentum resolutions defined above, the lower bound on the track momentum must be lower than the $P_T^{\mu} > 10$ GeV cut performed in this analysis (see section 6.3). At L1, due to the relatively poor resolution, this corresponds to selecting $P_T^{track} \gtrsim 1.5$ GeV to measure 97.5% of 10 GeV tracks[4]. At L2, where the momentum resolution is much better, this lower bound can be increased to $\approx$ 8 GeV and used to verify the L1 signal. Therefore, this is taken as the L2 track momentum cut in this study and a new trigger combination *Track* is formed, given by the following equation[5]

$$Track \;:\; P_T^{track} > 8 \text{ GeV} \quad \&\& \quad 25^\circ < \theta^{track} < 155^\circ \tag{5.1}$$

The efficiency of this combination to trigger muon signal events is found to be on average $\approx 65\%$, rising to $\approx 73\%$ for $P_T^X > 12$ GeV and falling to $\approx 60\%$ for $P_T^X <$ 12 GeV.

Another important consideration in the design of a new trigger is the expected *rate*. As mentioned in section 2.8, the bunch crossing frequency at HERA results in an interaction rate of 10 MHz. Post-upgrade limits on trigger rates are set as 1000 Hz from L1 and 200 Hz from L2 [100]. The expected L2 rate reduction factor with a high momentum track requirement in the FTT is shown in figure 5.3, obtained

where the L1 (L2) resolution is quoted as slightly better (worse).

[3]The track definition comes from the H1 software package `H1PHAN` [99].

[4]This figure represents all but the lower tail of 2σ of the resolution distribution.

[5]A && B represents the logical AND of A and B.

using a sample of track triggered events [31]. For a cut on P_T^{track} of 8 GeV, as chosen in this design, this results in a reduction factor of approximately 15. Independent studies [101] have confirmed this result with the full L2 FTT simulation using an L2/L4 transparent run[6] and a suitable L1 monitor trigger, yielding a rate of ≈ 25 Hz for *Track* from L2 [102].

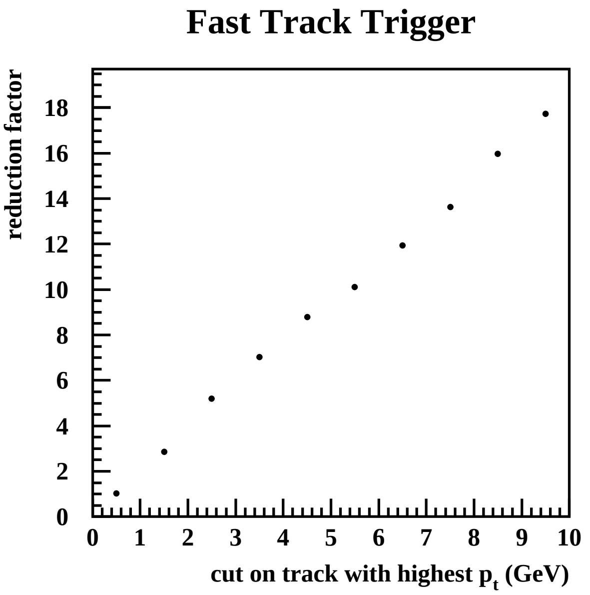

Figure 5.3: FTT rate reduction factor for a sample of track triggered events as a function of the cut on the highest P_T track in the event. Taken from [31].

Although this rate is within the 200 Hz limit at L2, it is still too high for an individual subtrigger. To remedy this, *Track* is combined with the L1 trigger element *Mu_Any*, which requires hits in either the barrel or endcaps of the central muon system. This lowers the efficiency of the new trigger by $\approx 20\%$ across all P_T^X, but is expected to lower the rate sufficiently to $\mathcal{O}(1\text{ Hz})$, as predicted in [31]. The efficiency of *Track* trigger based combinations to trigger muon signal events is illustrated in figure 5.4 as a function of P_T^X.

Event timing may also be included using the L1 trigger element *Zvtx_T0*, which

[6]L2/L4 transparent runs contain data recorded with no L2 or L4 trigger filtering and are used to measure the unbiased performance of individual triggers.

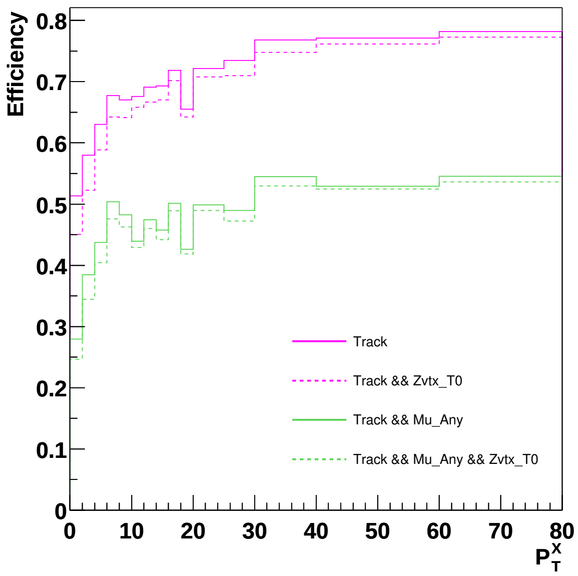

Figure 5.4: The trigger efficiency of *Track* trigger based combinations as a function of P_T^X for EPVEC events containing a muon with $P_T^\mu > 10$ GeV. P_T^X is measured in GeV.

constrains the reconstructed event vertex to the interaction region using information from the CIP and COP. This has a negligible effect on the efficiency to trigger signal events, as shown in figure 5.4, but is included in many existing subtriggers to eliminate background from beam-gas or beam-wall interactions. The final combination[7] of the new central subtrigger selection is given by

$$New\ Central\ :\ Track\quad \&\&\quad Mu\_Any\quad \&\&\quad Zvtx\_T0 \tag{5.2}$$

[7]On L1, the P_T^{track} threshold of *Track* would be reduced to 1.5 GeV, due to the momentum resolutions discussed in this section.

5.4 The Forward Region

Studies have also been performed on post-upgrade triggering in the forward region of H1, specifically involving the forward muon system [103]. A muon signal event selected by this analysis contains associated muon track hits in the FMD, as illustrated in figure A.10. These hits are combined to produced an L1 trigger signal by the trigger element *FwdMu_Val_Any*, which requires pre- and post-toroid hits in the same theta octant (see section 2.5.2) to provide a *validated* track. Further validation in the forward region will also be possible after the upgrade by matching L2 tracks provided by the CIP [103], although this is not implemented in this study.

The *FwdMu_Val_Any* trigger element is found to be ≈ 14% efficient in triggering muon signal events across all P_T^X. A new forward subtrigger is formed by combining *FwdMu_Val_Any* with *Zvtz_T0*, to give

$$New\ Forward\ :\ FwdMu\_Val\_Any\quad \&\&\quad Zvtx\_T0 \tag{5.3}$$

The timing requirement is again included to reduce expected background rate, which is higher in the forward region due to secondary scattering of the proton remnant with the beam pipe walls. The efficiency of *New Forward* to trigger muon signal events is illustrated in figure 5.5. Only in events at very low P_T^X does the Zvtz_T0 trigger element cause a significant loss in efficiency, as these events contain few tracks in the CIP or COP.

5.5 Results

Two new subtriggers, *New Central* (equation 5.2) and *New Forward* (equation 5.3), have been investigated for future use in this analysis. A summary of the calculated

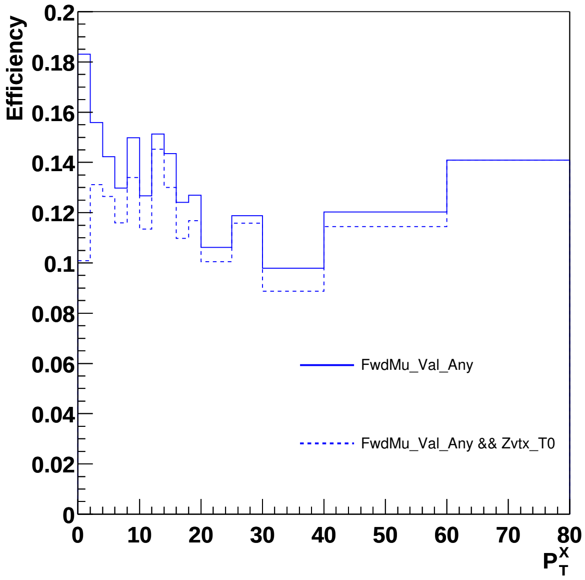

Figure 5.5: The trigger efficiency of *FwdMu_Val_Any* based combinations as a function of P_T^X for EPVEC events containing a muon with $P_T^\mu > 10$ GeV. P_T^X is measured in GeV.

trigger efficiencies of the new triggers is presented in table 5.1[8]. The efficiencies of the triggers currently used in this analysis are also shown.

For muon signal events with $P_T^X > 12$ GeV, the combination of the LAr and current muon triggers is over 90% efficient. For $P_T^X < 12$ GeV, the efficiency of this combination falls to 38%, highlighting the problematic region as detailed in section 5.1. The new muon trigger combination of (*New Central* $\|$ *New Forward*) is found to be approximately 20% more efficient than the current muon triggers both at $P_T^X <$ 12 GeV and $P_T^X < 6$ GeV, as illustrated in figure 5.6(a), equivalent to more than a factor of 2 improvement.

The efficiency of the new and current muon triggers in combination with the LAr triggers is shown in figure 5.6(b). As detailed in table 5.1, the new muon trigger

[8] A $\|$ B represents the logical OR of A and B.

Trigger Combination	Trigger Efficiency, ε			
	All P_T^X	$P_T^X < 6$	$P_T^X < 12$	$P_T^X > 12$
LAr Triggers	0.41	0.07	0.14	0.89
Current Muon Triggers	0.31	0.25	0.29	0.34
LAr $\|\|$ Current Muon	0.58	0.30	0.38	0.92
New Central	0.41	0.33	0.37	0.49
New Forward	0.12	0.12	0.12	0.11
New Central $\|\|$ New Forward	0.52	0.45	0.48	0.57
LAr $\|\|$ New Central	0.70	0.37	0.44	0.93
LAr $\|\|$ New Central $\|\|$ New Forward	0.74	0.48	0.54	0.94

Table 5.1: Summary of calculated trigger efficiencies, using EPVEC events containing a muon with $P_T^\mu > 10$ GeV. P_T^X is measured in GeV.

combination increases the total trigger efficiency by 16% for muon signal events at $P_T^X < 12$ GeV and 18% at $P_T^X < 6$ GeV. The *New Forward* trigger, which has a uniformly low efficiency, adds $\approx 10\%$ to the new trigger combination at low P_T^X.

5.6 Conclusions and Future Work

Only when the FTT is fully installed can the new triggers described in this study be fully tested. Of particular importance is the measured rate, not only to verify the results of the simulation on L2 described in section 5.3, but also on L1.

If the rate of *New Central* is lower than expected, the inclusion of *Mu_Any* may not be necessary, resulting in an increase of efficiency in the central region of $\approx$ 20% to trigger muon signal events (see figure 5.4). Furthermore, by not demanding a muon signature the trigger would be more generic, and could be used to select

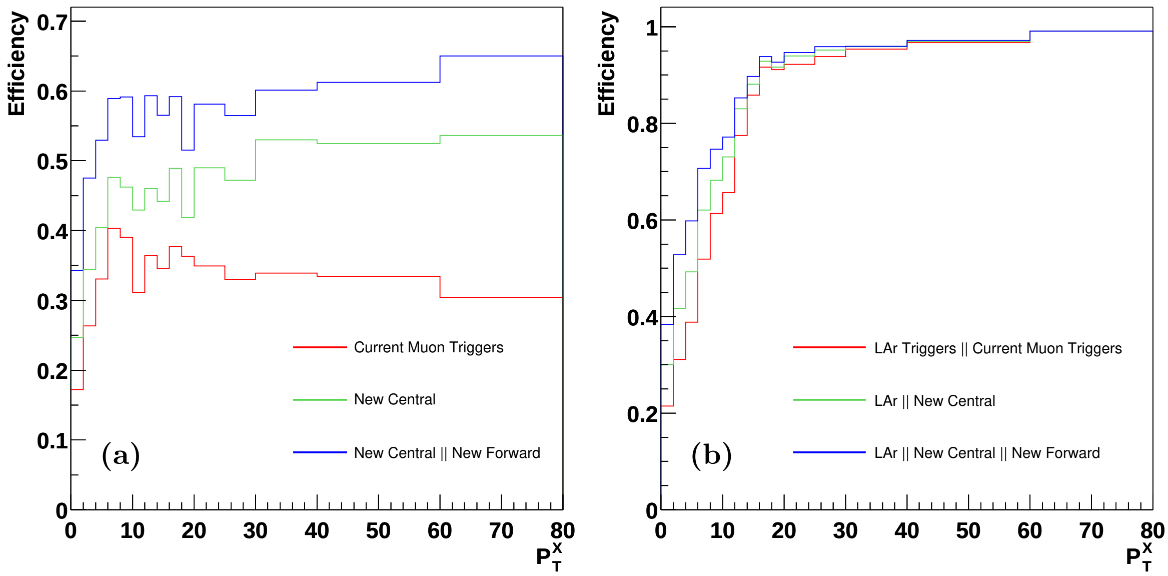

Figure 5.6: Comparison of trigger efficiencies of existing and new trigger combinations to trigger EPVEC events containing a muon with $P_T^{\mu} > 10$ GeV: (a) Comparison of new and current muon triggers, (b) Comparison of new and current muon triggers in combination with the LAr triggers. P_T^X is measured in GeV.

other processes producing single charged particles of several GeV, for example in the hadronic decays of bottom mesons [31]. In addition to the design presented here, track isolation criteria may also be applied to *New Central* by the FTT on L3 [97].

The rate of *New Forward* also needs investigation. A similar subtrigger to *New Forward* is already in use, which includes hits from the forward endcaps of the central muon system. The rate of this trigger was ≈ 0.2 Hz on L2 during the 2000 data taking period, although the efficiency to trigger muon signal events is found to be approximately half that predicted by *New Forward*, due to the inefficiency of the central muon system. The matching of CIP tracks or those provided by the new FTi2 [104] on L2 should also be included in this design.

If the results of this study and the simulations of the FTT are reproduced when the system is installed, improved triggering of high P_T tracks in the central region will be available for future analyses in H1. The new trigger selection presented here will provide improved triggering of muon signal events in this analysis. This will allow the phase space cut on missing calorimetric energy (see section 6.3) to be lowered for events containing high P_T muons, enabling a higher selection efficiency (see section 8.3) at low P_T^X .

Chapter 6

Particle Identification and Event Kinematics

The main process expected to contribute to this analysis is SM W production, a rare event at HERA with a total cross section $\mathcal{O}(1\text{ pb})$ as detailed in section 3.4.2. The rare nature of this process demands that any selection criteria are carefully defined, not only to accept as much signal as possible but also to reject unwanted background processes. A typical event is characterised by an isolated, high P_T lepton (electron or muon), a hadronic system X (which may contain jets) and an imbalance in transverse momentum (from the neutrino), as outlined in section 3.4.3. This chapter describes the identification of these constituent parts and introduces the kinematic variables employed to perform event selections. The relevant distributions of these quantities are also examined in the region of phase space used in this analysis.

Isolated Leptons with missing P_T and W production at HERA have been previously reported in several H1 publications [1–4]. This analysis uses the full HERA I e^+p data sample, corresponding to an integrated luminosity of 104.7 pb^{-1}. The data were recorded in two distinct running periods, 37.0 pb^{-1} from 1994-1997 ($\sqrt{s} = 301$ GeV) and 67.7 pb^{-1} from 1999-2000 ($\sqrt{s} = 319$ GeV).

6.1 Lepton Identification

The identification of leptons is performed as described below. Different detector components are employed for electrons and muons, reflecting the different nature of their respective interactions within the H1 detector.

6.1.1 Electron Candidates

Electrons are identified as compact, isolated energy clusters in the electromagnetic part of the LAr Calorimeter[1]. The electron finding routine `QESCAT` [105] is employed to perform this task. Inefficient regions of the LAr exist between calorimeter modules where an electron may pass through the EMC and into the HAC without interaction. Therefore a series of fiducial cuts are applied to exclude these regions, namely the z crack between CB2 and CB3 and $\pm 2^\circ$ of each ϕ crack (see figure 2.6). Outside these regions `QESCAT` is over 99% efficient [41]. The electron energy and polar angle, θ_e, are determined from the LAr cluster. In the final selection, electron candidates are required to have "clean" energy deposits. This is done by limiting the energy in a cone of radius 1 in pseudorapidity[2]-azimuth (η-ϕ) space around the electron to be at most 3% of the electron energy.

Electron candidates are also required to have an associated "good" track, with a distance of closest approach (DCA) of less than 12cm. The azimuthal angle, ϕ_e, is determined from the track. Further requirements on the electron track are made in the central region: the transverse momentum (P_T) of the track must be greater than 1 GeV and the radial starting position of the track must be well within CJC1. In the forward region, the electron may shower in the endplate of the CJC (see figure 2.3) resulting in an incorrect track assignment. Therefore, a CJC1 track with P_T

[1] The SpaCal is not used in analysis due to the large DIS/photoproduction background; see section 6.3.

[2] Pseudorapidity, $\eta = -\ln(\tan(\theta/2))$

greater than 1 GeV is also required to match the candidate electron track within cone of radius 1 in η-ϕ space.

The electron energy calibration is performed as described in [43, 106] and is only briefly outlined here. The procedure uses NC DIS events reconstructed using the *double-angle* (DA) method [107], which uses only the electron (θ_e) and hadronic (γ_h) polar angles to define the kinematics. The ratio $E_e^{'}$ / E_{DA} is then constrained to 1, where $E_e^{'}$ is the energy of the scattered electron and E_{DA} is the energy reconstructed from the DA method. The constants used to perform the calibration form a grid in z and ϕ. The inefficient regions described above are once again excluded. At high Q^2 ($\theta_e < 40°$) the ω method [108] is employed. Imperfect γ_h reconstruction and initial state QED radiation are taken into account, and the calibration is cross-checked using QED Compton and e^+e^- lepton pair events (see section 3.6.4).

6.1.2 Muon Candidates

Muon candidates are identified using a wide range of detector components. A combination of these components is used in order to obtain clean muon signatures.

Central muons are restricted to the region $25^o < \theta_\mu < 145^o$ and are categorised by a series of *grades* (1-5) relating to the amount of detector information available. Iron-linked muons are graded highest as grade 1 or grade 2 and have an iron track or cluster associated with a central track within a distance of 0.5 in η-ϕ space. The energy and position of the muon is measured by the central track in the CJC. Both categories of iron-linked muons have additional requirements. Grade 1 muons must have an extrapolated DCA of less than 100cm from the interaction vertex and a minimum of 2 hits in the central muon chamber. Grade 2 muons may only have a maximum of 10 GeV in a cone radius 1.0 in η-ϕ space to ensure a clean signature.

Grade 3 and 4 muons have no iron track information and are based purely on central track and calorimetry information. Grade 5 muons have no track information, and are based on clusters of hits in the iron. Grade 1 and 2 central muons are used in this analysis.

Forward muons are detected in the region $\theta_\mu < 17^o$, and are required to have a good quality track fit. This quality of this fit depends on the number of spatial parameters used; this analysis requires at least a good θ and ϕ resolution, and may also include x and y coordinates in the fit.

All muon tracks, similarly to electron candidates, are required to have a P_T greater than 1 GeV. All isolated muons (see section 6.3.7) must have an LAr energy deposit less than 8 GeV in a cone of radius 1.0 in η-ϕ space around the associated track. All identified muons (central or forward) are also required to be isolated from other forward muons in the event. This ensures a clean muon signal in the forward region where scattering in the beam pipe may cause hits in the instrumented iron and/or the FMD.

6.2 The Hadronic System

The hadronic system four-vector X is reconstructed using information from the LAr, the SpaCal, the TC (iron) and information from tracks. The tracking detectors provide a better momentum measurement than the calorimeters at low P_T and this information is utilised by the `FSCOMB` algorithm [109]. `FSCOMB` assigns a cylinder of radius 25 (50) cm in the EMC (HAC) around the impact point of the track. If the measured track P_T is less than 2 GeV, the energy from the track is used in the energy sum and the cylinder energy excluded. This method also importantly includes low P_T tracks without a calorimetric cluster.

Hadronic jets in the event are identified and reconstructed using an inclusive k_T algorithm [110] with $R < 1$ and $E^T_{min} = 5$ GeV. If no jets are found, the four-vector of the hadronic system is taken as the net four-vector of the constituent parts.

All identified leptons are excluded from the hadronic system. Any energy around the lepton in the LAr is also excluded using a cone of radius of 0.5 in η-ϕ space for electrons and radius 1.0 for muons. The cone is larger for muons as they tend to deposit energy in the HAC, whilst electrons are generally stopped by the EMC.

Calibration of the hadronic system is performed based on the method outlined in [106]. The method uses a large NC sample and compares the transverse momentum of the calibrated electron, P_T^e to that of the hadronic system, P_T^X. The P_T balance, P_T^X / P_T^e should be equal to 1 in intrinsically balanced NC events and the data are adjusted iteratively until they are in agreement with the MC simulation. A further P_T^X based correction is then applied to ensure the linearity of the calibration across the whole sample. The calibration constants are derived as a function of γ_h for all 7 (8) electromagnetic (hadronic) wheels in the LAr, in a similar fashion to the electron calibration described in section 6.1.1.

6.3 Kinematic Variables

Several further kinematic variables are used in this analysis to reduce the contribution from unwanted background processes. Some are sensitive to the presence of undetected particles in the event, providing a method of selecting the neutrino produced in the W decay. The main characteristics of each variable are described below, including any discriminatory properties. The distribution of each variable is also displayed for a basic phase space selection, as defined in table 6.1, which requires a high P_T lepton and missing transverse momentum measured in the calorimeter (see section 6.3.1). The lepton is also required to be in the forward or central region of the detector, due to the large photoproduction background (electron signal) and poor muon reconstruction in the backward region (muon signal). All further event selections contain these cuts, which yield 1661 electron data events and 207 muon data events.

Variable	Cut
P_T^l	> 10 GeV
θ_l	$5° < \theta_l < 140°$
P_T^{calo}	> 12 GeV

Table 6.1: The basic phase space selection.

6.3.1 P_T^{calo}

P_T^{calo} is defined as the P_T measured by all calorimeters (electromagnetic and hadronic) and is reconstructed from all clusters recorded by the LAr, the SpaCal and the TC using the `FSCLUS` algorithm (see, for example, [111]). All electrons and their respective cones are also included. However, unlike `FSCOMB`, track information is not included, so isolated muons contribute little to this quantity. This means that (especially at low P_T^X), P_T^{calo} may not necessarily indicate an overall momentum imbalance, as explained in section 5.1, and in events containing isolated muons $P_T^{calo} \approx P_T^X$. This quantity is hence used primarily as a method of removing NC background in the search for signal events containing isolated electrons. The distributions of P_T^{calo} in the electron and muon phase space selections are displayed in figure 6.1.

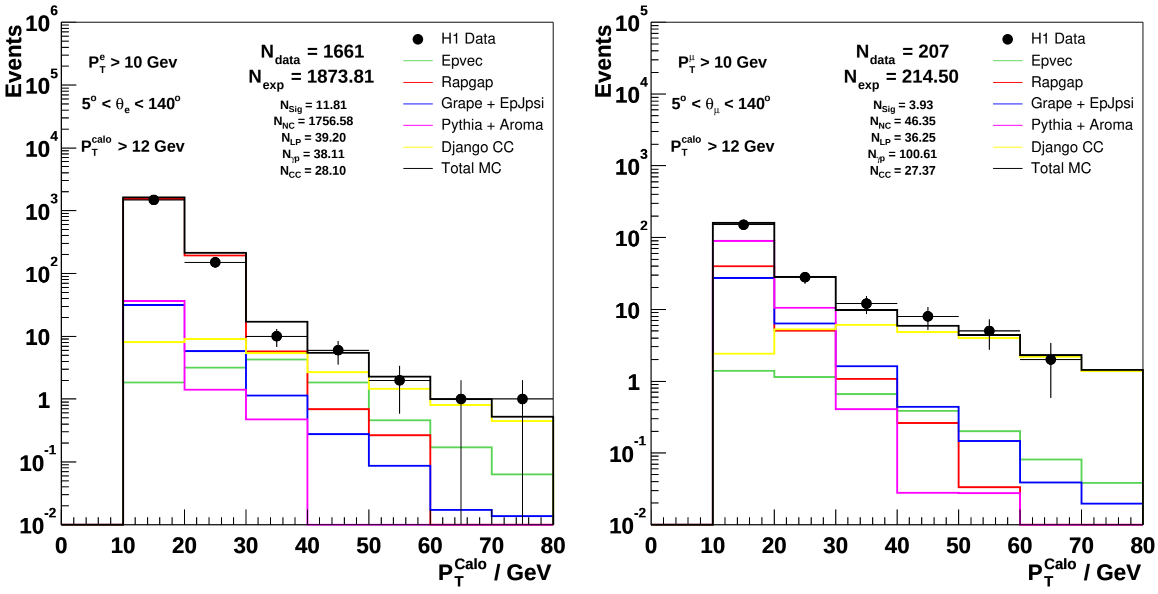

Figure 6.1: The P_T^{calo} distribution for electron (left) and muon (right) events in the basic phase space selection. The full SM prediction is shown, as well as the individual components from Epvec (signal), Rapgap (NC), Grape + EpJpsi (LP), Pythia + Aroma (γp) and Django CC.

6.3.2 P_T^{miss}

The total missing transverse momentum, P_T^{miss}, is calculated using the vector sum of all identified particles. The negative 4-vector of this sum may be attributed to the neutrino in the event and hence allows selection of events containing such a particle in the final state. Note that $P_T^{miss} \approx P_T^{calo}$ unless the event contains isolated muons. The distributions of P_T^{miss} in the electron and muon phase space selections are displayed in figure 6.2.

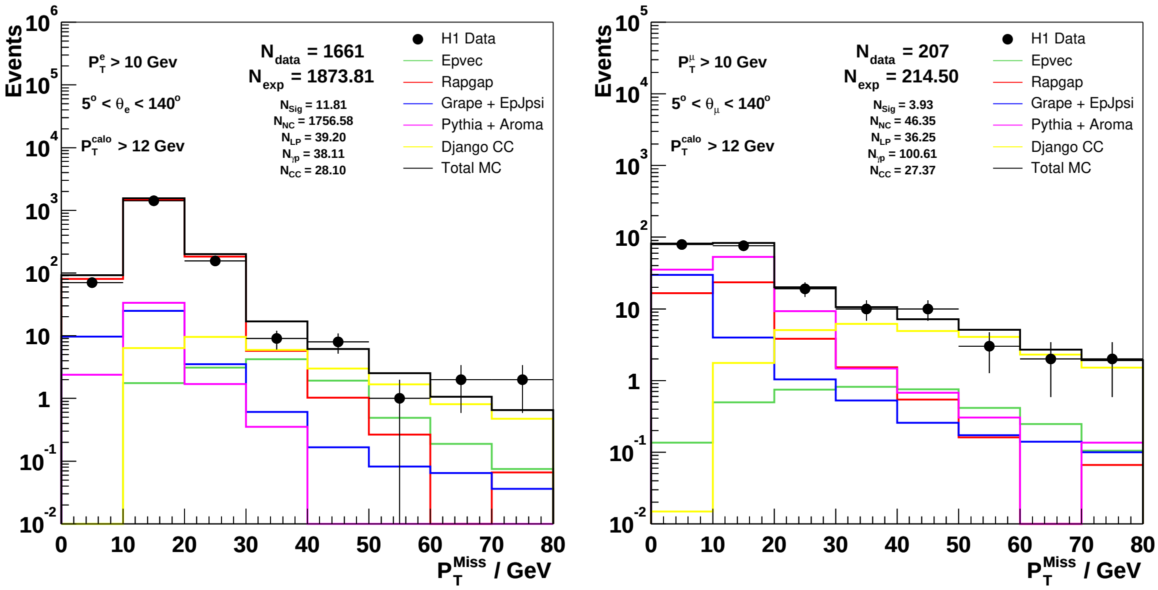

Figure 6.2: The P_T^{miss} distribution for electron (left) and muon (right) events in the basic phase space selection. The full SM prediction is shown, as well as the individual components from Epvec (signal), Rapgap (NC), Grape + EpJpsi (LP), Pythia + Aroma (γp) and Django CC.

6.3.3 ζ^2

As shown in figure 3.4 the NC cross section has a strong Q^2 dependence, which is peaked at low values. Q^2 is reconstructed using the *electron* method [107] given by

$$Q^2 = 4E_e E_l \cos^2(\theta_l/2) \tag{6.1}$$

where E_e is the energy of the beam electron and E_l (θ_l) is the energy (polar angle) of the scattered lepton. In $W \to e\nu$ events, where the scattered electron is often not detected, the W decay electron may be (falsely) tagged as the scattered electron of a NC event. However, the same NC Q^2 dependence is not present in the W cross section so that this variable can be used to reject unwanted background.

Hence the quantity ζ^2 is defined analogously to Q^2 with the understanding that they are actually different quantities depending on the event type. The distributions of ζ^2 in the electron and muon phase space selections are displayed in figure 6.3.

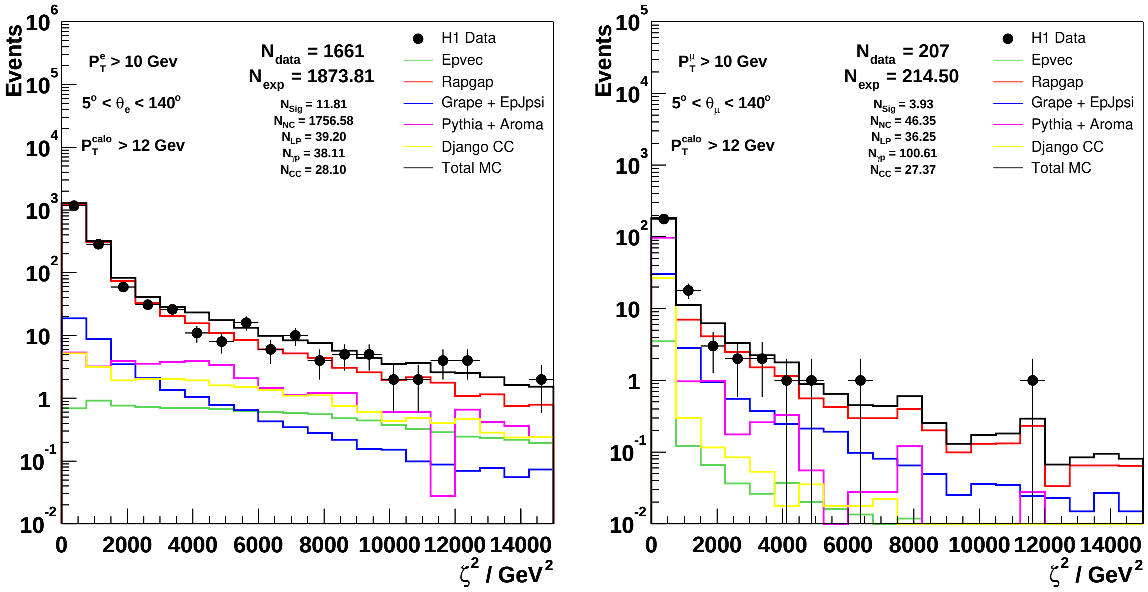

Figure 6.3: The ζ^2 distribution for electron (left) and muon (right) events in the basic phase space selection. The full SM prediction is shown, as well as the individual components from Epvec (signal), Rapgap (NC), Grape + EpJpsi (LP), Pythia + Aroma (γp) and Django CC.

6.3.4 $\Delta\phi_{l-X}$

Acoplanarity, $\Delta\phi_{l-X}$, is a measure of the azimuthal balance of an event, as illustrated in figure 6.4. In NC, photoproduction and LPAIR events this variable is approximately equal to 180°, as they contain no intrinsic missing P_T. This is illustrated for a typical NC event in the azimuthal projection in figure 3.15, where the hadronic system and the electron are produced in a back-to-back configuration. Deviations from this topology in such events may only be caused by detector resolution effects

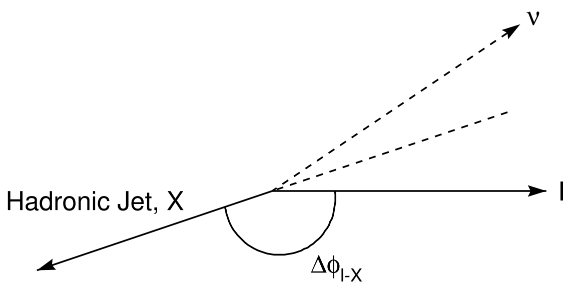

Figure 6.4: Diagram showing the definition of the acoplanarity. The vectors shown are in the azimuthal plane.

or measurement errors. This may be contrasted to the equivalent projection for a typical W event shown in figure 3.10(b), where the hadronic system is not back-to-back with the lepton, and there is missing transverse momentum due to the presence of the neutrino. The hadronic azimuthal angle used in the calculation of $\Delta\phi_{l-X}$ is taken from the full hadronic system, except if P_T^X is less than 5 GeV, when the plug energy deposit is used. The distributions of $\Delta\phi_{l-X}$ in the electron and muon phase space selections are displayed in figure 6.5.

6.3.5 $\frac{V_{ap}}{V_p}$

The ratio $\frac{V_{ap}}{V_p}$ gives another measure of the azimuthal balance of the event, where

$$V_{ap} = -\sum_i \frac{\vec{P}_T^X \cdot \vec{P}_{T,i}}{P_T^X} \quad \text{for} \quad \vec{P}_T^X \cdot \vec{P}_{T,i} < 0 \tag{6.2}$$

$$V_p = \sum_i \frac{\vec{P}_T^X \cdot \vec{P}_{T,i}}{P_T^X} \quad \text{for} \quad \vec{P}_T^X \cdot \vec{P}_{T,i} > 0 \tag{6.3}$$

The quantities V_{ap} and V_p are respectively the sum of the measured calorimetric transverse momentum anti-parallel and parallel to the hadronic system vector P_T^X,

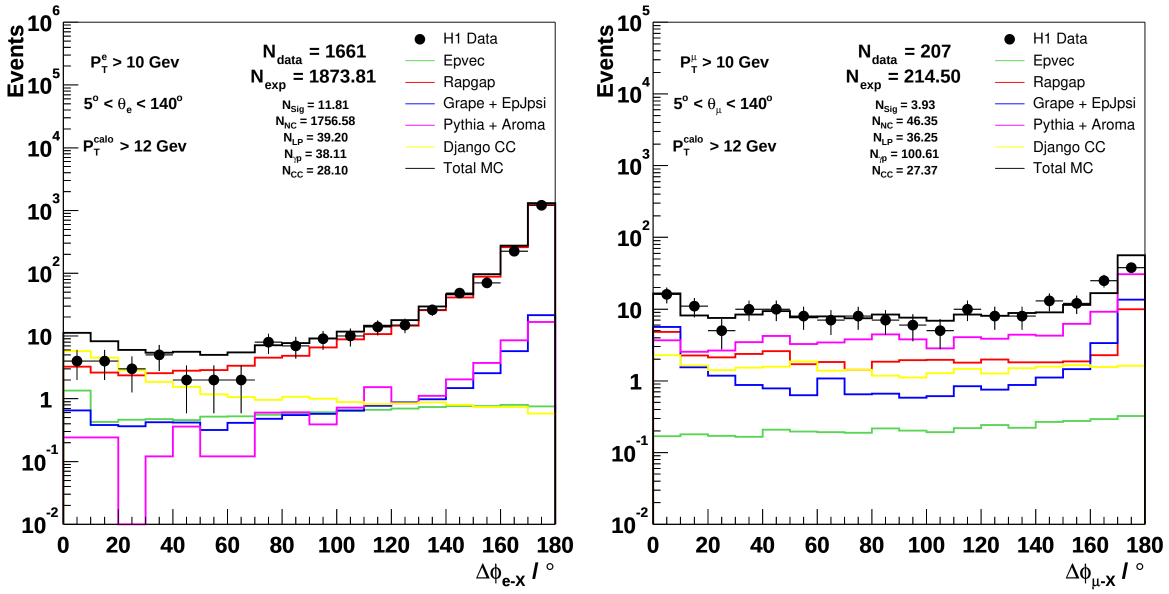

Figure 6.5: The $\Delta\phi_{l-X}$ distribution for electron (left) and muon (right) events in the basic phase space selection. The full SM prediction is shown, as well as the individual components from Epvec (signal), Rapgap (NC), Grape + EpJpsi (LP), Pythia + Aroma (γp) and Django CC.

where the sums are performed over each particle i of the final state [106]. Events containing undetected, high P_T particles generally have low values of $\frac{V_{ap}}{V_p}$. The distributions of $\frac{V_{ap}}{V_p}$ in the electron and muon phase space selections are displayed in figure 6.6.

6.3.6 δ_{miss}

δ_{miss} provides a measure of the longitudinal balance of an event and is defined as

$$\delta_{miss} = 2E_e - \sum_i (E_i - p_{z,i}) \tag{6.4}$$

where E_e is the energy of the beam electron and E_i ($p_{z,i}$) is the energy (longitu-

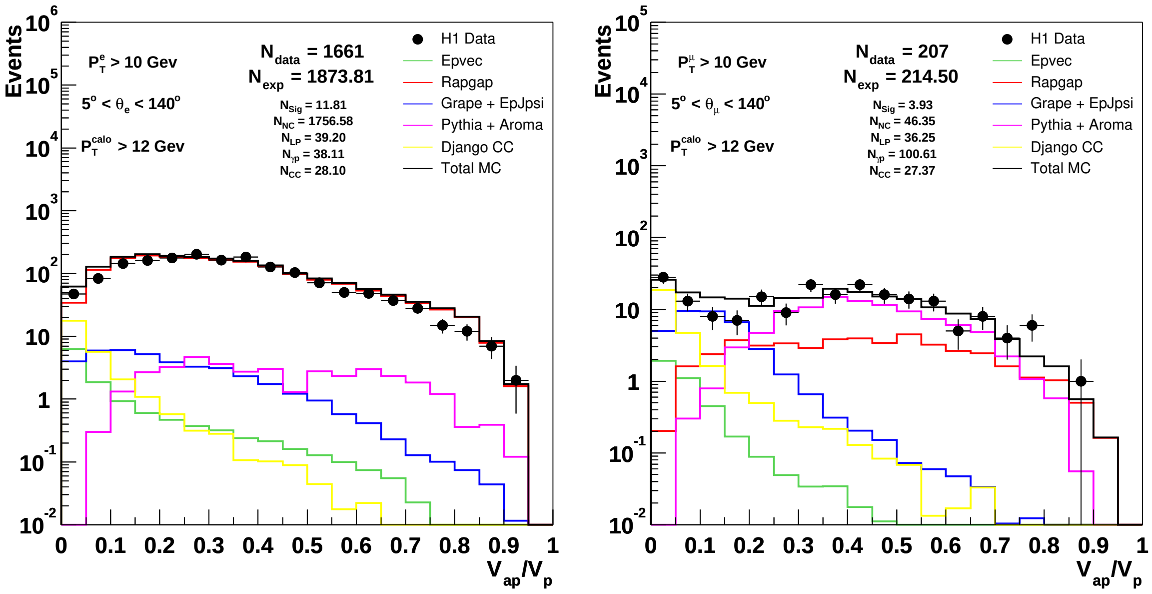

Figure 6.6: The $\frac{V_{ap}}{V_p}$ distribution for electron (left) and muon (right) events in the basic phase space selection. The full SM prediction is shown, as well as the individual components from Epvec (signal), Rapgap (NC), Grape + EpJpsi (LP), Pythia + Aroma (γp) and Django CC.

dinal momentum) of each detected particle in the event. For an event where only longitudinal momentum in the very forward region remains undetected, $\delta_{miss} \approx 0$ GeV. Background processes that are intrinsically longitudinally balanced can therefore be differentiated from signal events as δ_{miss} is sensitive to undetected particles. The distributions of δ_{miss} in the electron and muon phase space selections are displayed in figure 6.7.

6.3.7 Isolation Criteria: D_{jet} and D_{track}

An important part of the topology in a typical signal event is the isolation of the identified lepton with respect to other parts of the final state. This is quantified using the following two variables. The distance D_{jet} from the lepton track to the

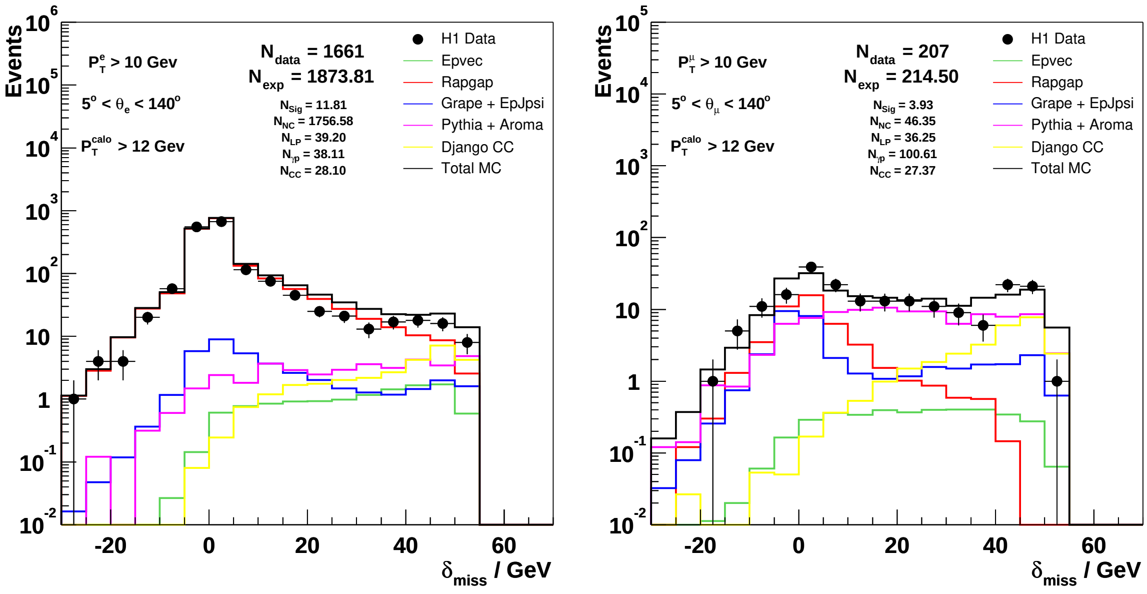

Figure 6.7: The δ_{miss} distribution for electron (left) and muon (right) events in the basic phase space selection. The full SM prediction is shown, as well as the individual components from Epvec (signal), Rapgap (NC), Grape + EpJpsi (LP), Pythia + Aroma (γp) and Django CC.

axis of the closest hadronic jet in η-ϕ space is defined as

$$D_{jet} = \sqrt{(\Delta\eta_{track-jet})^2 + (\Delta\phi_{track-jet})^2} \tag{6.5}$$

where if no jets are present the full hadronic system is used as described above. The distributions of D_{jet} in the electron and muon phase space selections are displayed in figure 6.8.

A similar treatment is performed with respect to the nearest good track to the lepton to calculate the distance D_{track}. This quantity not only ensures the isolation of the lepton from separated parts of the hadronic system but also any other leptons in the event. The distributions of D_{track} in the electron and muon phase space

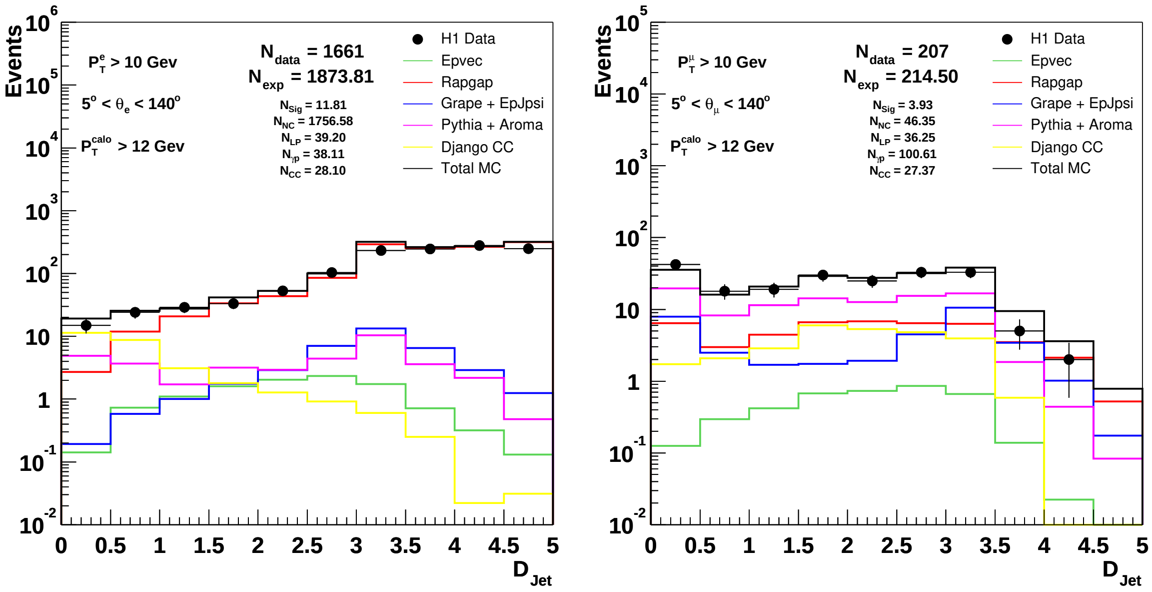

Figure 6.8: The D_{jet} distribution for electron (left) and muon (right) events in the basic phase space selection. The full SM prediction is shown, as well as the individual components from Epvec (signal), Rapgap (NC), Grape + EpJpsi (LP), Pythia + Aroma (γp) and Django CC.

selections are displayed in figure 6.9.

An identified lepton is hence termed "isolated" if it is well separated from jets and other tracks in the event, typically by selecting $D_{jet} > 1.0$ and $D_{track} > 0.5$. A further fiducial cut is placed on isolated tracks not associated to an identified particle in the central region. Events containing such a track within $\pm\, 2^{\circ}$ of a phi crack are excluded to ensure a clean reconstruction of the full final state.

6.3.8 P_T^X

The transverse momentum of the hadronic final state, P_T^X, is an important quantity in the final selections employed in this analysis. The distributions of P_T^X in the

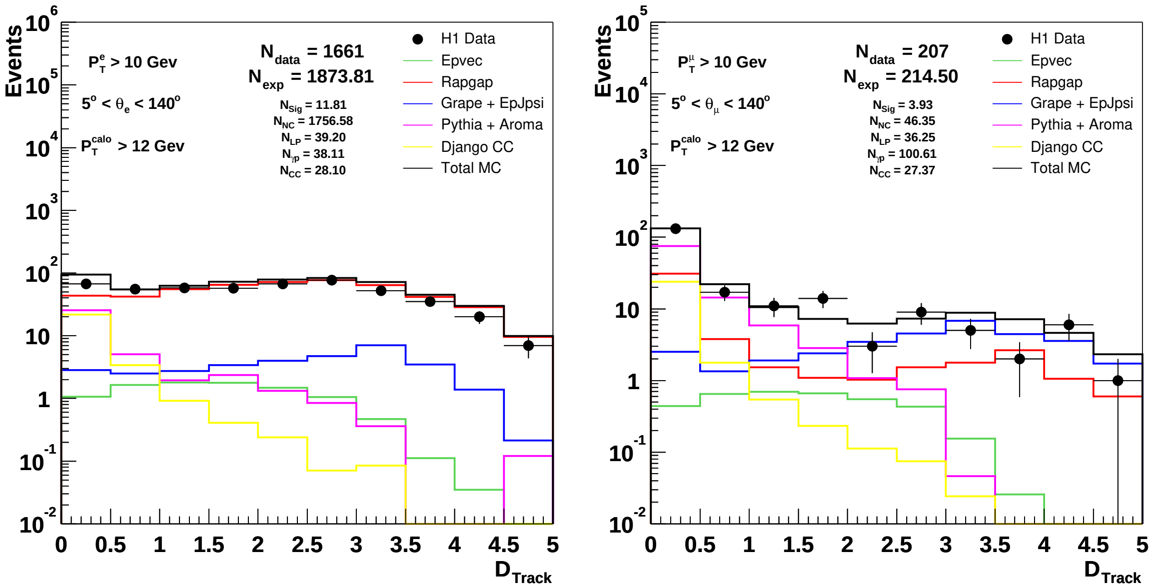

Figure 6.9: The D_{track} distribution for electron (left) and muon (right) events in the basic phase space selection. The full SM prediction is shown, as well as the individual components from Epvec (signal), Rapgap (NC), Grape + EpJpsi (LP), Pythia + Aroma (γp) and Django CC.

electron and muon phase space selections are displayed in figure 6.10. In events containing isolated muons, where $P_T^X \approx P_T^{calo}$, the effect of the phase space cut on P_T^{calo} is visible at low P_T^X.

6.3.9 Reconstructed Masses

Final state invariant masses may be reconstructed using P_T balance and $E - p_z$ conservation to calculate the missing four-vector. If the scattered electron is detected in the event ($\theta_{scat} \lesssim 176.5°$) the event kinematics may be fully reconstructed, assuming only one neutrino in the final state and no initial state radiation off the incoming electron. The invariant mass of the lepton-neutrino system, $M^{l\nu}$, may be calculated as

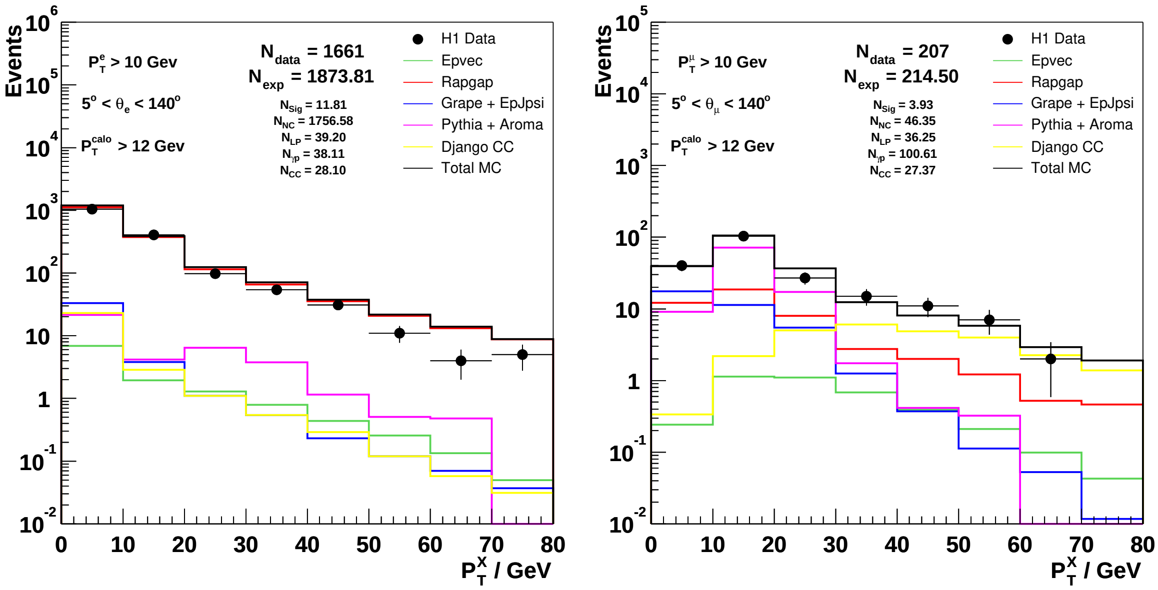

Figure 6.10: The P_T^X distribution for electron (left) and muon (right) events in the basic phase space selection. The full SM prediction is shown, as well as the individual components from Epvec (signal), Rapgap (NC), Grape + EpJpsi (LP), Pythia + Aroma (γp) and Django CC.

$$M^{l\nu} = \sqrt{(E^{\nu} + E^{l})^2 - (p^{\nu} + p^{l})^2} \tag{6.6}$$

The 3-body invariant mass, $M^{l\nu X}$ is also calculable (similarly to equation 6.6) with the additional inclusion of the hadronic system X.

If the scattered electron escapes detection in the beam-pipe, it may possess a fraction of the total event $E - p_z$ but is known to carry a negligible quantity of transverse momentum. The P_T constraint is used to calculate the transverse mass of the lepton-neutrino system $M_T^{l\nu}$, which is given by

$$M_T^{l\nu} = \sqrt{(P_T^{miss} + P_T^{l})^2 - (P_T^{miss+l})^2} \tag{6.7}$$

as defined in [112].

Under the assumption that the undetected scattered electron has negligible energy and therefore negligible $E - p_z$, the final state invariant masses may also be calculated using the missing four-vector in the event. The invariant mass of the lepton and missing four-vector system is given by the following equation

$$M^{l\,miss} = \sqrt{(E^{miss} + E^{l})^2 - (p^{miss} + p^{l})^2} \tag{6.8}$$

The uncertainty introduced into this calculation due to the assumption of a negligible scattered electron energy is investigated in section 9.4. Similarly, the 3-body variant mass M^{lmissX} is also calculable with the additional inclusion of the hadronic system X.

6.4 Reweight of Photoproduction Monte Carlos

The dominant contribution to the muon phase space selection comes from photoproduction, which is modelled by PYTHIA and AROMA as detailed in section 3.6.3. The predicted rate from these Monte Carlos is increased by a factor of 2 in order to reproduce the expectation of the data in this sample. This is illustrated in figure 6.11 for three independent selection variables; P_T^{calo} (top), D_{jet} (middle) and $\frac{V_{ap}}{V_p}$ (bottom). The scaling factor was chosen as to match the highest bin in the P_T^{calo} distribution, although all rescaled distributions exhibit better agreement as a result of the reweight. The reweight of photoproduction Monte Carlos is applied to all selections employed in this analysis, including the basic phase space selection described in this chapter.

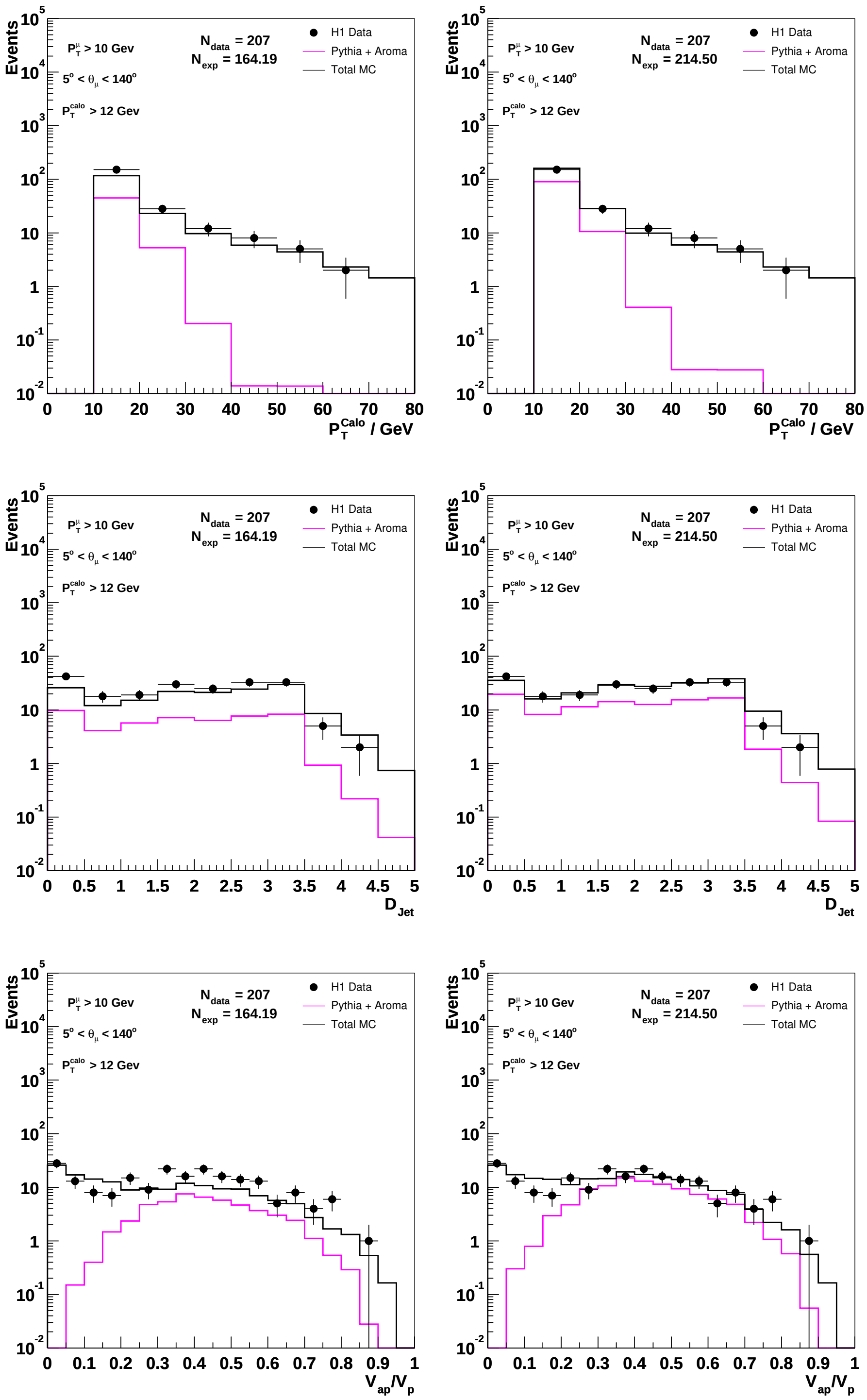

Figure 6.11: Distributions of P_T^{calo} (top), D_{jet} (middle) and $\frac{V_{ap}}{V_p}$ (bottom) in the muon phase space selection before (left) and after (right) MC reweighting.

Chapter 7

Background Studies

To ensure that the dominant background processes in this analysis are understood, a series of "enriched" selections are performed. Each selection is an extension of the basic phase space selection described in chapter 6 and designed specifically to select one background process. Signal processes are described in section 3.4. For signal events containing isolated electrons (*e channel*), the dominant background processes in the final event selection are NC and CC. For signal events containing isolated muons (μ *channel*), the dominant background in the final event selection arises from elastic LP events or CC events containing a reconstructed isolated muon. The final event selection is presented in chapter 8.

The enriched selections are used to verify the agreement between data and simulation of the background processes. This is particularly important in regions where the signal process is not dominant, although it should be noted that none of the enriched selections specifically reject signal events. The level of agreement of these selections determines the systematic uncertainty attributed to the background processes. These uncertainties are discussed at the end of this chapter.

7.1 Electron NC Enriched Selection

The electron phase space selection defined in section 6.3 consists mainly of NC events. However, further cuts may be used to reduce, in particular, the CC component to achieve a NC dominated sample. This is done by applying isolation criteria using D_{jet} and D_{track}, as any misidentified electrons in CC events are usually part of the hadronic jet (see figure 3.16). The distribution of D_{jet} in the electron phase space selection is displayed in figure 6.8. It can be seen that the contributions of other background processes are comparable with the prediction from NC at low values of D_{jet}. This sample requires $D_{jet} > 1.0$, which results in a large reduction in the CC component. Figure 6.9 similarly shows that the contributions from CC and photoproduction are comparable in the electron phase space selection at low D_{track}. A further cut is imposed on this sample of $D_{track} > 0.5$, but only for events with $\theta_e > 45°$, due to the problem of showering electrons in the forward region described in section 6.1.1.

After applying these criteria, this selection mainly contains events with genuine electron candidates and fake missing transverse momentum due to mismeasurement. The distributions of the key kinematic quantities of the electron NC enriched selection are presented in figures 7.1 to 7.6. The data are the points. The combined SM prediction is given by the open histogram and the shaded band represents the total SM error (see section 7.5). The individual components of the SM prediction are displayed numerically. The signal component is given by the full histogram.

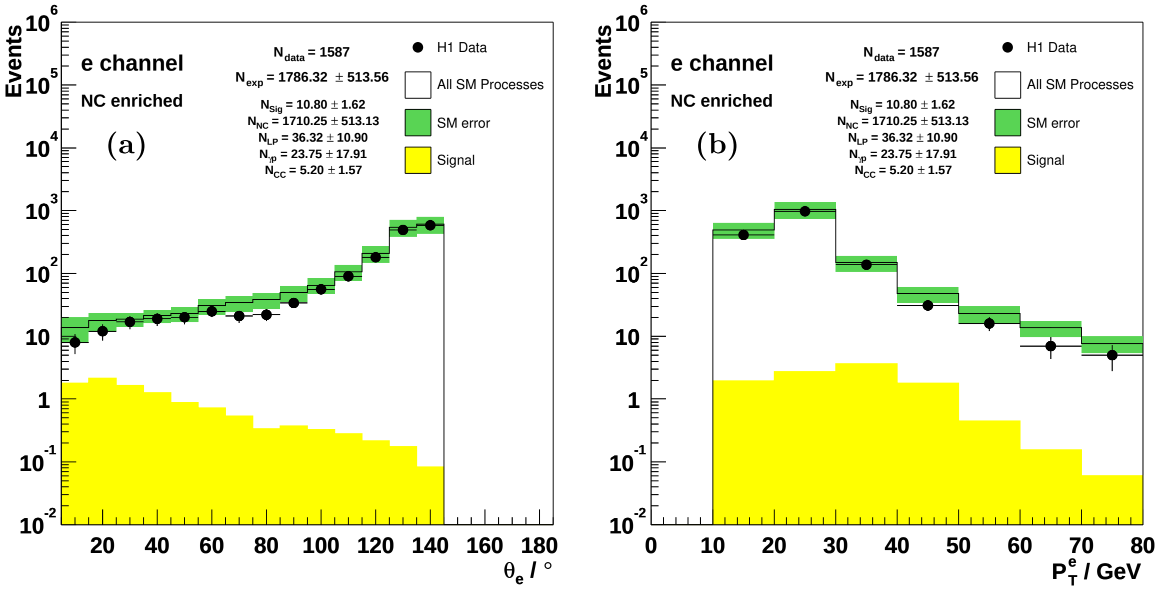

Figure 7.1: The θ_e (a) and P_T^e (b) distributions of the electron NC enriched selection.

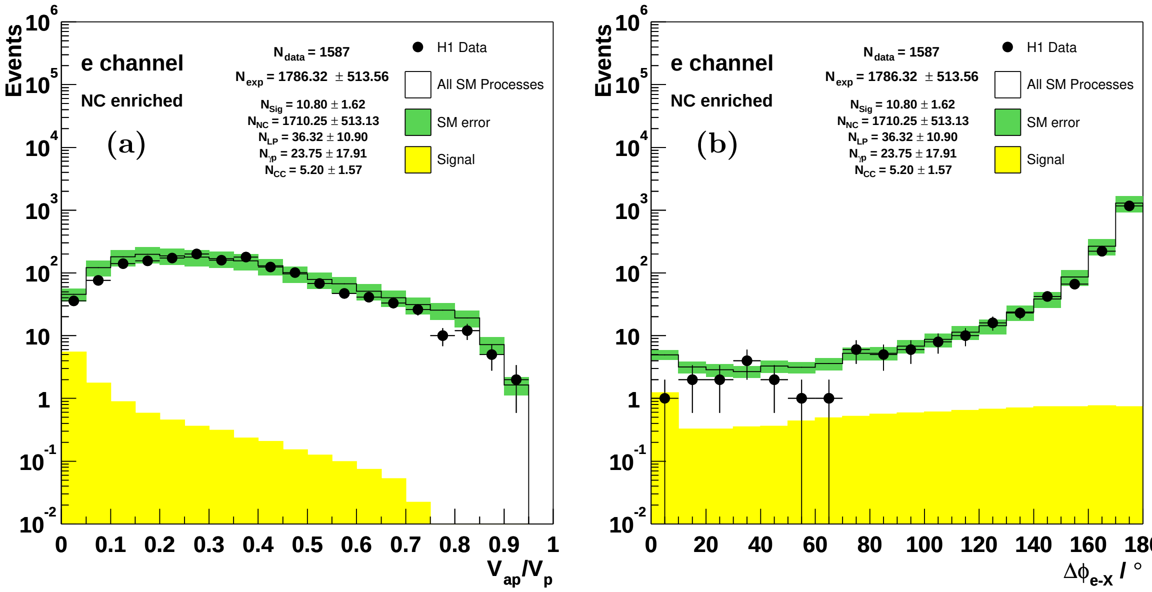

Figure 7.2: The $\frac{V_{ap}}{V_p}$ (a) and $\Delta\phi_{e-X}$ (b) distributions of the electron NC enriched selection.

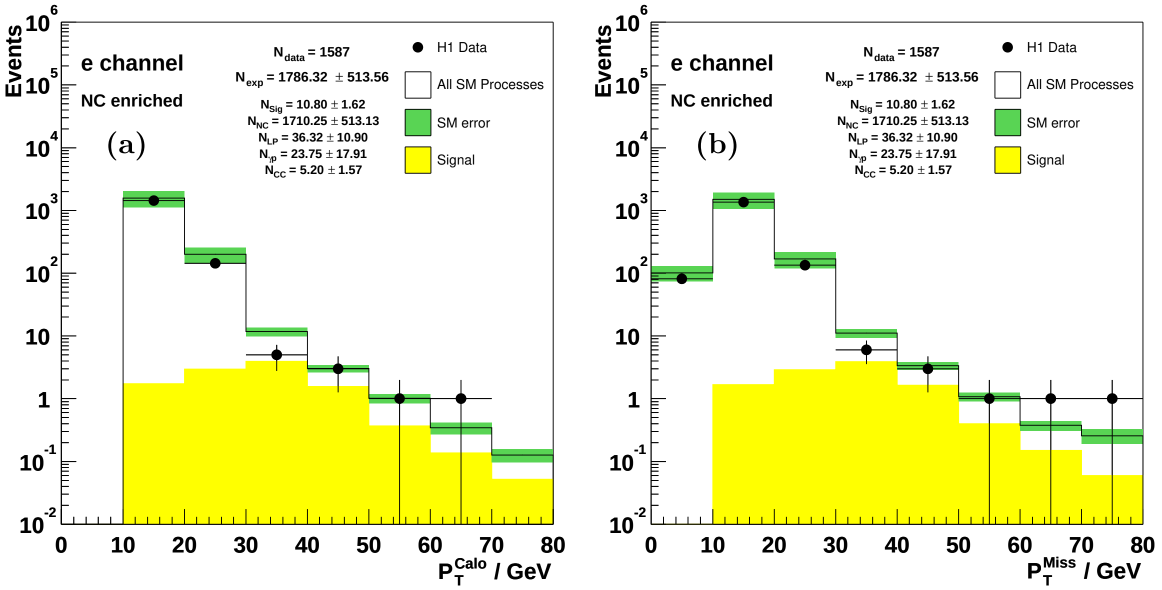

Figure 7.3: The P_T^{calo} (a) and P_T^{miss} (b) distributions of the electron NC enriched selection.

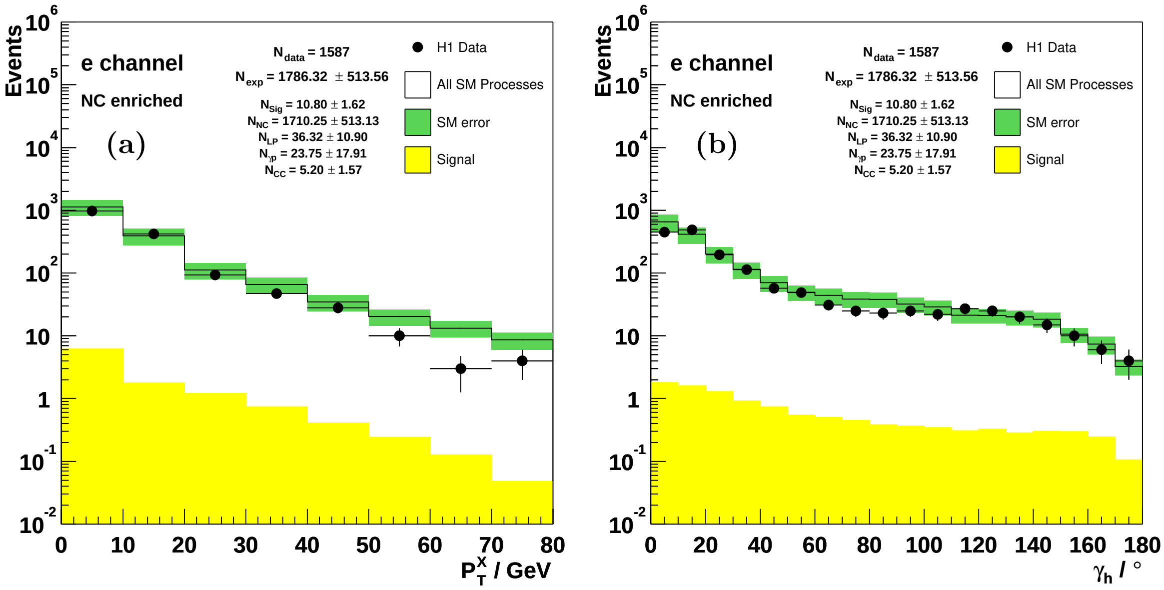

Figure 7.4: The P_T^X (a) and γ_h (b) distributions of the electron NC enriched selection.

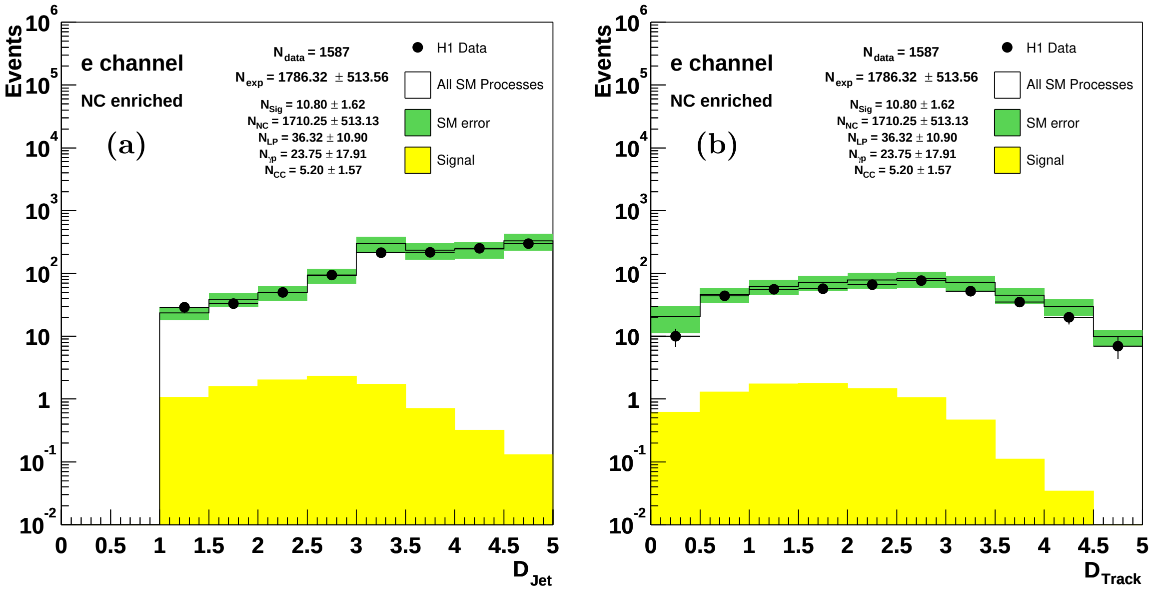

Figure 7.5: The D_{jet} (a) and D_{track} (b) distributions of the electron NC enriched selection.

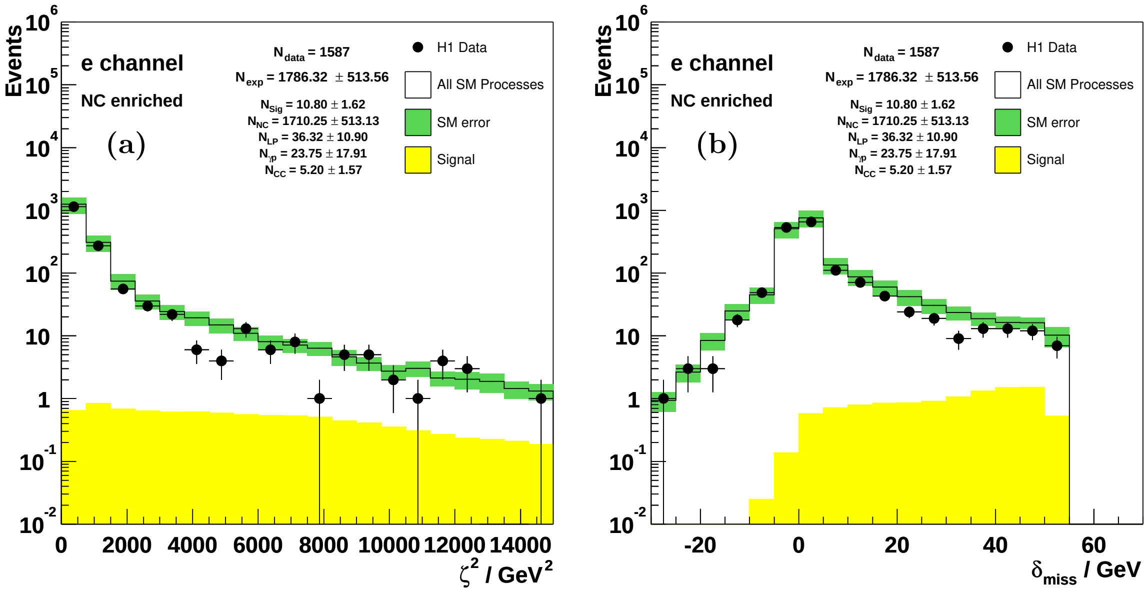

Figure 7.6: The ζ^2 (a) and δ_{miss} (b) distributions of the electron NC enriched selection.

7.2 Electron CC Enriched Selection

To study the CC component of the electron phase space selection, the dominant NC component must be rejected as much as possible. This is done by applying several standard anti-NC cuts. As described in section 6.3.3, ζ^2 is equivalent to Q^2 in NC events. This can be seen in the electron phase space ζ^2 distribution in figure 6.3, where the NC component is strongly peaked at low values. A cut of $\zeta^2 > 2500$ GeV is applied to this selection, which removes the majority of the NC contribution. A further anti-NC cut is performed by requiring $\frac{V_{ap}}{V_p} < 0.15$ [106], which also removes a significant amount of the photoproduction component. CC (and signal) events tend to have low values of $\frac{V_{ap}}{V_p}$, as seen in figure 6.6.

Two further cuts are applied based on the overall balance of the event: $\Delta\phi_{e-X} < 160°$ and $\delta_{miss} > 5$ GeV. NC and LP events tend to have high values of $\Delta\phi_{e-X}$, as they are intrinsically balanced in the azimuthal plane. Figure 6.5 illustrates this strong dependence and also shows that CC events are most densely populated at low values of $\Delta\phi_{e-X}$. If the event contains no undetected particles and is fully contained, $\delta_{miss} \approx 0$ GeV as explained in section 6.3.6. The distribution of δ_{miss} in the electron phase space selection, displayed in figure 6.7, shows that the NC and LP components are peaked at 0 GeV, and fall off steeply above 5 GeV. This may be contrasted with the CC component, which rises towards positive values of δ_{miss}.

After applying these criteria, this selection mainly contains events with misidentified electron candidates and genuine missing transverse momentum. However, as well as the dominant CC component, a significant signal prediction is also present. The distributions of the key kinematic quantities of the electron CC enriched selection are presented in figures 7.7 to 7.12. The data are the points. The combined SM prediction is given by the open histogram and the shaded band represents the total SM error (see section 7.5). The individual components of the SM prediction are displayed numerically. The signal component is given by the full histogram.

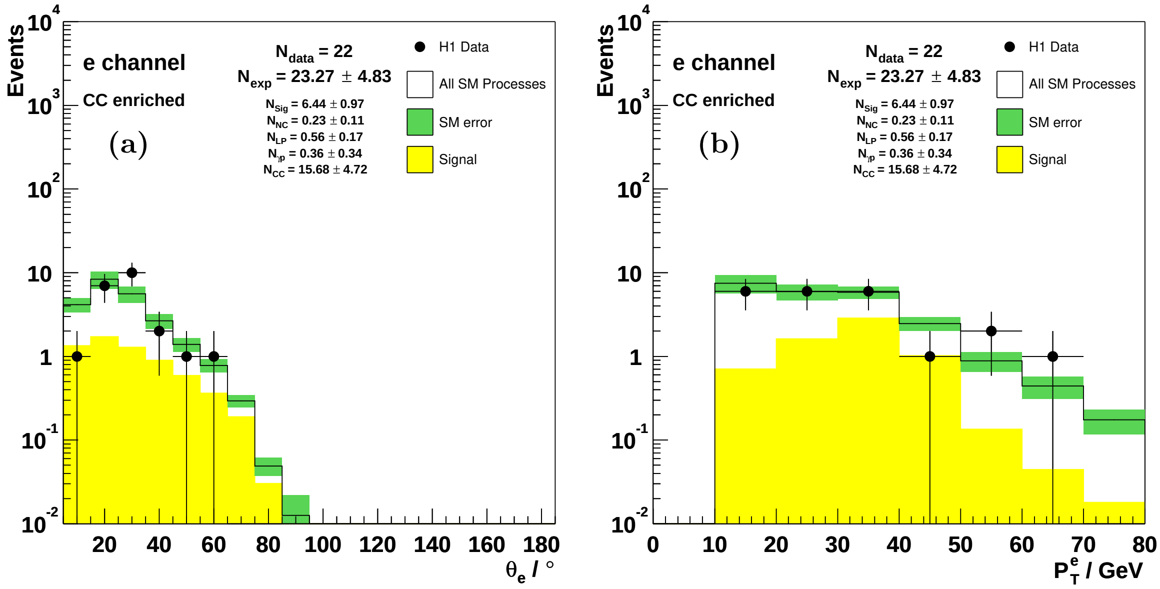

Figure 7.7: The θ_e (a) and P_T^e (b) distributions of the electron CC enriched selection.

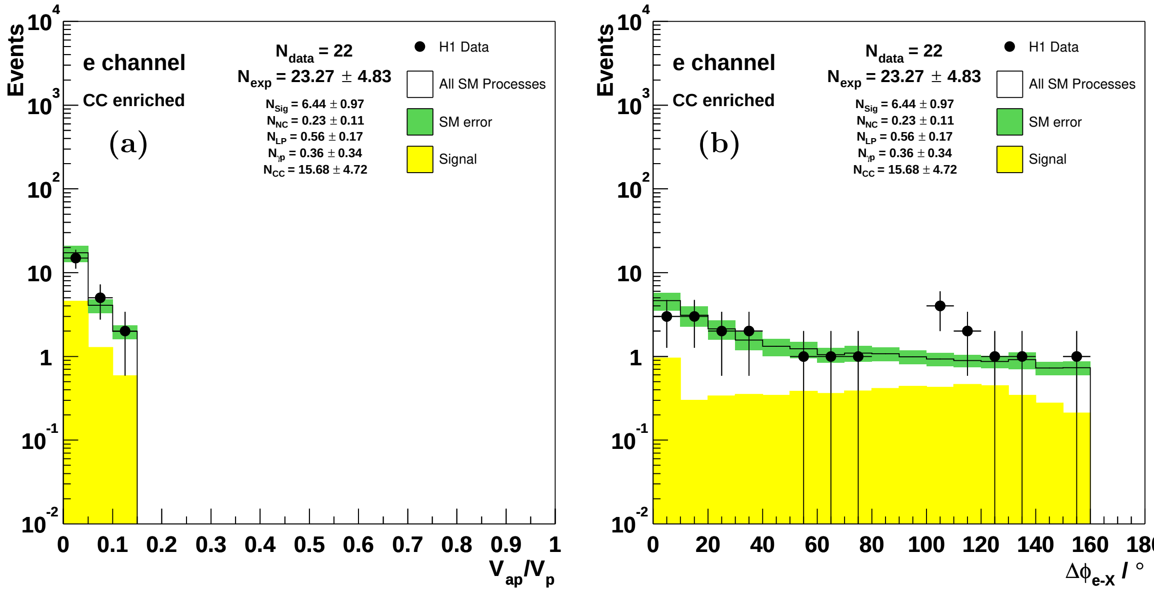

Figure 7.8: The $\frac{V_{ap}}{V_p}$ (a) and $\Delta\phi_{e-X}$ (b) distributions of the electron CC enriched selection.

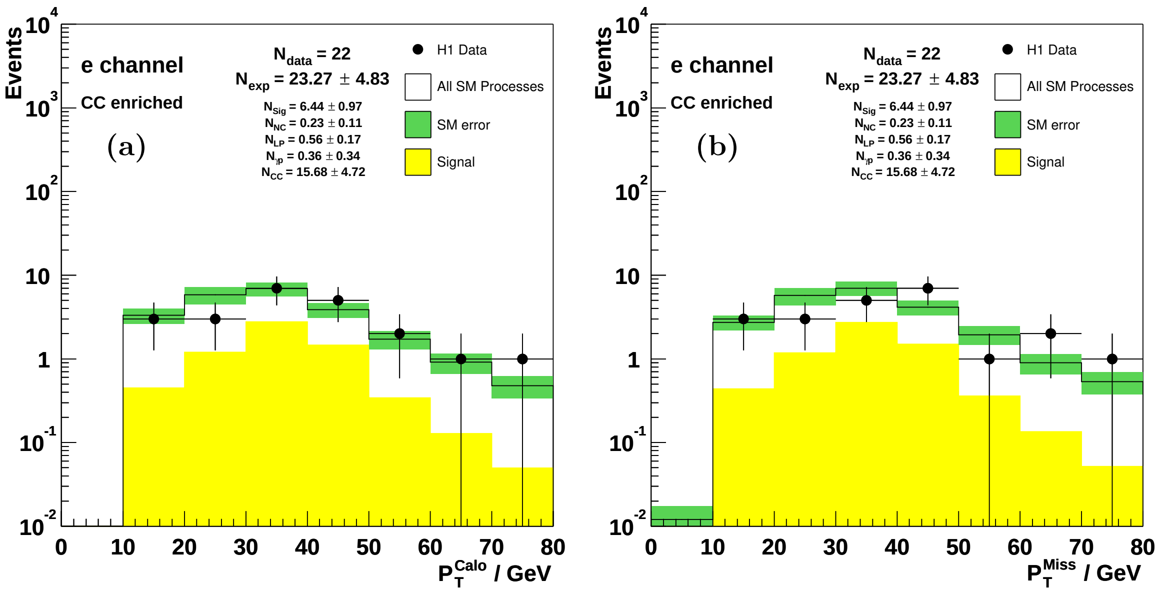

Figure 7.9: The P_T^{calo} (a) and P_T^{miss} (b) distributions of the electron CC enriched selection.

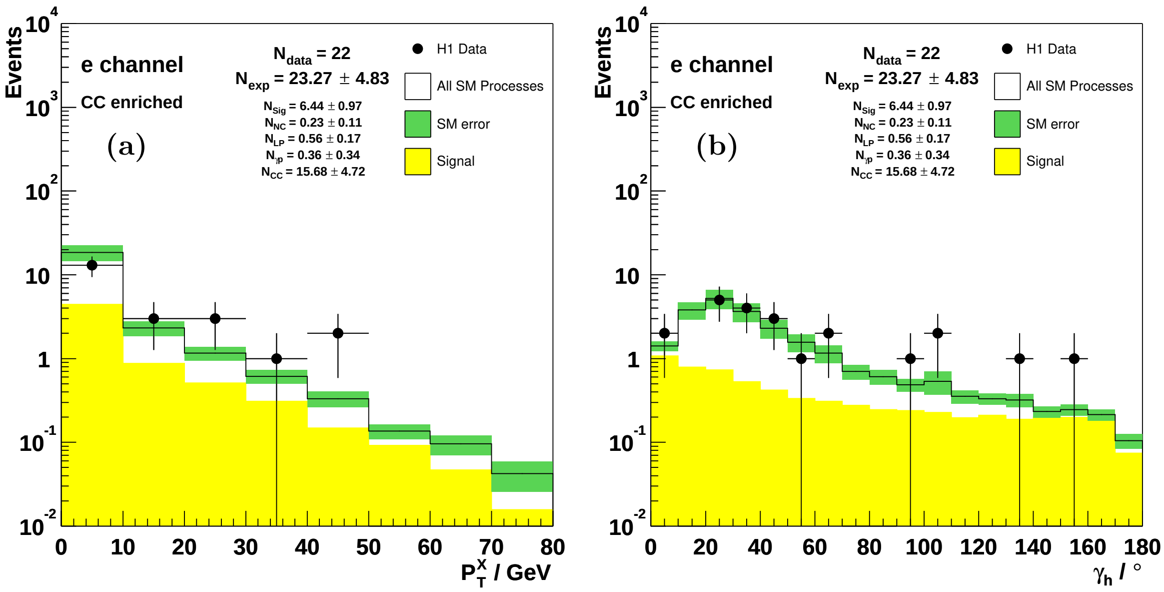

Figure 7.10: The P_T^X (a) and γ_h (b) distributions of the electron CC enriched selection.

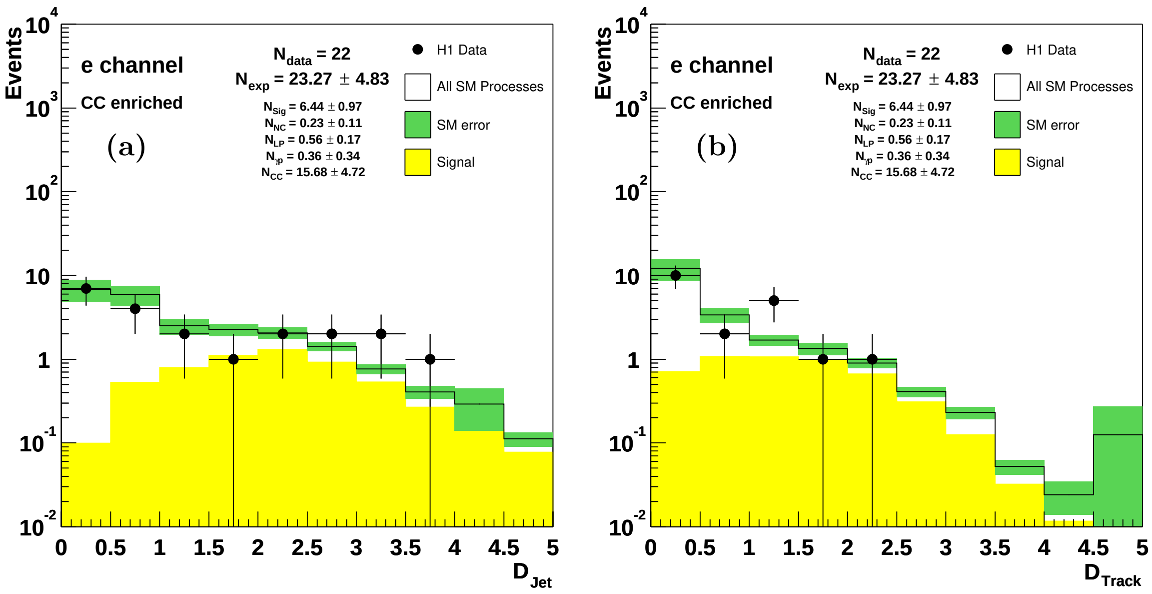

Figure 7.11: The D_{jet} (a) and D_{track} (b) distributions of the electron CC enriched selection.

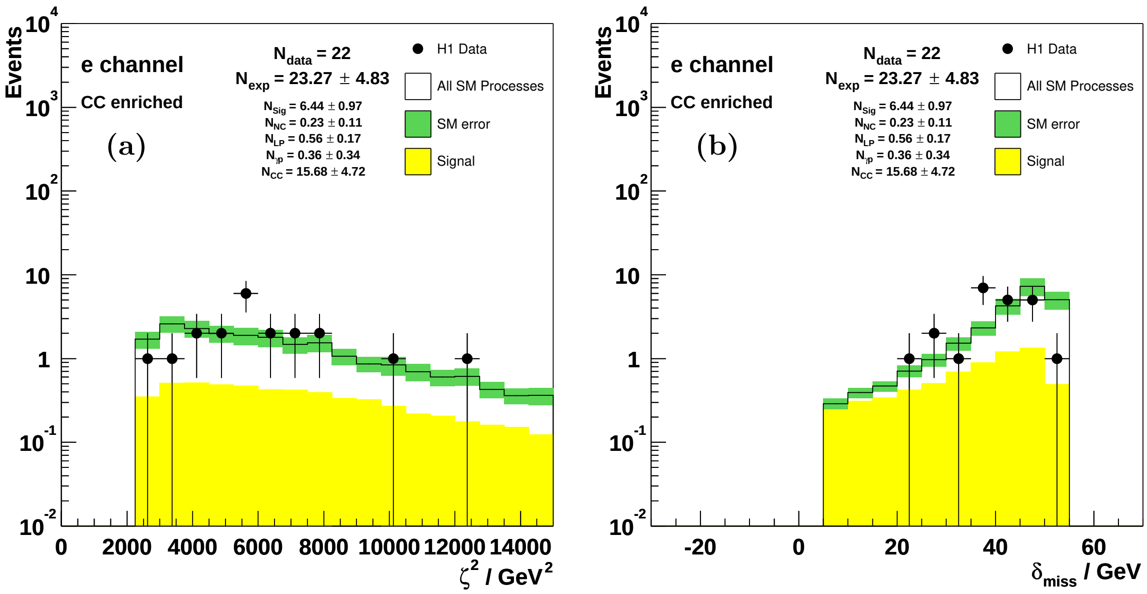

Figure 7.12: The ζ^2 (a) and δ_{miss} (b) distributions of the electron CC enriched selection.

7.3 Muon Lepton Pair Enriched Selection

In order to obtain a lepton pair (LP) sub-sample of the muon phase space selection, the dominant photoproduction component must be suppressed. This is done by requiring $\frac{V_{ap}}{V_p} < 0.2$. Figure 6.6 shows the $\frac{V_{ap}}{V_p}$ distribution in the muon phase space selection, where the photoproduction and NC components are seen to have rather flat distributions, with a photoproduction peak around 0.4. Conversely, the LP component rises towards low values of $\frac{V_{ap}}{V_p}$. Similarly to the electron NC selection, isolation criteria are applied to the identified lepton, namely $D_{jet} > 1.0$ and $D_{track} > 0.5$, so that events in this sample contain at least one isolated muon. The isolation requirement removes the majority of the CC component also present at low $\frac{V_{ap}}{V_p}$.

After applying these criteria, this selection mainly contains events with genuine muons and fake missing transverse momentum due to mismeasurement. As well as the dominant LP contribution, a small NC component is also present containing misidentified muons. In addition, a small but significant signal prediction is present and all muon data events which pass the final event selection (see section 8.2) are also present in this sample. The distributions of the key kinematic quantities of the muon LP enriched selection are presented in figures 7.13 to 7.17. The data are the points. The combined SM prediction is given by the open histogram and the shaded band represents the total SM error (see section 7.5). The individual components of the SM prediction are also displayed numerically. The signal component is given by the full histogram.

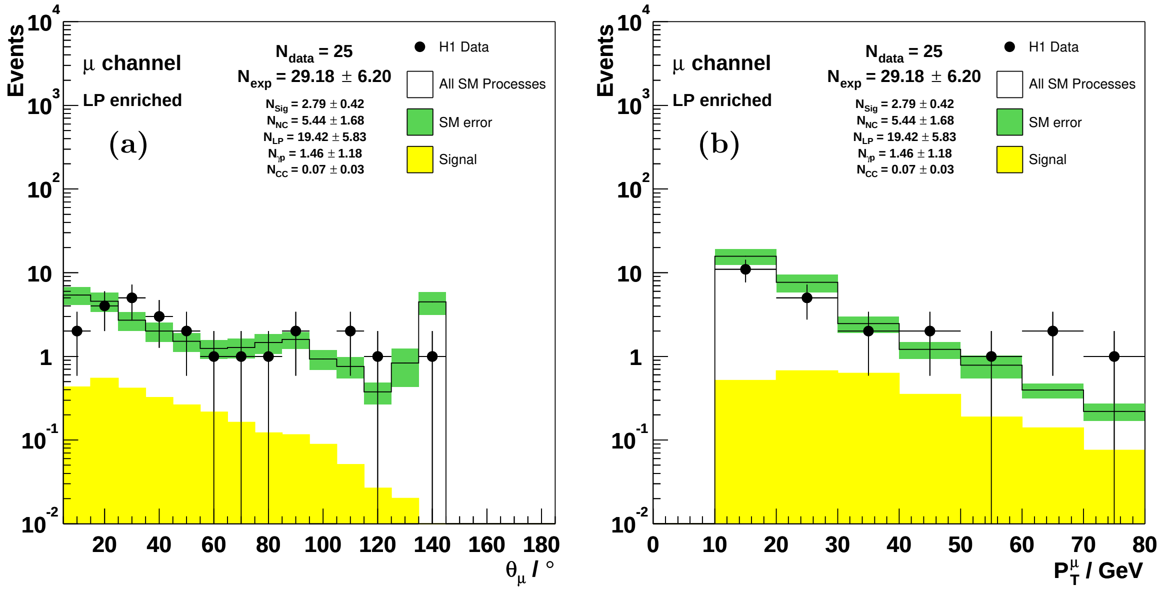

Figure 7.13: The θ_μ (a) and P_T^μ (b) distributions of the muon LP enriched selection.

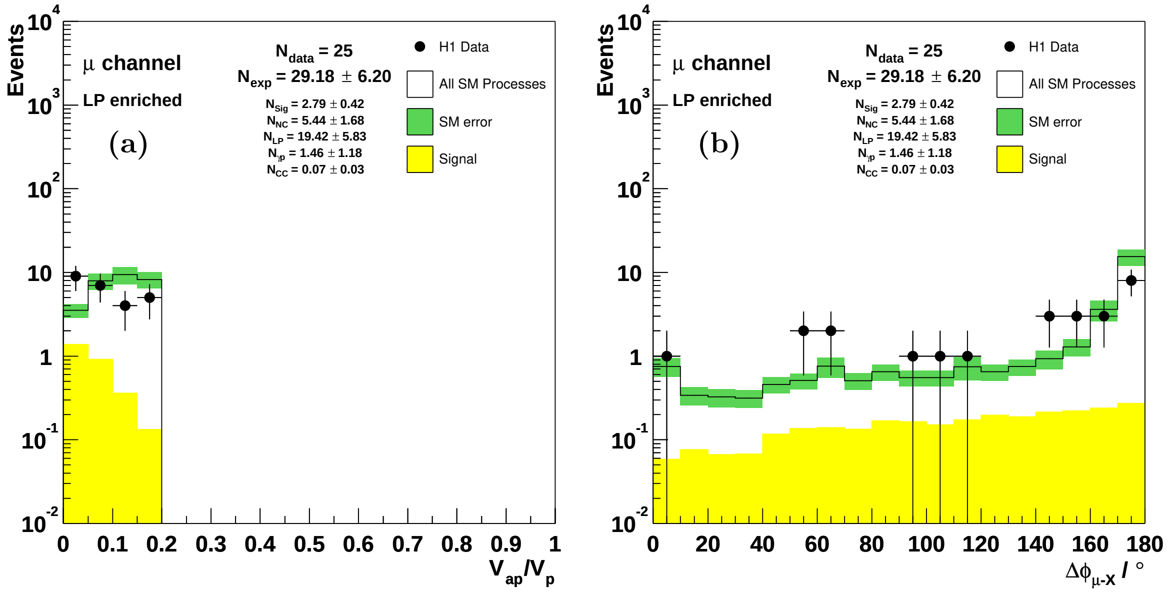

Figure 7.14: The $\frac{V_{ap}}{V_p}$ (a) and $\Delta\phi_{\mu-X}$ (b) distributions of the muon LP enriched selection.

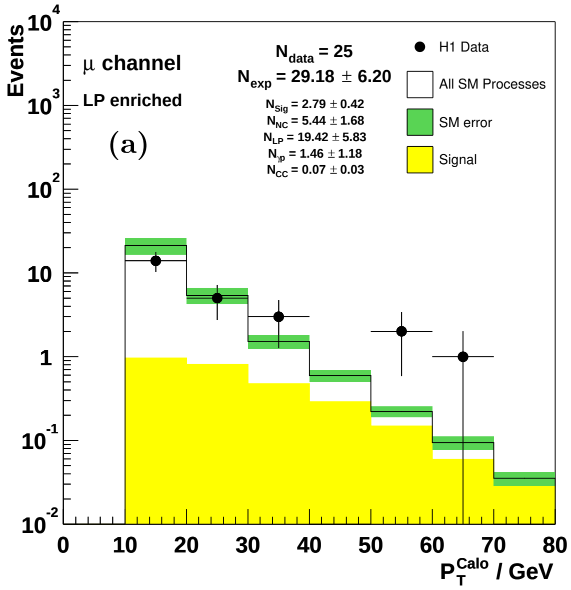

Figure 7.15: The P_T^{calo} (a) and P_T^{miss} (b) distributions of the muon LP enriched selection.

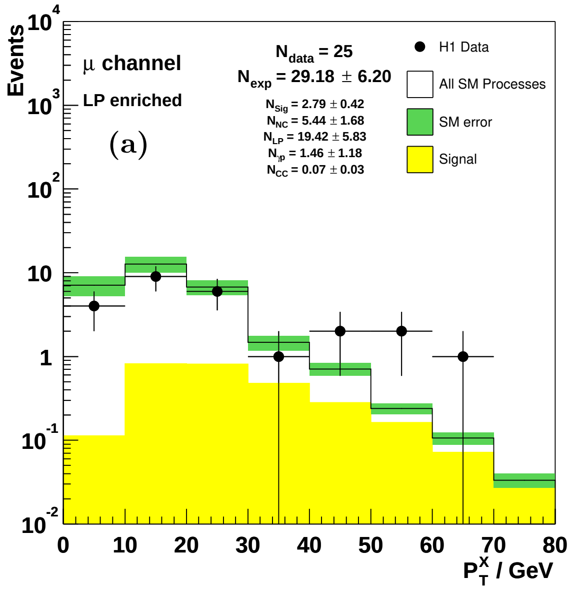

Figure 7.16: The P_T^X (a) and γ_h (b) distributions of the muon LP enriched selection.

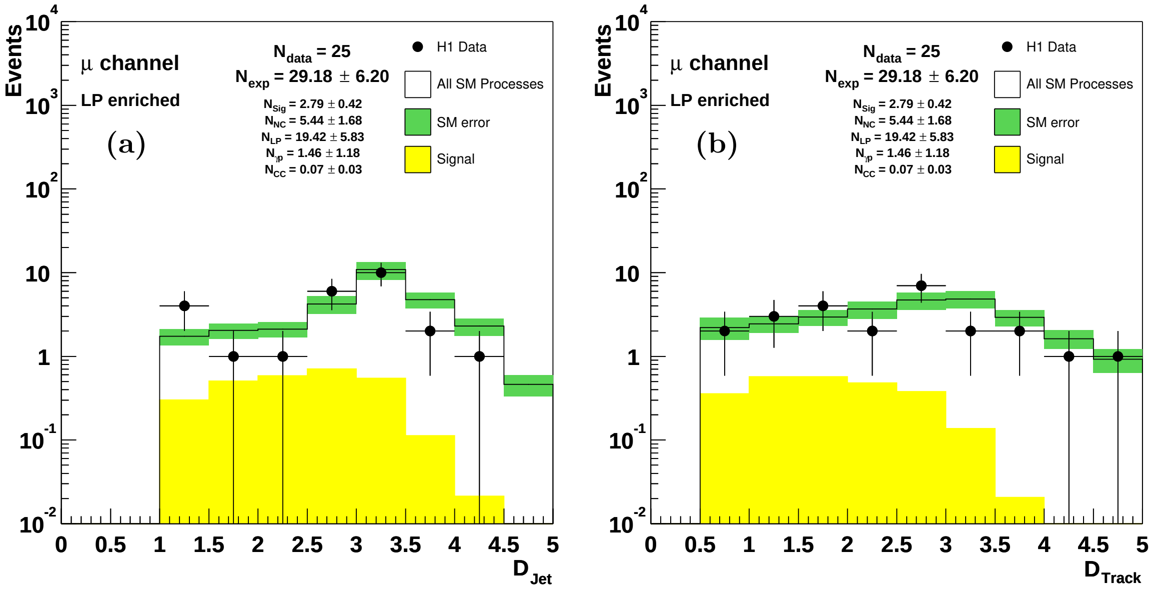

Figure 7.17: The D_{jet} (a) and D_{track} (b) distributions of the muon LP enriched selection.

7.4 Muon CC Enriched Selection

As in the muon LP enriched selection, the main cut employed in this sample selects events at low values of $\frac{V_{ap}}{V_p}$. However, the CC component of the muon phase space sample has a much steeper peak towards lower values of $\frac{V_{ap}}{V_p}$ than the LP component, so this cut is tightened to $\frac{V_{ap}}{V_p} < 0.15$ to remove as much of the LP contribution as possible. Events in this selection must contain at least one muon, but no isolation criteria is applied. Similarly to the electron CC selection, a cut on $\Delta\phi_{\mu-X}$ is also performed. However, as can be seen in figure 6.5, the peak at high values of $\Delta\phi_{l-X}$ is not as significant in the muon phase space selection as in the electron phase space selection, so this sample requires $\Delta\phi_{\mu-X} < 170°$.

After applying these criteria, this selection mainly contains events with genuine (LP) or fake (CC) muons and fake missing transverse momentum due to mismeasurement. The CC component is the dominant contribution, although a significant amount of LP remains in this sample. A larger signal component is present than in the muon LP enriched selection and again all muon data events which pass the final event selection (see section 8.2) are present in this sample. The distributions of the key kinematic quantities of the muon CC enriched selection are presented in figures 7.18 to 7.22. The data are the points. The combined SM prediction is given by the open histogram and the shaded band represents the total SM error (see section 7.5). The individual components of the SM prediction are also displayed numerically. The signal component is given by the full histogram.

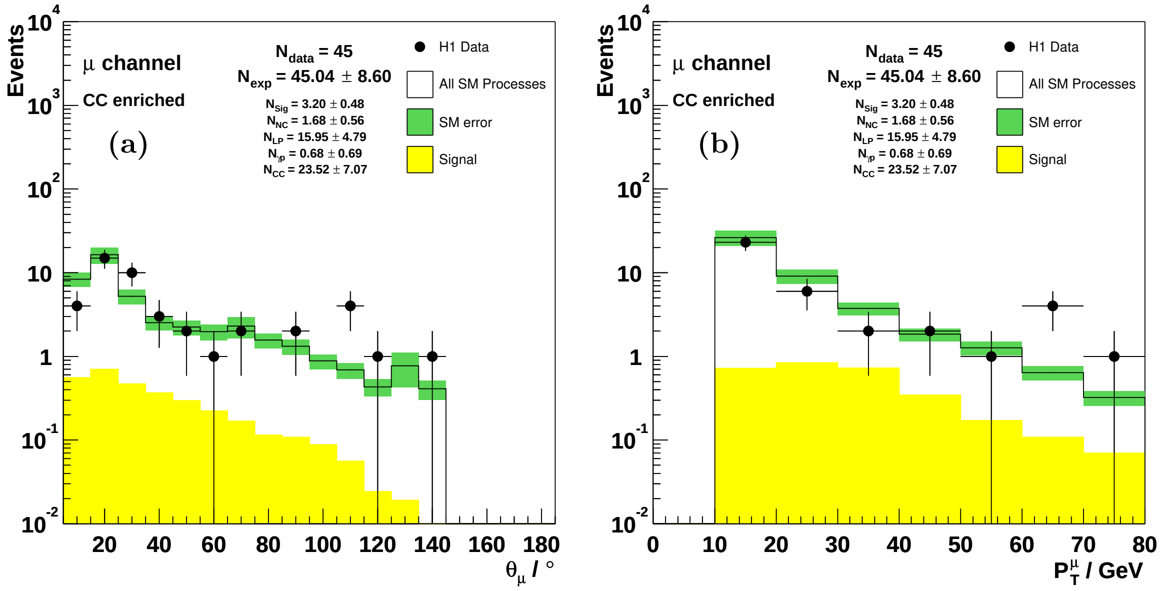

Figure 7.18: The θ_μ (a) and P_T^μ (b) distributions of the muon CC enriched selection.

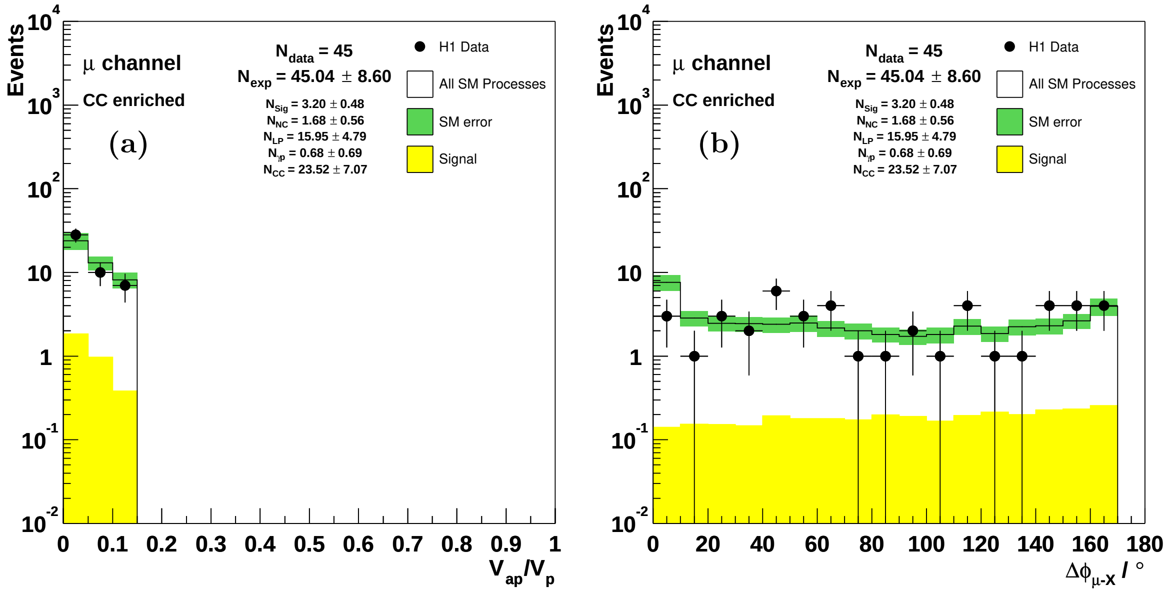

Figure 7.19: The $\frac{V_{ap}}{V_p}$ (a) and $\Delta\phi_{\mu-X}$ (b) distributions of the muon CC enriched selection.

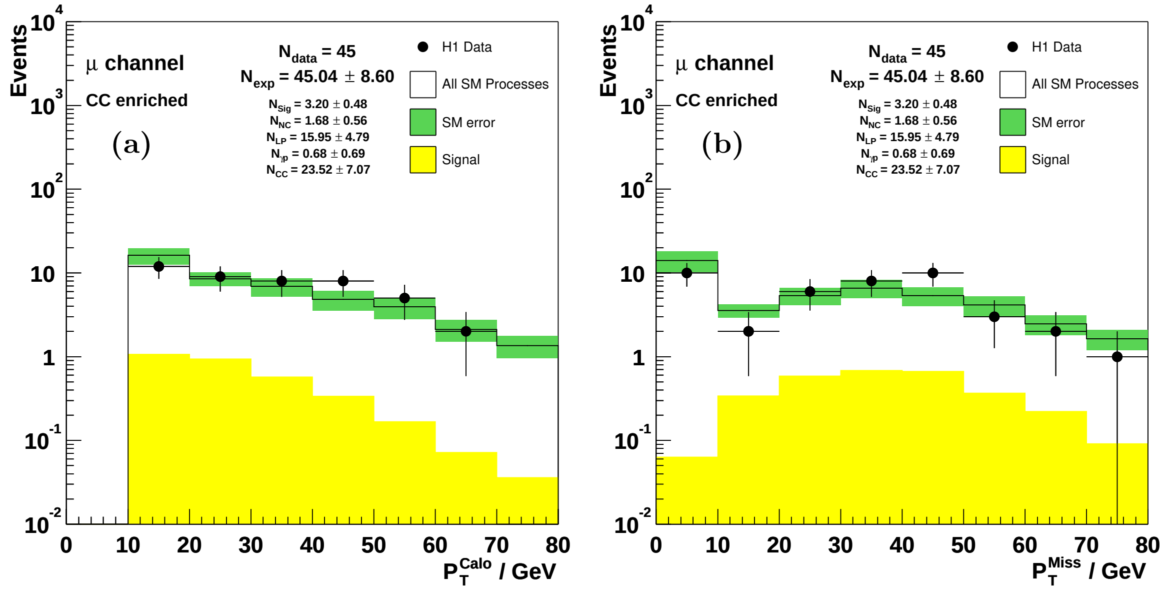

Figure 7.20: The P_T^{calo} (a) and P_T^{miss} (b) distributions of the muon CC enriched selection.

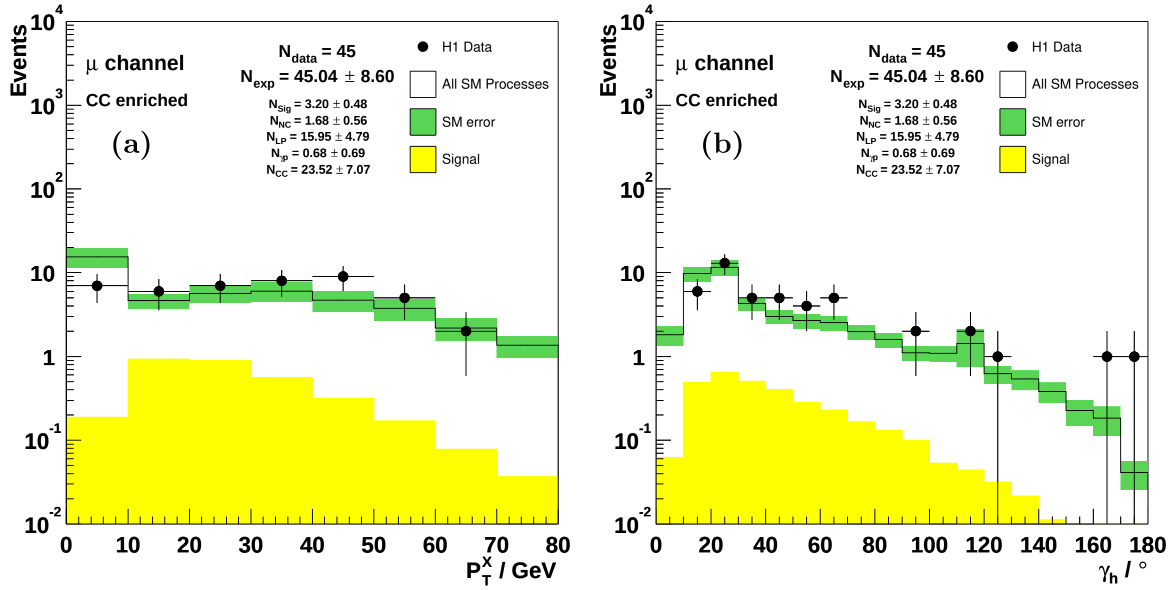

Figure 7.21: The P_T^X (a) and γ_h (b) distributions of the muon CC enriched selection.

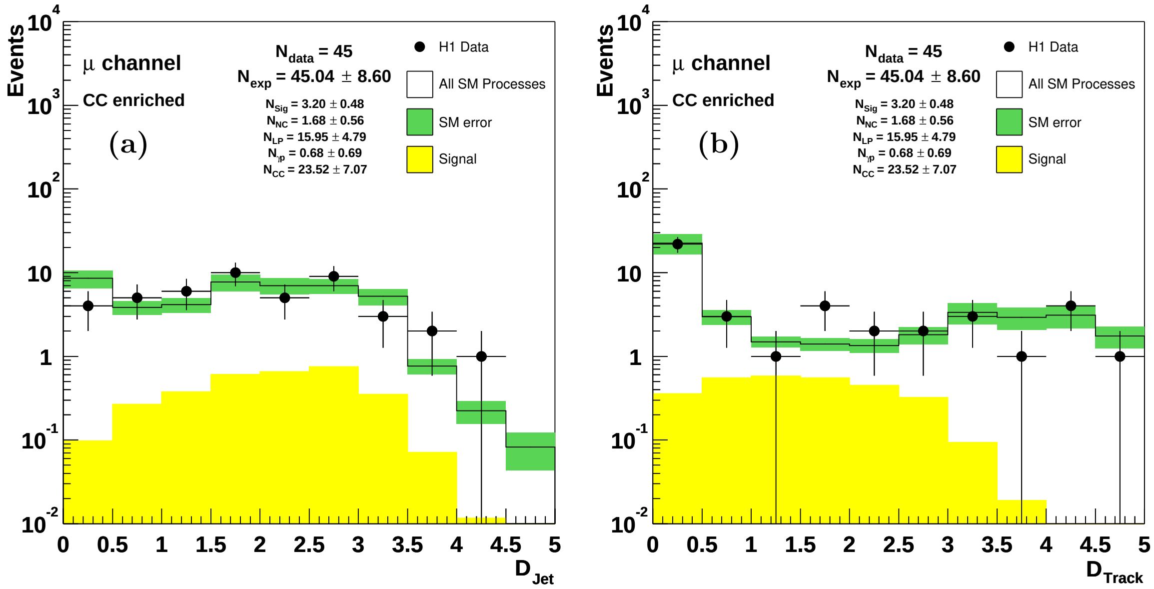

Figure 7.22: The D_{jet} (a) and D_{track} (b) distributions of the muon CC enriched selection.

7.5 Summary

Selection	Data	SM Expectation	Enriched Process	Signal
Electron NC	1587	1786 $\pm$ 514	1710 $\pm$ 513	10.80 $\pm$ 1.62
Electron CC	22	23.27 $\pm$ 4.83	15.68 $\pm$ 4.72	6.44 $\pm$ 0.97
Muon LP	25	29.18 $\pm$ 6.20	19.42 $\pm$ 5.83	2.79 $\pm$ 0.42
Muon CC	45	45.04 $\pm$ 8.60	23.52 $\pm$ 7.07	3.20 $\pm$ 0.48

Table 7.1: Observed and predicted event rates in the enriched samples. The "enriched process" column refers to the dominant contribution, for example NC in the Electron NC selection.

The results of the background enriched selections are summarised in table 7.1. The total number of data events contained in each selection is in good agreement with the total prediction from all SM processes. The distributions of all quantities in all samples are well described in both shape and normalisation in the kinematic regions not dominated by signal processes. However, an excess of data events is visible at high P_T in the three low statistics enriched selections, a region of phase space dominated by signal processes.

The data excess at high P_T^X in the electron CC enriched selection displayed in figure 7.10 is also present in the final electron selection described in section 8.1. Both the muon LP and CC enriched selections contain all data events that pass the final muon selection described in section 8.2. These events account for the excess seen in some of the distributions of the muon enriched samples, notably at high P_T^μ in both selections and, similarly to the electron CC enriched selection, at high P_T^X in the muon LP enriched selection. The data excess visible at low $\frac{V_{ap}}{V_p}$ in the muon LP enriched selection is also due to events contained in the final muon selection.

The level of agreement of these samples is used to determine the systematic errors attributed to the background MCs used in this analysis: RAPGAP (NC), GRAPE (LP) and DJANGO CC are all assigned systematic errors of 30%. Note that this figure does not represent the typical accuracy of the predictions made by these simulations, but rather the level of agreement between data and MC in the region of phase space selected by the enriched samples.

The photoproduction contribution from PYTHIA (γp) is conservatively assigned a systematic error of 75%, due to the reweight performed as described in section 6.4. However, it is found that this contribution is minimal in the final electron selection and that no events contribute to the final muon selection.

The systematic error assigned to EPVEC in the enriched selections is the theoretical uncertainty of 15% quoted in section 3.4.2. In the final selections, where the prediction from EPVEC is the dominant contribution to the total SM prediction, this theoretical uncertainty is combined with the experimental systematics described in section 9.1. The error of the total SM expectation is the combined total (statistical and systematic) errors of all simulated processes.

Chapter 8

Final Event Selections

The discriminatory power of the enriched selections described in chapter 7 is used to form final electron and muon selections dominated by signal processes. This is first done by extending the basic phase space selection defined in section 6.3 to include four further cuts.

By requiring $P_T^{miss} > 12$ GeV some of the NC, lepton pair and photoproduction background is removed from both phase space samples. It can be seen in figure 6.2 that the bulk of the prediction at low P_T^{miss} is due to non-signal processes in both channels. It can also be seen that the lowest bin of the electron phase space P_T^{miss} distribution is suppressed by the $P_T^{calo} > 12$ GeV basic phase space cut. The isolation criteria included in the electron NC and muon LP enriched selections, namely $D_{jet} > 1.0$ and $D_{track} > 0.5$, are also included in the final selections to remove CC and photoproduction background. In the final electron selection the D_{track} cut is only employed for $\theta_e > 45°$ as described in section 7.1. Finally, a cut of $\frac{V_{ap}}{V_p} < 0.5$ is applied to remove NC and photoproduction background. This cut is tightened to $\frac{V_{ap}}{V_p} < 0.15$ as used in the electron and muon CC enriched selections, but for different regions of phase space in the final electron and muon selections.

The common cuts in electron and muon final selections are summarised in table 8.1 and form the final phase space selection. Further cuts are applied to this sample in order to select signal events containing either isolated electrons or muons. These selections are described in the following two sections.

Variable	Cut
P_T^l	> 10 GeV
θ_l	$5° < \theta_l < 140°$
P_T^{calo}	> 12 GeV
P_T^{miss}	> 12 GeV
D_{jet}	> 1.0
D_{track}	$> 0.5^{\dagger}$
$\frac{V_{ap}}{V_p}$	< 0.5

†*Only applied for $\theta_e > 45°$ in events containing isolated electrons.*

Table 8.1: The final phase space selection.

8.1 Events Containing Isolated Electrons

In addition to the cuts listed in table 8.1, further cuts are applied to select an event sample dominated by signal events containing isolated electrons. Figure 8.1 shows the correlation between P_T^e and $\frac{V_{ap}}{V_p}$ of events in the final electron phase space selection. Signal events are predominantly found at low values of $\frac{V_{ap}}{V_p}$, whereas NC and lepton pair events are distributed mainly at low P_T^e across a large range of $\frac{V_{ap}}{V_p}$. The remaining CC component occupies a similar region of phase space to signal events. The existing requirement of $\frac{V_{ap}}{V_p} < 0.5$ is extended to $\frac{V_{ap}}{V_p} < 0.15$ as used in the electron CC enriched selection, but only for events with $P_T^e < 25$ GeV as shown in figure 8.1. This allows a greater acceptance of signal events whilst removing a large part of the NC and lepton pair background.

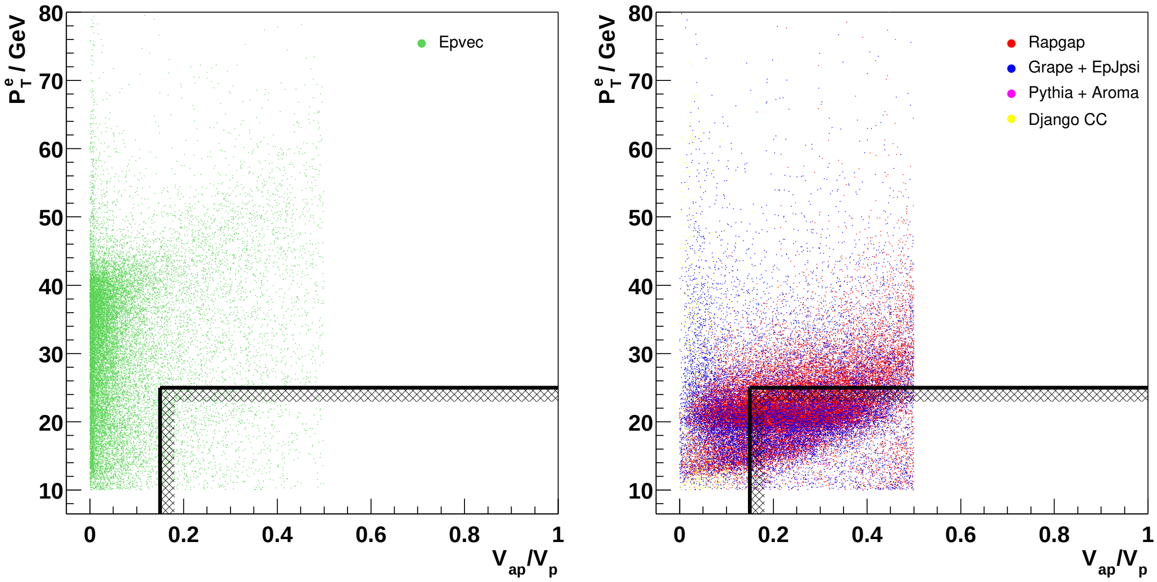

Figure 8.1: The correlation between P_T^e and $\frac{V_{ap}}{V_p}$ of events in the final electron phase space selection. Epvec (signal) events are shown on the left and background events are shown on the right. The applied cuts are depicted by the lines.

Further reduction of NC and lepton pair background is achieved by selecting events with high values of ζ^2. Figure 8.2 shows the correlation between ζ^2 and P_T^{calo} of events in the final electron phase space selection. Background events are mainly found at low values of ζ^2, with only the lepton pair contribution significant at high P_T^{calo}. Signal events are found across the whole of the ζ^2 spectrum, including a dense band at values of $P_T^{calo} \approx \frac{m_W}{2}$. A requirement of $\zeta^2 > 5000$ GeV^2 is imposed but only for events with $P_T^{calo} < 25$ GeV, as illustrated in figure 8.2

The electron CC enriched selection cuts $\Delta\phi_{e-X} < 160°$ and $\delta_{miss} > 5$ GeV are also added to the final electron selection to remove NC and lepton pair background. However, the δ_{miss} requirement is only imposed when only one electron is detected, which has the same charge as the beam lepton: the signature of a NC event. Finally, a requirement of no isolated muons is included in the final electron selection so that

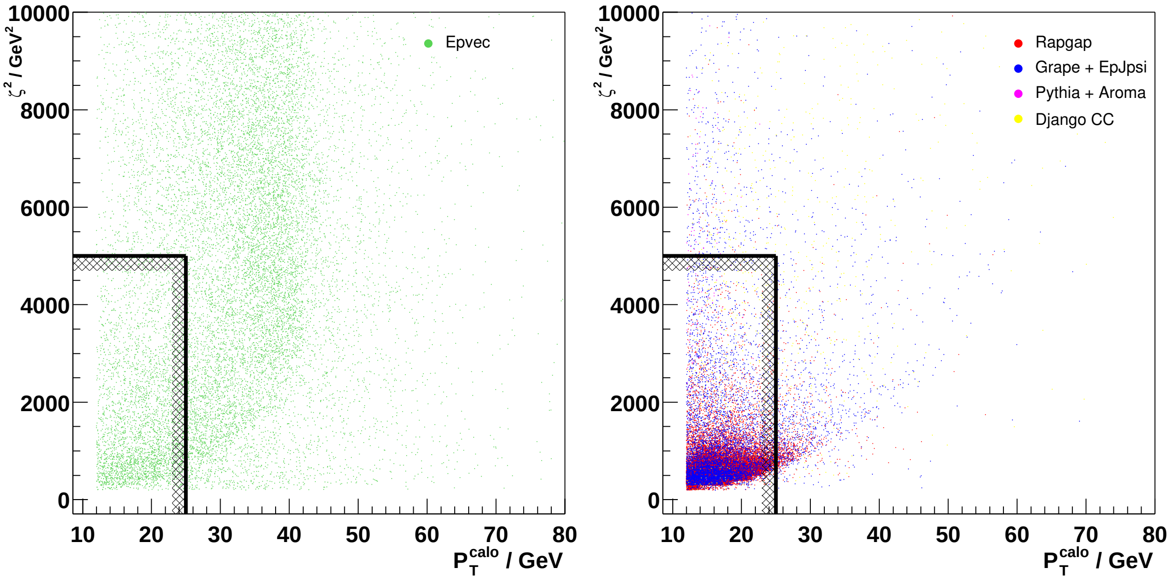

Figure 8.2: The correlation between ζ^2 and P_T^{calo} of events in the final electron phase space selection. Epvec (signal) events are shown on the left and background events are shown on the right. The applied cuts are depicted by the lines.

any given event may only contribute to one of the two signal channels examined in this analysis. The final electron selection including the final phase space selection is summarised in table 8.2.

The distributions of the key kinematic quantities of the final electron selection are presented in figures 8.3 to 8.8. The data are the points. The combined SM prediction is given by the open histogram and the shaded band represents the total SM error (see section 9.1). The individual components of the SM prediction are also displayed numerically. The signal component is given by the dashed histogram.

The data are found mainly at low values of θ_e (figure 8.3a) and γ_h (figure 8.6b), consistent with the signal expectation. A significant portion of the remaining background component in this selection is also visible at central values of θ_e and is mainly due to NC events. The distributions of P_T^e (figure 8.3b), P_T^{calo} (figure 8.5a) and P_T^{miss}

Variable	Cut
P_T^e	> 10 GeV
θ_e	$5^\circ < \theta_e < 140^\circ$
P_T^{calo}	> 12 GeV
P_T^{miss}	> 12 GeV
D_{jet}	> 1.0
D_{track}	> 0.5 for $\theta_e > 45^\circ$
$\frac{V_{ap}}{V_p}$	< 0.5 (< 0.15 for $P_T^e < 25$ GeV)
ζ^2	> 5000 GeV^2 for $P_T^{calo} < 25$ GeV
$\Delta\phi_{e-X}$	$< 160^\circ$
δ_{miss}	> 5 GeV†
# isolated μ	0

† *If only one e candidate is detected, which has the same charge as the beam lepton.*

Table 8.2: The final electron selection.

(figure 8.5b) all exhibit a large spread in the data events centred around $\frac{m_W}{2}$, again consistent with the signal expectation. The clustering of data events at low values of $\frac{V_{ap}}{V_p}$ (figure 8.4a) and the even spread across all values of $\Delta\phi_{e-X}$ (figure 8.4b) are also both in agreement with the distribution of the signal prediction. However, an excess of data events over the SM prediction is visible at high P_T^X (figure 8.6a). The results of the final electron selection are discussed in chapter 9.

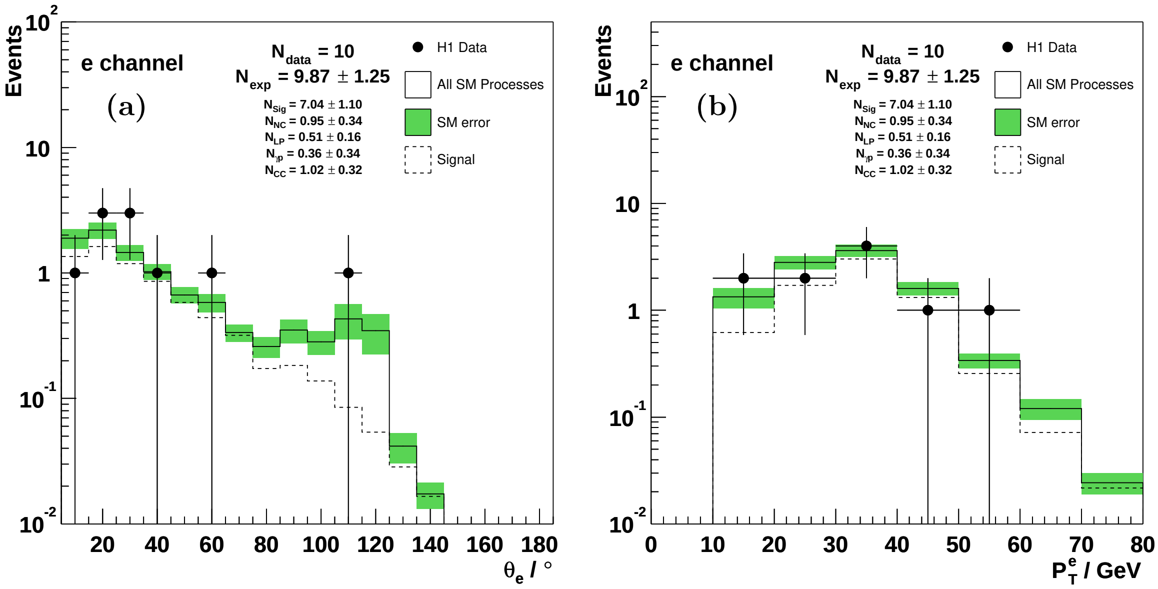

Figure 8.3: The θ_e (a) and P_T^e (b) distributions of the final electron selection.

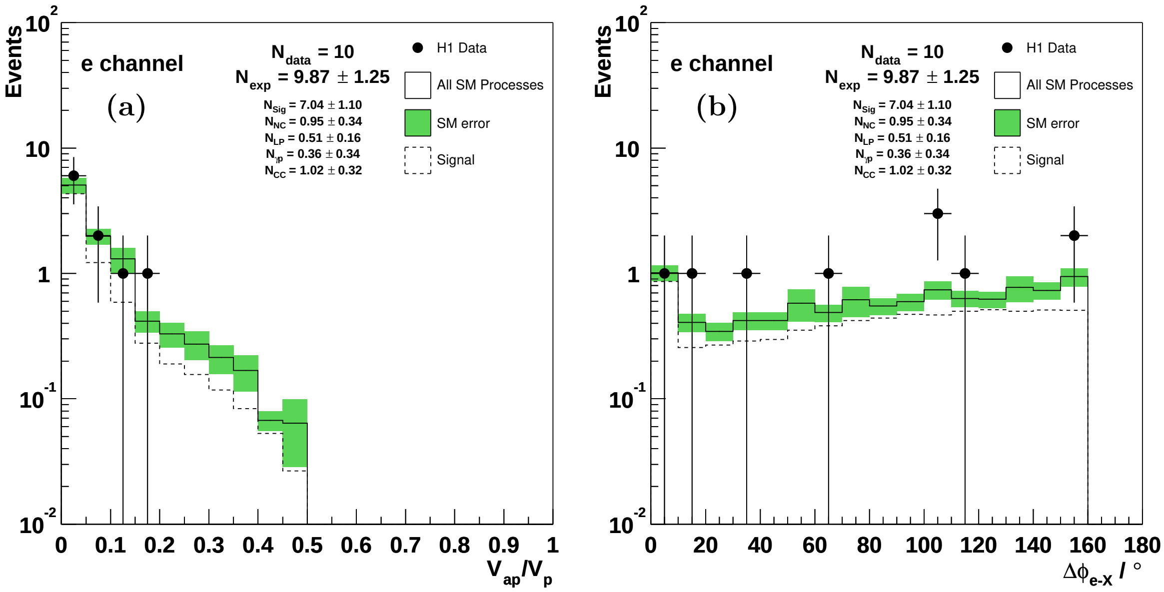

Figure 8.4: The $\frac{V_{ap}}{V_p}$ (a) and $\Delta\phi_{e-X}$ (b) distributions of the final electron selection.

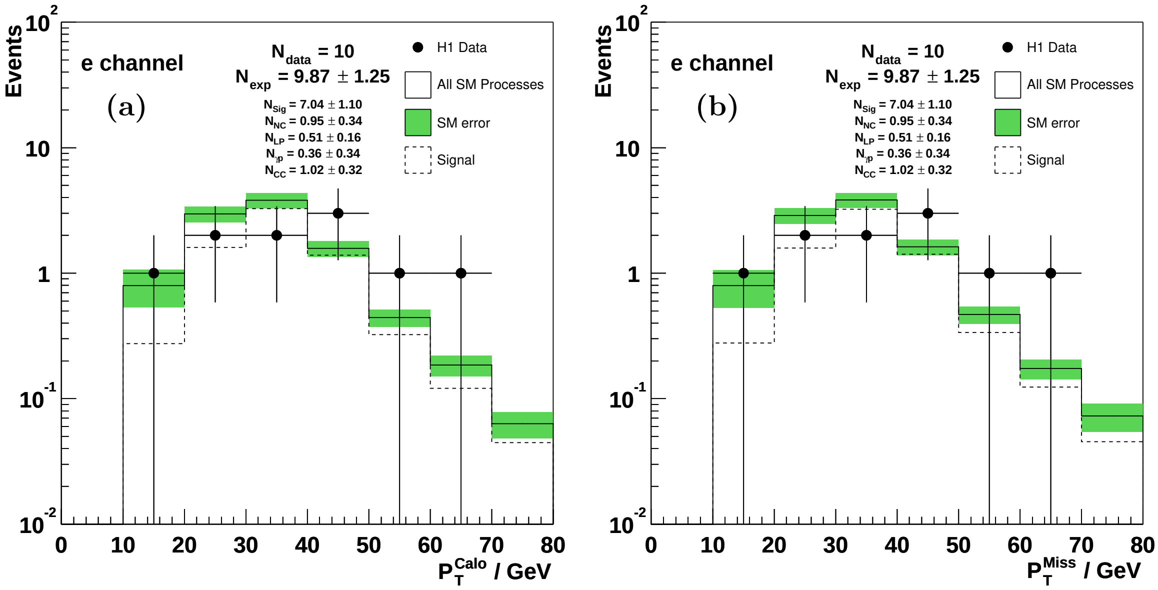

Figure 8.5: The P_T^{calo} (a) and P_T^{miss} (b) distributions of the final electron selection.

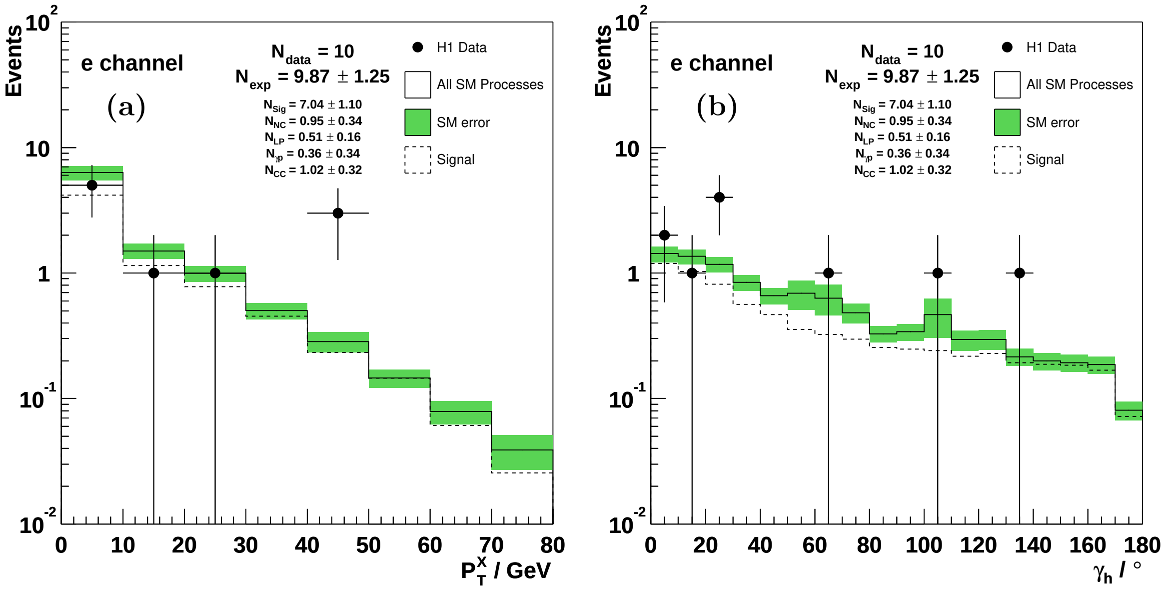

Figure 8.6: The P_T^X (a) and γ_h (b) distributions of the final electron selection.

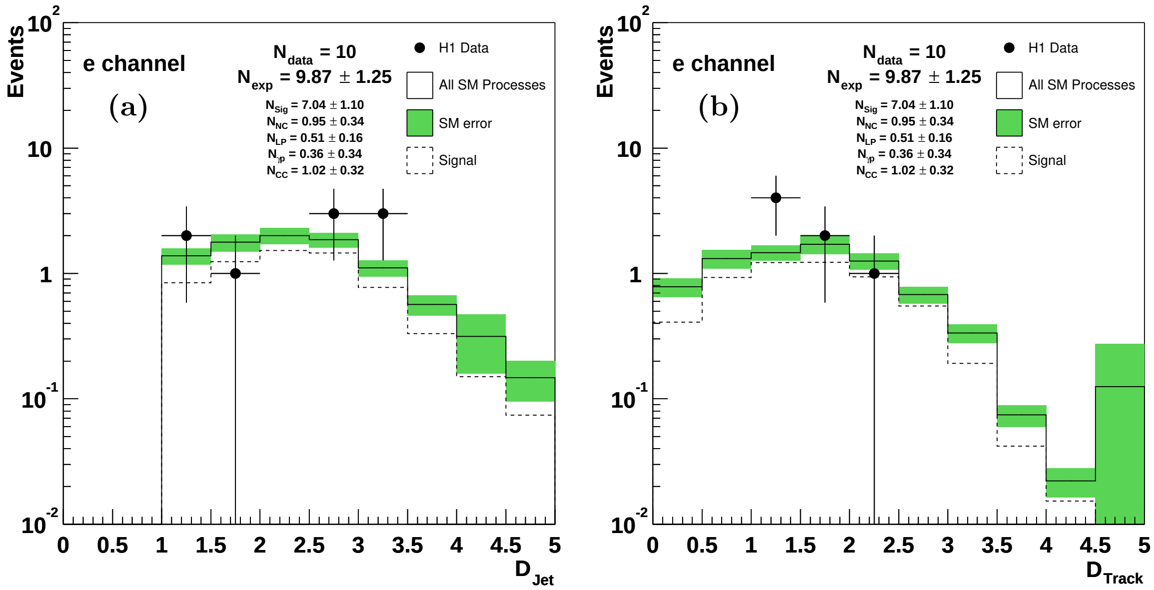

Figure 8.7: The D_{jet} (a) and D_{track} (b) distributions of the final electron selection.

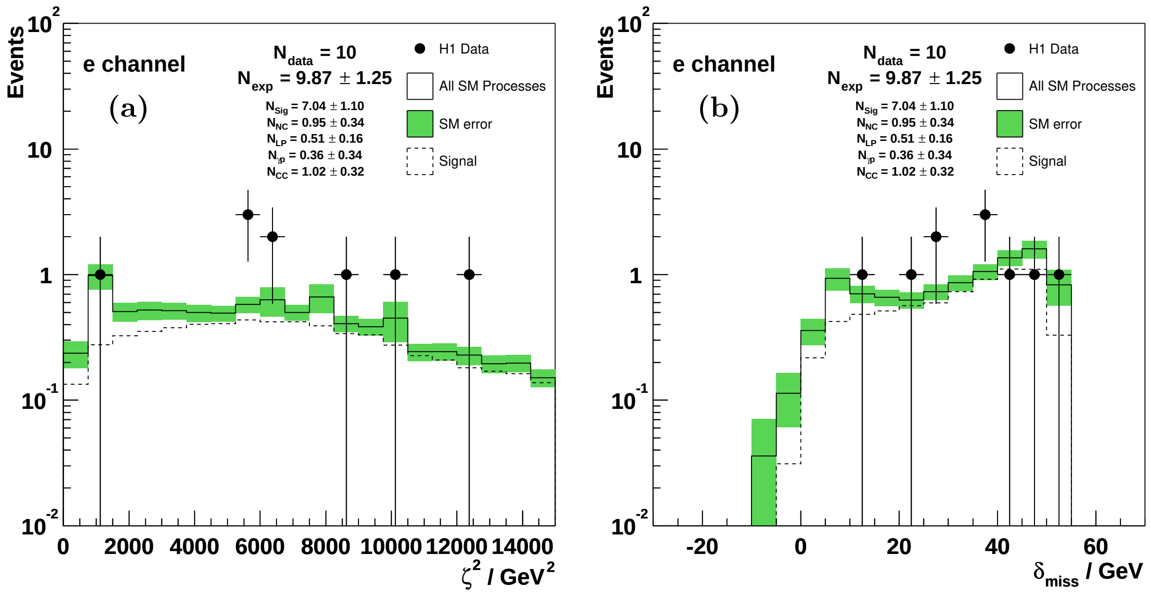

Figure 8.8: The ζ^2 (a) and δ_{miss} (b) distributions of the final electron selection.

8.2 Events Containing Isolated Muons

To obtain an event sample dominated by muon signal events, additional cuts are applied to those listed in table 8.1. Figure 8.9 shows the correlation between P_T^{calo} and $\frac{V_{ap}}{V_p}$ of events in the final muon phase space selection. Similarly to the final electron phase space sample, signal and CC events are found predominantly at low values of $\frac{V_{ap}}{V_p}$. Lepton pair and photoproduction events are found across a large range of $\frac{V_{ap}}{V_p}$ but mainly at low values of P_T^{calo}. The $\frac{V_{ap}}{V_p} < 0.15$ cut from the muon enriched CC selection is hence also applied to the final muon selection for events with $P_T^{calo} <$ 25 GeV, as shown in figure 8.9.

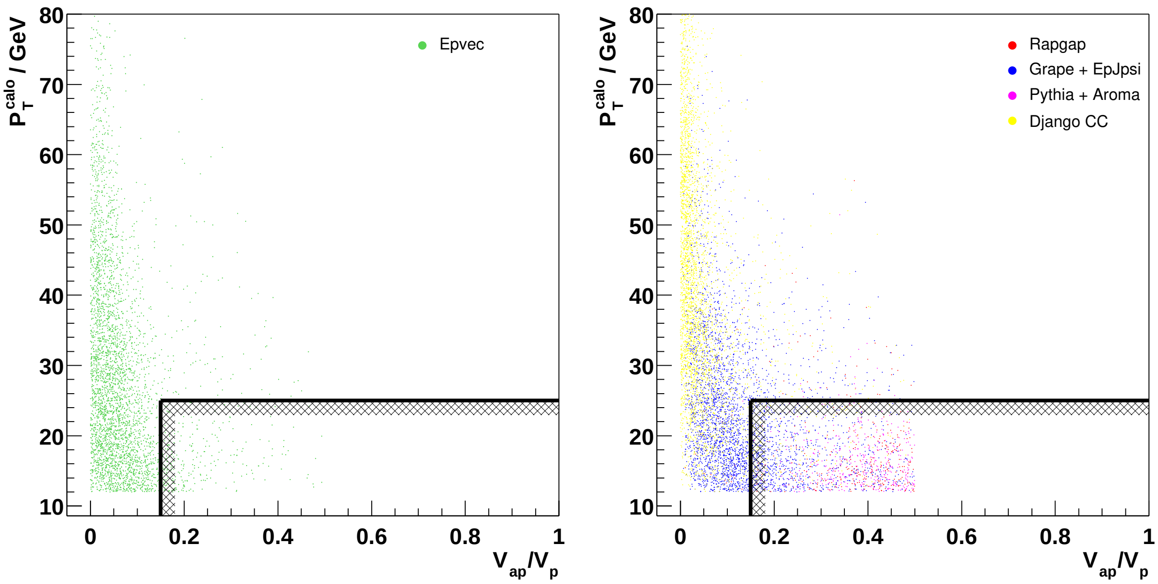

Figure 8.9: The correlation between P_T^{calo} and $\frac{V_{ap}}{V_p}$ of events in the final muon phase space selection. Epvec (signal) events are shown on the left and background events are shown on the right. The applied cuts are depicted by the lines.

As stated in chapter 6, the P_T^{calo} cut imposed in the basic phase selection is equivalent to a cut on P_T^X in events containing isolated muons. The bulk of the remainder of the prediction in the muon basic phase space selection at low P_T^X is due to elastic muon pair events where the scattered electron provides significant P_T^{calo}, as shown in figure 6.10. The contribution from signal events at low P_T^X is very low, so a cut of $P_T^X > 12$ GeV is added to the final muon selection to remove further background.

The muon CC enriched selection acoplanarity cut, $\Delta\phi_{\mu-X} < 170°$, is also included in the final muon selection to reject NC background events. Finally, events in this selection must contain only one isolated muon. Whilst electron signal events may contain two electrons if the scattered electron is detected in the event, muon signal events intrinsically contain only one isolated muon. The final muon selection including the final phase space selection is summarised in table 8.3.

The distributions of the key kinematic quantities of the final muon selection are presented in figures 8.10 to 8.14. The data are the points. The combined SM prediction is given by the open histogram and the shaded band represents the total SM error (see section 9.1). The individual components of the SM prediction are also displayed numerically. The signal component is given by the dashed histogram.

As in the final electron selection, the data are found at low values of θ_μ (figure 8.10a) and $\frac{V_{ap}}{V_p}$ (figure 8.11a) and across all values of $\Delta\phi_{\mu-X}$ (figure 8.11b). However, an excess of data events over the SM prediction is observed in this selection. This is visible in most kinematic distributions and in particular at high P_T^X (figure 8.13a) and low γ_h (figure 8.13b). The distributions of P_T^μ (figure 8.10b), P_T^{calo} (figure 8.12a) and P_T^{miss} (figure 8.12b) all exhibit a similarly large spread in the data events to the distributions in the final electron selection, although more events are present at high P_T than in the electron channel. The results of the final muon selection are discussed in chapter 9.

Variable	Cut
P_T^μ	> 10 GeV
θ_μ	$5° < \theta_\mu < 140°$
P_T^{calo}	> 12 GeV
P_T^{miss}	> 12 GeV
D_{jet}	> 1.0
D_{track}	> 0.5
$\frac{V_{ap}}{V_p}$	< 0.5 (< 0.15 for $P_T^{calo} < 25$ GeV)
$\Delta\phi_{\mu-X}$	$< 170°$
P_T^X	> 12 GeV
# isolated μ	1

Table 8.3: The final muon selection.

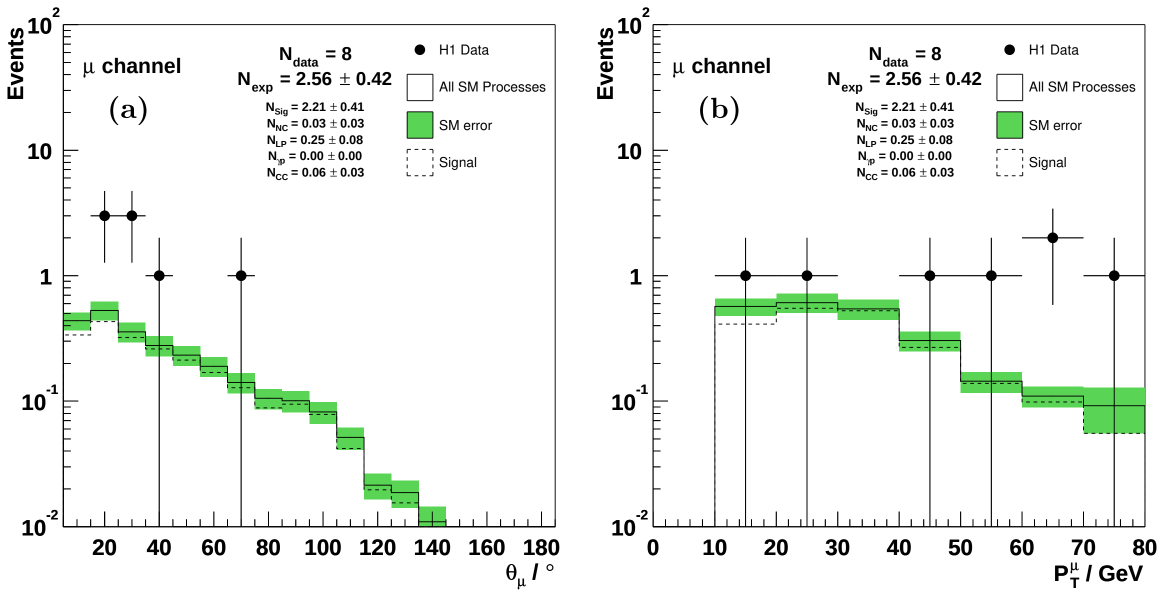

Figure 8.10: The θ_μ (a) and P_T^μ (b) distributions of the final muon selection.

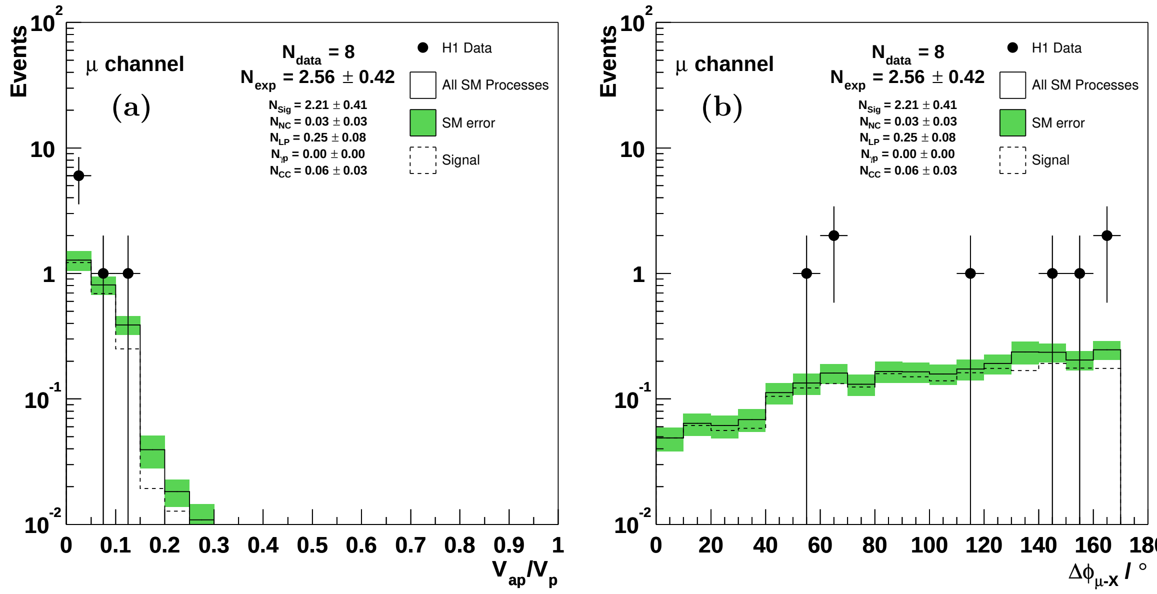

Figure 8.11: The $\frac{V_{ap}}{V_p}$ (a) and $\Delta\phi_{\mu-X}$ (b) distributions of the final muon selection.

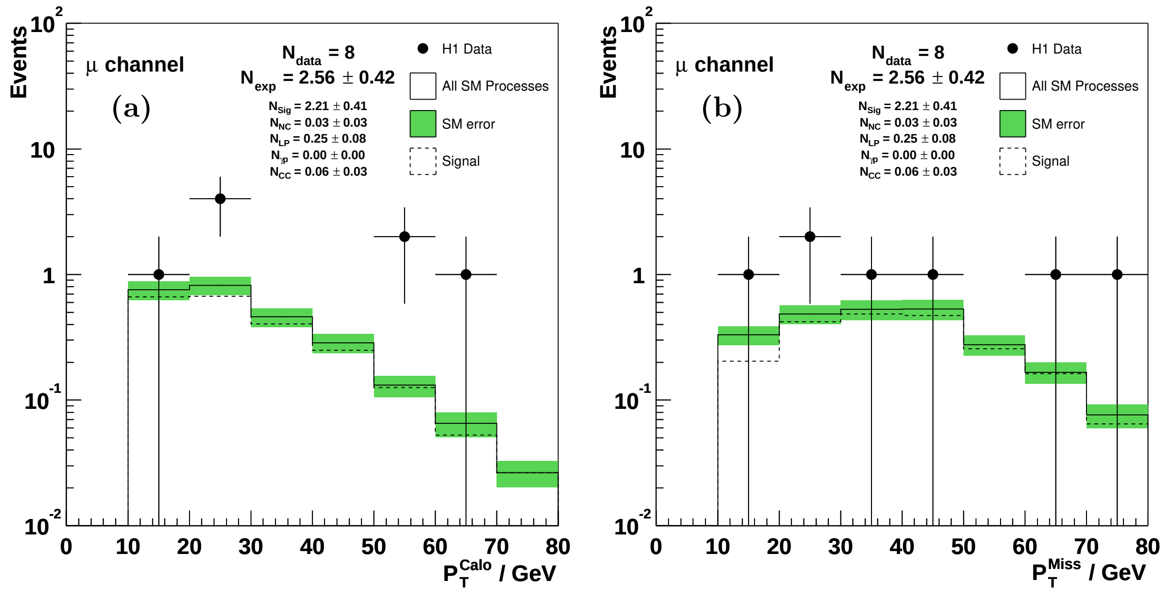

Figure 8.12: The P_T^{calo} (a) and P_T^{miss} (b) distributions of the final muon selection.

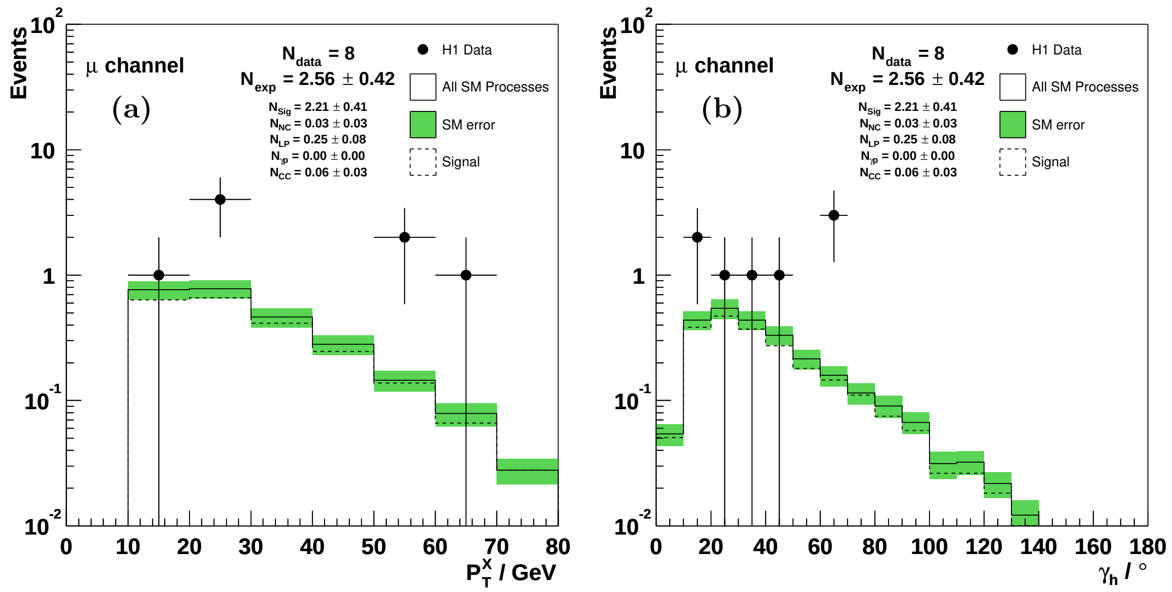

Figure 8.13: The P_T^X (a) and γ_h (b) distributions of the final muon selection.

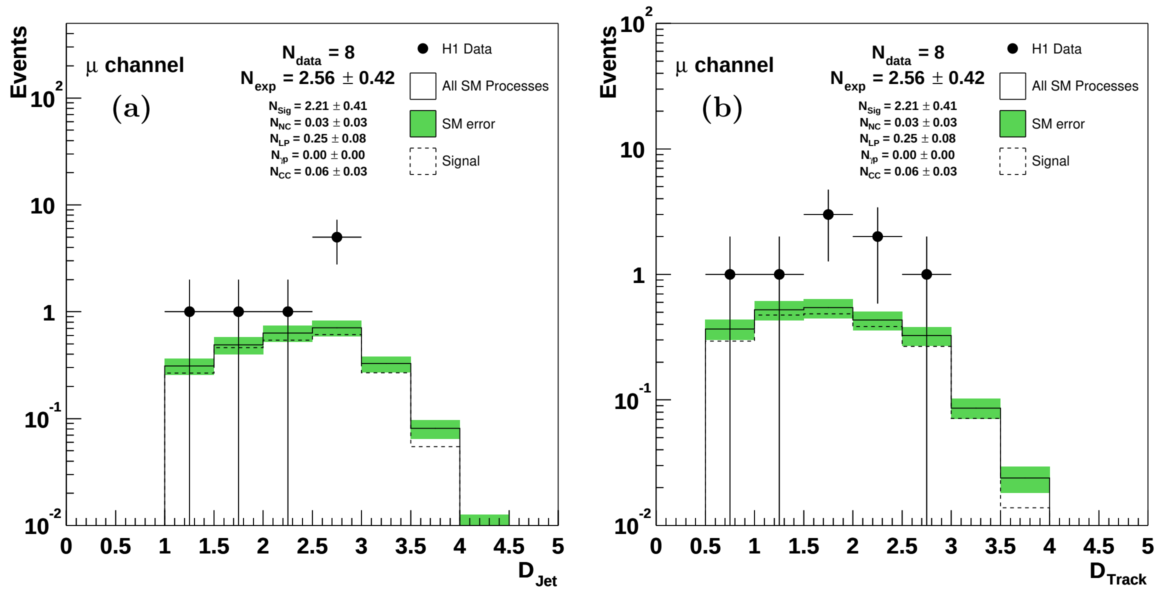

Figure 8.14: The D_{jet} (a) and D_{track} (b) distributions of the final muon selection.

8.3 Selection Efficiencies

The selection efficiency, ε_{sel} of the final event selections for a given bin is studied using EPVEC and defined as

$$\varepsilon_{\text{sel}} = \frac{\text{N}_{\text{rec}}}{\text{N}} \tag{8.1}$$

where N is the total number of events generated in the bin and N_{rec} is the number of events reconstructed in the bin after the final event selection. The selection efficiency of the electron and muon final selections are displayed in figure 8.15 as a function of generated hadronic transverse momentum, P_T^XGen.

The selection efficiency in the electron channel is $40-50\%$ across the full P_T^XGen spectrum. In the muon channel, at low P_T^XGen the selection efficiency is very low due to the P_T^{calo} cut in the basic phase space selection, which is equivalent in signal events to a cut on P_T^X as explained in section 6.3.1. However, at P_T^XGen > 25 GeV the muon channel is compatible with the electron channel with a selection efficiency greater than 40%.

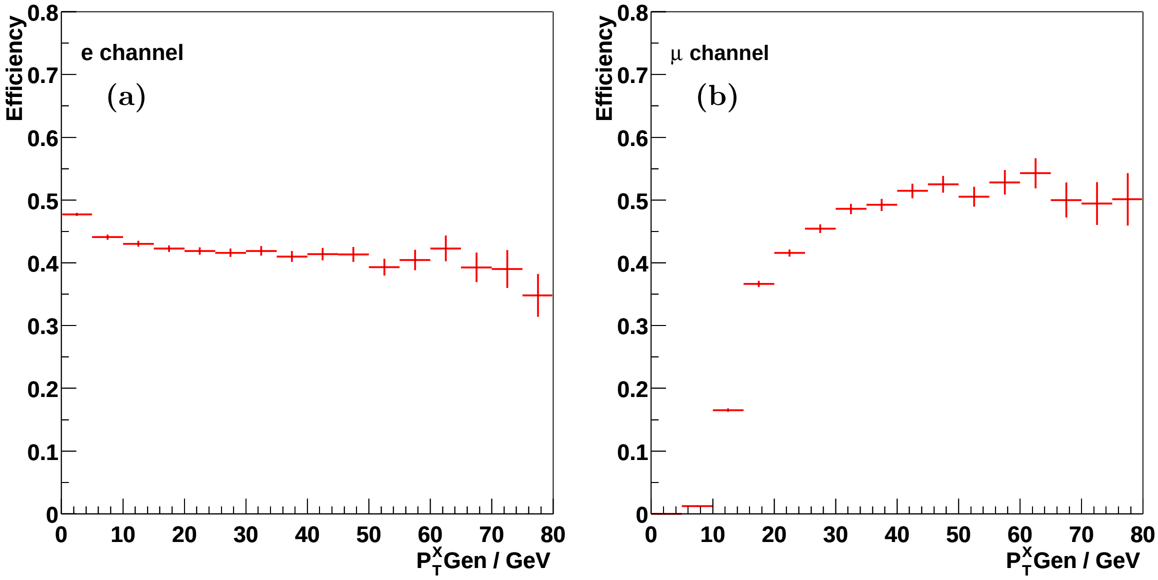

Figure 8.15: Selection efficiencies in the final electron (a) and muon (b) selections as a function of P_T^XGen, calculated using EPVEC.

Chapter 9

Results and Discussion

The results of the final event selection are presented in this chapter. The experimental systematic uncertainties are introduced in section 9.1, followed by a full breakdown of the final event selections in section 9.2. The measured cross section is presented in section 9.3 and the results are discussed in section 9.4.

9.1 Systematic Uncertainties

The systematic uncertainties attributed to background processes are determined from the level of agreement seen in the background studies as described in chapter 7. The total systematic uncertainty on the signal expectation in the final selections is the theoretical uncertainty of 15% quoted in section 3.4.2 combined in quadrature with the experimental uncertainties described below. The experimental uncertainties on the signal expectation and the acceptance used in the measured cross section (see section 9.3) are determined by varying experimental quantities by $\pm$ 1 standard deviation and recalculating the expectation or cross section.

The systematic uncertainties on electron quantities are taken from the H1 Neutral Current analysis [43, 106]. The total systematic uncertainty on the electromagnetic energy scale ranges from 0.7% in the backward region to 3.0% in the statistically limited forward region, as shown in figure 9.1. The uncertainty on the electron polar angle is 1 mrad, 2 mrad and 3 mrad for $\theta_e > 135°$, $120° < \theta_e < 135°$ and $\theta_e < 120°$ respectively. The uncertainty on the electron azimuthal angle is 1 mrad. The uncertainty on electron identification efficiency is 2%. Additionally, an error of 3% is included due to the track-cluster link requirement described in section 6.1.1 [41]. This is higher than in the H1 Neutral Current analysis due to the more stringent track definition.

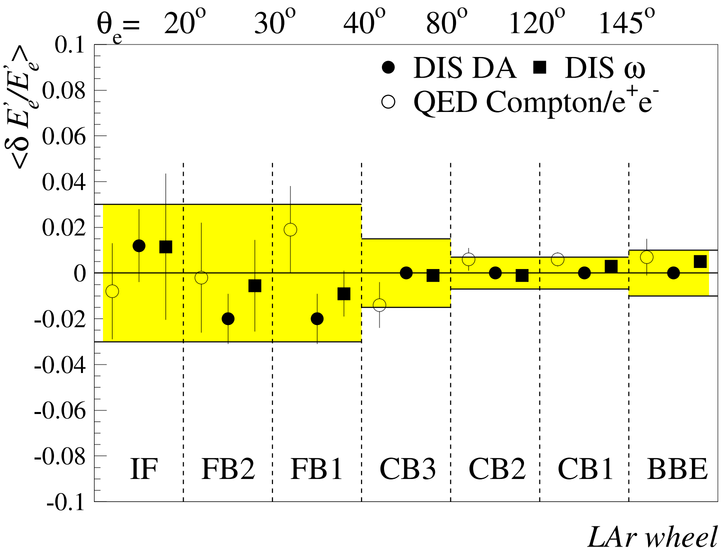

Figure 9.1: The electromagnetic energy scale determined by different calibration methods as a function of polar angle and corresponding LAr wheel. The shaded band shows the range of systematic uncertainty on the energy scale. Taken from [106].

The uncertainty on the muon energy scale is 5%, determined from the P_T balance of a data sample of muon pair events [113]. The muon identification efficiency is evaluated using the same data sample and is assigned an uncertainty of 6%.

The uncertainty on the muon polar and azimuthal angles is 3 mrad and 1 mrad respectively.

Uncertainties on the hadronic system are evaluated using a standard NC DIS sample [114, 115]. The uncertainty on the hadronic energy scale is 4%. The uncertainties on the measurements of the hadronic polar and azimuthal angle are both 20 mrad. The agreement between data and Django NC Monte Carlo is shown in figure 9.2, which compares the hadronic polar angle measured using two different methods. Signal events tend to have hadronic jets in the central or forward region (see figures 8.6b and 8.13b) and from figure 9.2 the quoted systematic of 20 mrad is adequate in this region. Additionally, an error of ± 0.02 on the measurement of $\frac{V_{ap}}{V_p}$ is employed, as used in the H1 Charged Current analysis [43, 106].

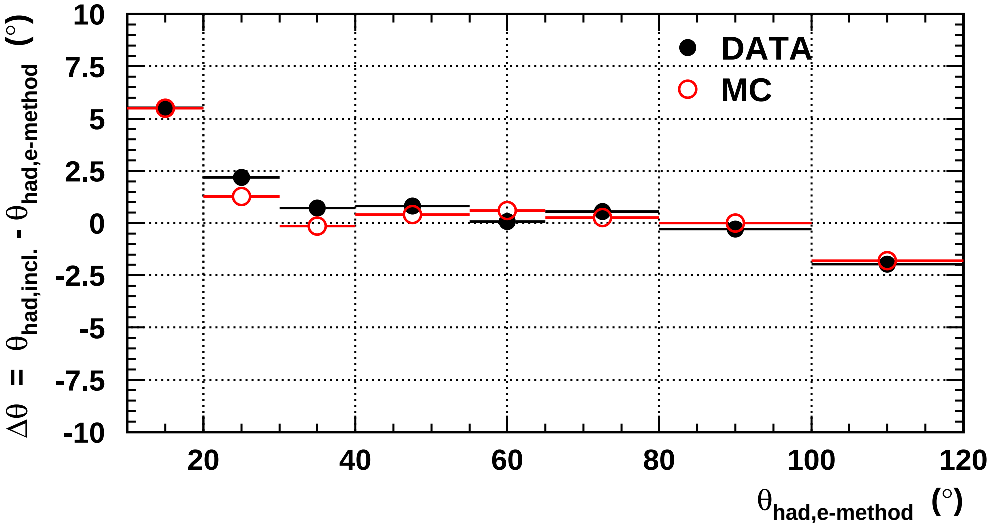

Figure 9.2: The difference $\Delta\theta$ of the hadronic polar angle reconstructed from the inclusive and electron methods for a standard NC DIS sample. The agreement between data and Django Monte Carlo is shown as a function of hadronic polar angle reconstructed using the electron method. Taken from [114].

For events in the final electron selection the uncertainty on the trigger efficiency is negligible as the LAr trigger is ≈ 100% efficient (see section 4.4.1). The uncertainty on the trigger efficiency in the final muon selection is composed of two parts added in quadrature [41]. A 2% uncertainty is added in quadrature to 30% of the inefficiency of the LAr CC triggers[1], resulting in a total uncertainty in the muon channel of 6% for $P_T^X < 25$ GeV and 3% for $P_T^X > 25$ GeV. Finally, the uncertainty on the luminosity measurement of the data analysed in this thesis is 1.5% [43].

The total error on the expectation from each process is the statistical and systematic errors combined in quadrature. The total SM error is the total error of each process combined in quadrature.

9.2 Results

9.2.1 The Final Electron Selection

The results of the final electron selection described in section 8.1 are presented in the following tables. Table 9.1 contains a detailed breakdown of the results from data and the expectation from all SM processes in four bins of hadronic transverse momentum, P_T^X. The signal expectation is the dominant contribution and the highest background predictions are due to NC and CC processes. The contribution of the background prediction is greatest in the two lowest P_T^X bins. The NC and photoproduction components are combined in the table, where the photoproduction component only contributes to the lowest bin in P_T^X and is equal to 0.36 ± 0.34.

Table 9.2 presents the data results, the combined prediction from all SM processes and the expectation from signal and background processes in the final electron selection as a function of P_T^X. Summed over all P_T^X, the total prediction from the SM is in agreement with the total number of observed data events: 10 data events are observed compared to a SM prediction of 9.87 ± 1.25. However, for $P_T^X > 25$ GeV 4 data events are observed compared to a total SM prediction of 1.51 ± 0.26.

[1]This is increased from 15% used in the CC analysis presented in [41] due to the presence of a muon in the final state.

P_T^X (GeV)	Data	Signal	NC & γp	Lepton Pair	CC
< 12	5	4.45 ± 0.71	1.08 ± 0.43	0.44 ± 0.14	0.69 ± 0.22
12 - 25	1	1.32 ± 0.21	0.17 ± 0.09	0.05 ± 0.02	0.17 ± 0.06
25 - 40	1	0.79 ± 0.14	0.03 ± 0.03	0.01 ± 0.01	0.11 ± 0.04
> 40	3	0.48 ± 0.12	0.03 ± 0.03	0.00 ± 0.00	0.05 ± 0.02
Total	10	7.04 ± 1.10	1.31 ± 0.48	0.51 ± 0.16	1.02 ± 0.32

Table 9.1: Observed and predicted event rates in the final electron selection in bins of P_T^X for the complete HERA I e^+p H1 data set. Presented are the observed data events and the breakdown of the expectation from different SM processes: Signal (EPVEC), NC (RAPGAP), Photoproduction (PYTHIA and AROMA), Lepton Pair (GRAPE and EPJPSI) and CC (DJANGO CC). Also given are the total errors (statistical and systematic) combined in quadrature.

P_T^X (GeV)	Data	SM Expectation	Signal	Other SM processes
< 12	5	6.66 ± 0.87	4.45 ± 0.71	2.21 ± 0.50
12 - 25	1	1.70 ± 0.24	1.32 ± 0.21	0.39 ± 0.11
25 - 40	1	0.94 ± 0.15	0.79 ± 0.14	0.15 ± 0.05
> 40	3	0.56 ± 0.13	0.48 ± 0.12	0.08 ± 0.04
Total	10	9.87 ± 1.25	7.04 ± 1.10	2.84 ± 0.60
< 25	6	8.37 ± 1.07	5.77 ± 0.91	2.60 ± 0.56
> 25	4	1.51 ± 0.26	1.27 ± 0.25	0.24 ± 0.08

Table 9.2: Observed and predicted event rates in the final electron selection in bins of P_T^X for the complete HERA I e^+p H1 data set. Presented are the observed data events, the total expectation from all SM processes, and the prediction from the signal and background components. Also given are the total errors (statistical and systematic) combined in quadrature.

9.2.2 The Final Muon Selection

The results of the final muon selection described in section 8.2 are presented in the following tables. Table 9.3 contains a detailed breakdown of the results from data and the expectation from all SM processes in three bins of hadronic transverse momentum, P_T^X. As in the final electron selection, the dominant contribution to the SM prediction is due to signal processes and the majority of the background is present at low P_T^X. The predictions from lepton pair and CC are the largest contributions to the expectation from background processes.

Table 9.4 presents the data results, the combined prediction from all SM processes and the expectation from signal and background processes in the final muon selection as a function of P_T^X. In contrast to the final electron selection, the total number of observed data events exceeds the total prediction from all SM processes: 8 data events are observed compared to a SM prediction of 2.56 ± 0.42. This discrepancy is larger at $P_T^X > 25$ GeV, where 6 data events are observed compared to a total SM prediction of 1.38 ± 0.27. Additionally, the contribution of background processes to the total SM prediction is found to be much smaller than in the final electron selection.

P_T^X (GeV)	Data	Signal	NC & γp	Lepton Pair	CC
12 - 25	2	0.99 $\pm$ 0.18	0.03 $\pm$ 0.03	0.14 $\pm$ 0.05	0.01 $\pm$ 0.01
25 - 40	3	0.72 $\pm$ 0.14	0.00 $\pm$ 0.00	0.09 $\pm$ 0.03	0.03 $\pm$ 0.01
> 40	3	0.50 $\pm$ 0.13	0.00 $\pm$ 0.00	0.02 $\pm$ 0.01	0.03 $\pm$ 0.02
Total	8	2.21 $\pm$ 0.41	0.03 $\pm$ 0.03	0.25 $\pm$ 0.08	0.06 $\pm$ 0.03

Table 9.3: Observed and predicted event rates in the final muon selection in bins of P_T^X for the complete HERA I e^+p H1 data set. Presented are the observed data events and the breakdown of the expectation from different SM processes: Signal (EPVEC), NC (RAPGAP), Photoproduction (PYTHIA and AROMA), Lepton Pair (GRAPE and EPJPSI) and CC (DJANGO CC). Also given are the total errors (statistical and systematic) combined in quadrature.

P_T^X (GeV)	Data	SM Expectation	Signal	Other SM processes
12 - 25	2	1.17 $\pm$ 0.19	0.99 $\pm$ 0.18	0.18 $\pm$ 0.06
25 - 40	3	0.83 $\pm$ 0.14	0.72 $\pm$ 0.14	0.11 $\pm$ 0.03
> 40	3	0.55 $\pm$ 0.13	0.50 $\pm$ 0.13	0.05 $\pm$ 0.02
Total	8	2.56 $\pm$ 0.42	2.21 $\pm$ 0.41	0.35 $\pm$ 0.09
< 25	2	1.17 $\pm$ 0.19	0.99 $\pm$ 0.18	0.18 $\pm$ 0.06
> 25	6	1.38 $\pm$ 0.27	1.12 $\pm$ 0.26	0.17 $\pm$ 0.04

Table 9.4: Observed and predicted event rates in the final muon selection in bins of P_T^X for the complete HERA I e^+p H1 data set. Presented are the observed data events, the total expectation from all SM processes, and the prediction from the signal and background components. Also given are the total errors (statistical and systematic) combined in quadrature.

9.2.3 Combined Final Selections

The two final selections are combined to form a final event sample[2], the results of which are presented in table 9.5. Shown are the data results, the combined prediction from all SM processes and the expectation from signal and background processes as a function of P_T^X. Only the electron channel contributes for $P_T^X < 12$ GeV. The total number of observed data events exceeds the total prediction from all SM processes: 18 data events are observed compared to a SM prediction of 12.43 ± 1.59. At $P_T^X < 25$ GeV, 8 events are observed, in good agreement with the total SM prediction of 9.54 ± 1.21. However, at $P_T^X > 25$ GeV, 10 data events are observed compared to a total SM prediction of 2.89 ± 0.51.

P_T^X (GeV)	Data	SM Expectation	Signal	Other SM processes
< 12	5	6.66 ± 0.87	4.45 ± 0.71	2.21 ± 0.50
12 - 25	3	2.88 ± 0.39	2.30 ± 0.37	0.57 ± 0.13
25 - 40	4	1.78 ± 0.28	1.51 ± 0.27	0.27 ± 0.07
> 40	6	1.11 ± 0.25	0.98 ± 0.25	0.14 ± 0.05
Total	18	12.43 ± 1.59	9.24 ± 1.45	3.19 ± 0.63
< 25	8	9.54 ± 1.21	6.76 ± 1.07	2.78 ± 0.58
> 25	10	2.89 ± 0.51	2.49 ± 0.51	0.40 ± 0.10

Table 9.5: Observed and predicted event rates in the combined (electron and muon) final selection in bins of P_T^X for the complete HERA I e^+p H1 data set. Presented are the observed data events, the total expectation from all SM processes, and the prediction from the signal and background components. Also given are the total errors (statistical and systematic) combined in quadrature.

[2] The two selections are exclusive due to the requirement of no isolated muons in the final electron sample (see section 8.1).

Appendix A contains event displays of all 18 data events in the final selection. The main kinematic quantities of each event are listed in table B.1. The distributions of θ_l and $\Delta\phi_{l-X}$ in the combined final selection are shown in figure 9.3. The data are found at mainly at low values of θ_l and exhibit a flat distribution in $\Delta\phi_{l-X}$, both consistent with the expectation. Figure 9.4a shows the P_T^X distribution of the selected events. At low P_T^X the data are in agreement the SM prediction, whereas at high P_T^X the data lie above the SM prediction. The transverse mass distribution of the selected events is displayed in figure 9.4b and is compatible with the Jacobian peak expected from W production. The results of the final event selection are discussed in section 9.4.

9.3 Cross Section

A measured cross section for signal processes (see section 3.4) is obtained by correcting the number of observed data events for the acceptance of the detector. Isolated electrons or muons produced in leptonic tau decays may also contribute to this measurement, as described in section 3.4.3. The cross section is measured in the kinematical region defined in table 9.6, at an effective centre of mass energy of $\sqrt{\mathrm{s}} =$ 312 GeV. This value assumes a linear dependence of the cross section on the proton beam energy and is calculated by combining the two e^+p data samples (see chapter 6) used in this analysis according to their respective luminosities.

The detector acceptance, A for a given bin is calculated using EPVEC and is defined as

$$A = \frac{\mathrm{N_{rec}}}{\mathrm{N_{gen}}} \tag{9.1}$$

where $\mathrm{N_{rec}}$ is the number of events reconstructed in the bin after the final event selection and $\mathrm{N_{gen}}$ is the number of events generated in the bin the region of phase

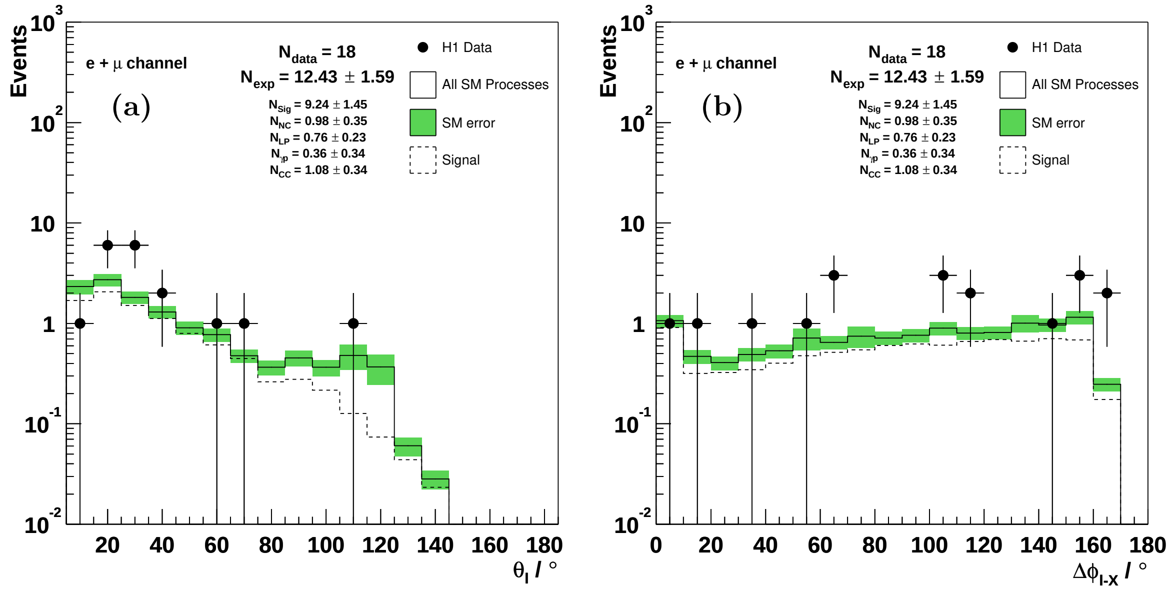

Figure 9.3: The θ_l (a) and $\Delta\phi_{l-X}$ (b) distributions of the combined final selections.

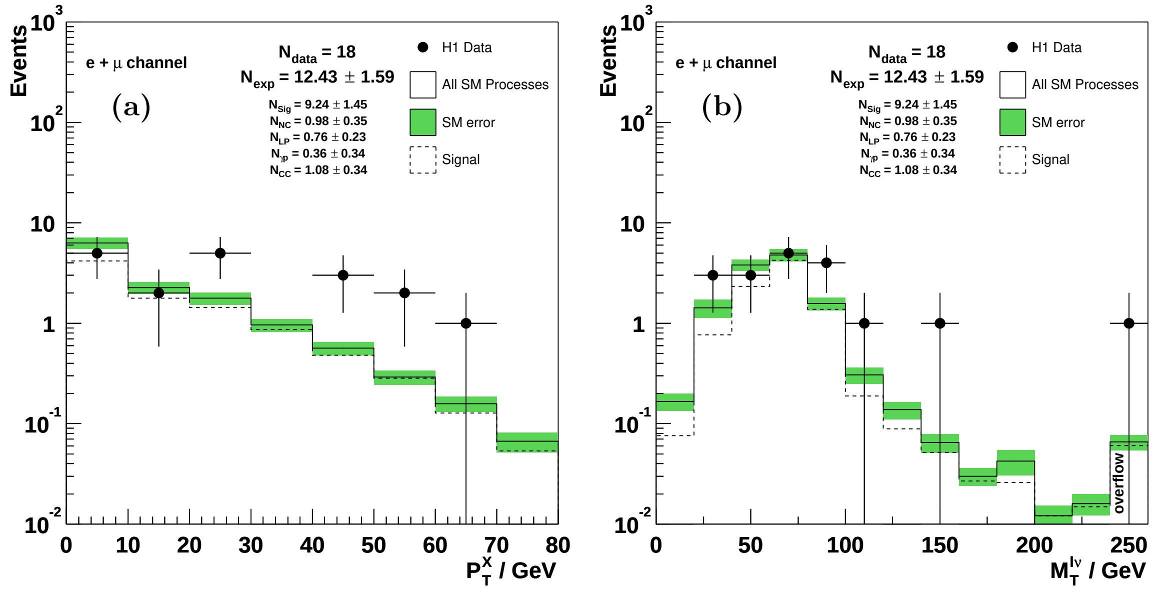

Figure 9.4: The P_T^X (a) and $M_T^{l\nu}$ (b) distributions of the combined final selections.

space defined in table 9.6.

The cross section is defined as

$$\sigma = \frac{(\mathrm{N_{obs}} - \mathrm{N_{bg}})}{\mathcal{L}A} \tag{9.2}$$

where $\mathrm{N_{obs}}$ is the number of observed data events, $\mathrm{N_{bg}}$ is the expectation from background processes, $\mathcal{L}$ is the integrated luminosity of the data sample and A is the detector acceptance, calculated as described above.

Variable	Cut
P_T^l	> 10 GeV
θ_l	$5^\circ < \theta_l < 140^\circ$
P_T^{miss}	> 12 GeV
D_{jet}	> 1.0

Table 9.6: The generator level selection, defining the kinematical region of the measured cross section.

The cross section for events with isolated electrons or muons and missing transverse momentum is measured in the kinematic region defined in table 9.6. The measured cross section is presented in table 9.7 for $P_T^X < 25$ GeV, $P_T^X > 25$ GeV and integrated over all P_T^X, with the associated statistical and systematic errors.

The total systematic error on the cross section is formed by combining the experimental uncertainties described in section 9.1 in quadrature with the total background error and a 10% uncertainty on the model dependence of the acceptance. The model uncertainty is estimated by comparing the acceptance obtained using EPVEC with two further generators which produce W bosons [116]. A full breakdown of the errors on the measured cross section is given in table B.2.

Table 9.7 also shows the signal expectation from the Standard Model, calculated for all signal processes described in section 3.4. The dominant $ep \to eWX$ contribution is calculated at NLO as described in section 3.4.2. Integrated over all P_T^X the measured cross section is compatible with the SM prediction and for $P_T^X < 25$ GeV the cross sections agree within the stated errors. However, for $P_T^X > 25$ GeV the measured cross section exceeds the expectation.

P_T^X	Cross Section (pb)	
(GeV)	Measured	SM NLO
< 25	$0.141 \pm 0.082 \pm 0.028$	0.194 ± 0.029
> 25	$0.166 \pm 0.055 \pm 0.028$	0.044 ± 0.007
Total	$0.308 \pm 0.098 \pm 0.041$	0.237 ± 0.036

Table 9.7: The measured cross section for signal events, calculated in the kinematical region defined in table 9.6 and at $\sqrt{s} = 312$ GeV. The first error is statistical and the second is systematic. Also shown is the signal expectation from the Standard Model and the associated total error, where the dominant $ep \to eWX$ contribution is calculated at NLO.

9.4 Discussion

Introduction

The analysis presented in this thesis is the extension of several previous H1 analyses concerning events containing isolated, high P_T leptons and missing transverse momentum. Since the observation of the first event published in [1], the H1 events with isolated leptons and missing transverse momemtum have been of great interest. Six such events were discovered in the 94-97 e^+p data taking period, 5 events containing a muon and 1 event containing an electron, compared to a SM prediction of 3.2 ± 0.6 [2]. The excess observed in the 94-97 e^+p data is also present in the 99-00 e^+p data.

The analyses presented in [3, 4] examined these events in the context of SM W production. The current analysis has a broader focus including all SM processes producing isolated charged leptons and missing transverse momentum, as described in section 3.4. The event selections performed have also been improved with respect to the selection described in [3], through simplifying the cuts and with the introduction of the basic phase space definition described in section 6.3. More detailed studies, each an extension of the basic phase space selection, have been performed on the major SM background processes in the final event selections.

Furthermore, the analysis now includes the full HERA I e^+p data sample. The results presented in this thesis have provided an important cross-check to those recently published in [116]. A comparison of the two sets of results is presented in appendix C.

A new NLO calculation of the W production cross section at HERA has been performed, as described in section 3.4.2. This has reduced the theoretical systematic error on the signal component of the total SM prediction to 15% from 30% at LO, improving the precision of the presented signal expectation. The evaluation of experimental systematics using the signal prediction has also been included in the analysis for the first time, as described in section 9.1.

The Presented Results

In the early HERA I data the final event sample was dominated by muon events [2], whereas the current final event sample exhibits a more balanced distribution with 5 electron events and 8 muon events at $P_T^X > 12$ GeV. At $P_T^X < 12$ GeV, 3 of the 5 electron events are new to the analysis. The data are found to be in agreement with the SM prediction at low P_T^X in all final selections. In the combined final selection 8 data events are observed at $P_T^X < 25$ GeV in good agreement with the total SM prediction of 9.54 $\pm$ 1.21 (6.76 $\pm$ 1.07 from signal processes).

An excess of data events remains with the inclusion of the data since the results published in [3, 4], with 2 further events at $P_T^X > 25$ GeV; 1 electron event and 1 muon event. The high P_T^X muon event discussed in [1] and included in previous publications is no longer present in the final event selection, due to the change in the acoplanarity cut in the final muon selection. Furthermore, the data presented in this thesis have been *reprocessed*: a technique employed to include the latest calibrations at DST level (see section 2.8). As a result of this reprocessing, one electron event has migrated into the highest bin in P_T^X. In the combined final selection 10 data events are observed at $P_T^X > 25$ GeV compared with a total SM prediction of 2.89 $\pm$ 0.51 (2.49 $\pm$ 0.51 from signal processes). At $P_T^X > 40$ GeV 6 data events are observed, compared to a total SM prediction of 1.11 $\pm$ 0.25 (0.98 $\pm$ 0.25 from signal processes).

With the accumulation of greater statistics a cross section measurement for events containing isolated charged leptons and missing transverse momentum has been made possible, as described in section 9.3. The measured cross section is found to be in agreement with the prediction from signal processes for events at $P_T^X <$

25 GeV. However, at $P_T^X > 25$ GeV the prediction from signal processes underestimates the observed cross section. This result reflects the excess observed in the data over the expectation, where the dominant contribution to the total SM prediction at high P_T^X is due to signal processes.

Systematic and Statistical Errors

The systematic uncertainty on the prediction from signal processes consists of two parts: experimental and theoretical, as described in section 9.1. The experimental systematics included are based on studies performed in other H1 analyses, with refinements appropriate to the final state topology examined. The NLO theoretical error of 15% remains the dominant contribution to the total systematic error on the signal expectation.

The systematic uncertainties on background processes are evaluated using the background study samples as described in chapter 7. In the final electron selection the dominant sources of background are due to NC and CC events and dedicated studies on these processes are presented in section 7.1 and 7.2 respectively. In the final muon selection the dominant sources of background are due to lepton pair and CC events and dedicated studies on these processes are presented in section 7.3 and 7.4 respectively. Examination of the kinematic distributions in each of the background study samples shows that the level of agreement between data and simulation is within the 30% systematic error attributed to the major background processes. The contribution of photoproduction events to the final selection, which are assigned a systematic of 75%, is minimal.

In the high P_T^X region of the individual and combined final selections the total SM prediction is very low compared to the data. The data lie well beyond the extent of the systematic errors attributed to the simulation. The excess of data events at high P_T^X may be interpreted as a statistical fluctuation, although the continued observation of new events in this region of phase space further reduces the likelihood of this interpretation.

Numerically, the probability (calculated using Poisson statistics) of the SM expectation measured by this analysis to fluctuate up to or beyond the observed number of events across all P_T^X is 0.10. For $P_T^X > 25$ GeV and $P_T^X > 40$ GeV this probability decreases to 0.0015. These probabilities include the total uncertainty (statistical and systematic) on the SM prediction. The calculation of these probabilities is outlined in appendix D.

Comparison to ZEUS

A similar analysis has been performed by the ZEUS collaboration [117–119]. In particular, recent results published by ZEUS on the full HERA I data sample have reported no excess of data events at high P_T^X [119]. In particular, at $P_T^X > 25$ GeV 7 data events are observed compared to 5.65 predicted by the SM (2.68 from W production) and at $P_T^X > 40$ GeV no data events are observed compared to 1.89 predicted by the SM (1.15 from W production). The predicted rate from signal processes at high P_T^X in the ZEUS analysis is similar to the results presented in this thesis, but the background contribution to the total SM prediction is much larger. In particular, at $P_T^X > 25$ GeV background processes account for $\approx 53\%$ of the total SM prediction, compared to 14% in this analysis (see table 9.5). H1 has also repeated its analysis in the more limited angular range of the ZEUS experiment [4]. This reduces the total SM expectation by 20–25%, but the ratio of the signal to background prediction remains approximately constant.

In order to investigate the observed differences in the H1 and ZEUS analyses a comparison has been made of the track finding efficiency of each experiment using a W production Monte Carlo [120]. The study, which concentrated on high P_T muon events, reports that although the ZEUS efficiency is lower than H1 at very low polar angles the two are comparable at $\theta_{track} > 25°$. Crucially, this is the region where the high P_T^X H1 events are found and the report concluded that it was likely that such events would have also been found by ZEUS [120]. Table B.1 shows that 9 of the 10 events at $P_T^X > 25$ GeV in the results presented here are in this angular range. Clearly, more detailed comparisons are required to investigate all facets of each analysis to determine a possible source of the observed discrepency in the results of each experiment.

Possible BSM Interpretations

Several publications [67–72, 77, 78] have discussed the excess of data events at high P_T^X as a potential signature of new physics beyond the Standard Model.

Leptoquark production with lepton flavour violation may produce a final state containing high P_T muons and a jet, similar to the final state of the observed events at high P_T^X. However, the leptoquark final state contains no intrinsic P_T^{miss} and has an approximate back-to-back configuration in the $x - y$ plane, making this process an unlikely explanation for the source of the observed excess. Furthermore, in a dedicated search for leptoquark production at H1 no event candidate was found compatible with leptoquark kinematics [67].

A search for excited fermions has been performed by H1 [70], a process where a fermion participating in the interaction is excited into a higher energy state by the scattering process. This excited state may then decay via the production of a real W boson, providing a similar final state to the signal processes examined here. However, the search described in [70] found no evidence of the production of such particles.

Several other searches for particles based on the Minimal Supersymmetric Standard Model (MSSM) have been undertaken by H1 [71, 72] and such decays may mimic the signal topology of this analysis. In particular, the production of squarks with subsequent R_p violating and conserving decays has been investigated in [71], which reported no significant deviation from the Standard Model.

A further hypothesis for the origin of the observed excess is single top production via Flavour Changing Neutral Current interactions as described in section 3.5.2. Previous work [3] has cited this explanation as the most compatible of the possible BSM interpretations.

Single Top Production

The single top hypothesis may be examined by reconstructing the invariant masses of the final state of the events in the final selection, following the method described in section 6.3.9. The scattered electron is detected in 2 events, enabling the calculation of the invariant masses $M^{l\nu}$ and $M^{l\nu X}$. Such events are termed *tagged* events in the following. The kinematic properties of the scattered electron and the values of the reconstructed masses of the two events are presented in table 9.8.

Run Event		P_T^{scat} (GeV)	θ_{scat} (°)	ϕ_{scat} (°)	$M^{l\nu}$ (GeV)	$M^{l\nu X}$ (GeV)
188108 5066	μ^-	$6.7^{+0.5}_{-0.5}$	$118.05^{+0.25}_{-0.25}$	$138.20^{+0.30}_{-0.30}$	$86.6^{+8.7}_{-6.8}$	$160.2^{+7.0}_{-6.2}$
196406 38438	e	$0.8^{+0.05}_{-0.05}$	$176.14^{+0.25}_{-0.25}$	$-6.58^{+0.30}_{-0.30}$	$74.7^{+2.8}_{-2.8}$	$100.2^{+3.4}_{-3.4}$

Table 9.8: The kinematic properties of the scattered electron and the reconstructed invariant masses of the two tagged events in the final selection.

In the remaining 16 events no scattered electron is observed in the detector. These events are termed *untagged* events and the invariant masses of the final state are calculated as M^{lmiss} and M^{lmissX}. The effect of the uncertainty on the scattered electron energy, E_{scat}, in the calculation of M^{lmiss} is investigated using the following procedure: The scattered electron in each of the untagged events is assumed to carry half of the missing $E - P_z$ in the event ($\frac{\delta_{miss}}{2}$); the remainder is attributed to the neutrino. The variation in the value of M^{lmiss} is then calculated for a given variation in the scattered electron energy using the following relationship

$$\delta M^{l\,miss} = \frac{1}{2M^{l\,miss}} \left| \frac{\partial M^{l\,miss^2}}{\partial E_{scat}} \right| \delta E_{scat} \tag{9.3}$$

where

$$\frac{\partial M^{l\,miss^2}}{\partial E_{scat}} = 2E_l \, \frac{P_T^{miss^2}}{\delta_{miss}{}^2} \, (1 - \cos\theta_l) - 2E_l \, (1 + \cos\theta_l) \tag{9.4}$$

For a variation of 50% in the scattered electron energy the variation in M^{lmiss} is typically around 10%, demonstrating the relative insensitivity of this quantity to the scattered electron energy. The same level of variation is expected in M^{lmissX} as the hadronic system has no dependence on the scattered electron.

The distributions of M^{lV} and M^{lVX} in the combined final selections are displayed in figure 9.5, where $V \equiv \nu$ in tagged events and $V \equiv miss$ in untagged events. It should be noted that the typical variation of the invariant masses described above is less than the bin width of each distribution for all masses below 200 GeV.

The M^{lV} distribution in the combined final event selection is displayed in figure 9.5(a). The data and SM prediction follow a broad peak around the nominal W boson mass, with the untagged events introducing a visible smearing to higher values of M^{lV}. Figure 9.5(b) shows the M^{lVX} distribution in the combined final event selection. The SM prediction exhibits a broad peak around 100 GeV. However, the data are clearly found towards higher values of M^{lVX}.

The final selection presented in this thesis is extended in a dedicated H1 single top search [78], where the signal component of the total SM prediction in this analysis forms the dominant background process. The single top signal is selected by the additional requirements that the charge of the isolated lepton is positive, $P_T^X > 30$ GeV and $M^{lVX} > 140$ GeV. A positively charged lepton is expected in leading order FCNC single top production (see section 3.5.2). For untagged events

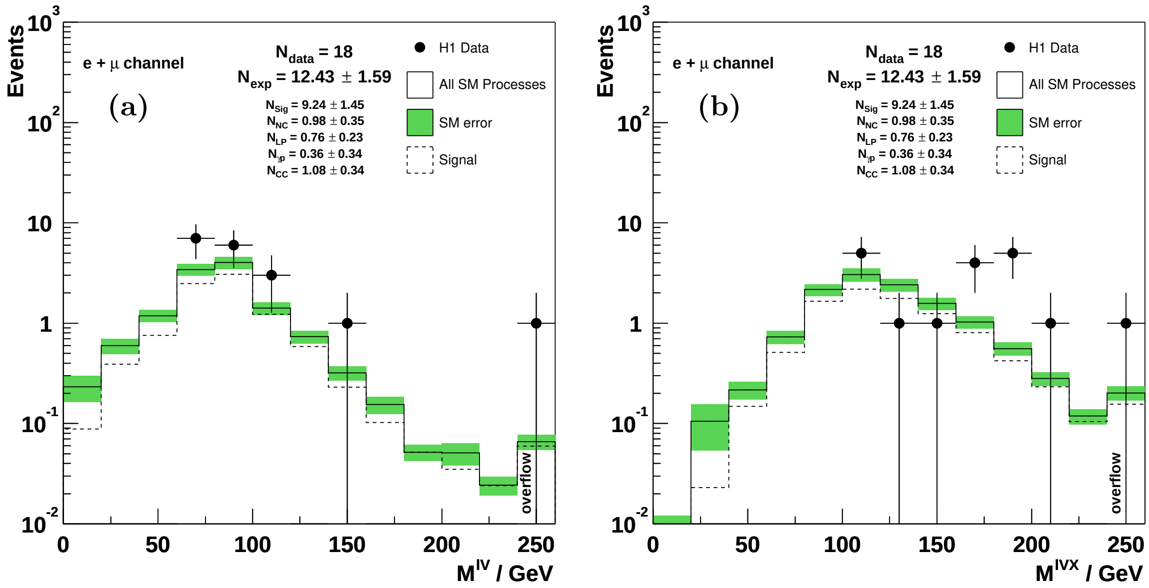

Figure 9.5: The M^{lV} (a) and M^{lVX} (b) distributions of the combined final selections.

the invariant mass reconstruction is performed by constraining the lepton-neutrino mass to that of the W boson. The invariant masses of the tagged events are reconstructed identically to the method presented here. The single top analysis reports 5 events compatible with single top production compared to a SM prediction from background processes of 1.31 $\pm$ 0.22. These 5 events appear in the range 140 $< M^{lVX} <$ 220 GeV in figure 9.5(b). The analysis reported in [78] also shows the correlation between M_T^{lV} and M^{lVX} and finds several events compatible with single top production.

Chapter 10

Summary

A total of 18 events containing an isolated electron or muon with missing transverse momentum are observed in the 104.7 pb^{-1} comprising the complete HERA I e^+p data set. The prediction from all SM processes is 12.43 ± 1.59, of which 9.24 ± 1.45 are due to signal processes. The signal expectation is dominated by W production with subsequent leptonic decay.

At low P_T^X the number of observed events is in agreement with the SM expectation. At $P_T^X > 25$ GeV, 10 events are observed compared to an SM expectation of 2.89 ± 0.51, of which 2.49 ± 0.51 are due to signal processes. The cross section for all processes producing isolated electrons or muons and missing transverse momentum is measured as $0.308 \pm 0.098 \pm 0.041$ pb in the kinematic region studied.

A possible explanation of the excess of events observed at high P_T^X is the production of single top quarks via the FCNC interaction. Of the BSM hypotheses relevant to this analysis, this process is the most compatible interpretation, given the event kinematics.

The HERA accelerator is currently undergoing an extensive luminosity upgrade. The H1 and ZEUS experiments are also upgrading to benefit from the tenfold increase in data expected from the HERA II programme. In terms of this analysis, the higher statistics provided by the upgrade will provide greater insight into the origin of the events presented in this thesis.

Bibliography

[1] H1 Collaboration; T. Ahmed *et al.*, *Observation of an $e^+p \rightarrow \mu^+X$ Event with High Transverse Momenta at HERA*, DESY Report, **DESY-94-248**.

[2] H1 Collaboration; C. Adloff *et al.*, *Observation of Events with an Isolated High Energy Lepton and Missing Transverse Momentum at HERA*, Eur. Phys. J. **C5** (1998) 575.

[3] N. Malden, *W Production in ep Collisions*, Ph.D. Thesis, University of Manchester (2000).

[4] H1 Collaboration, *W Production in ep Collisions at HERA*, contributed paper to *The 30th International Conference on High–Energy Physics, Osaka 2000*, **Abstract 974**.

[5] H1 Collaboration; I. Abt *et al.*, *The H1 Detector at HERA*, NIM, **A386** (1997) 310 and 348.

[6] R. K. Bock and A. Vasilescu, *The Particle Detector Briefbook*, Springer (1998).

[7] J. Burger *et al.*, *The Central Jet Chamber of the H1 Experiment*, NIM, **A279** (1989) 217.

[8] S. Egli *et al.*, *The Central–Inner Z–Drift Chamber of the H1 Experiment*, NIM, **A283** (1989) 487.

[9] K. Müller *et al.*, *Construction and Performance of a Thin Cylindrical Multiwire Proportional Chamber with Cathode Pad Readout for the H1 Experiment*, NIM, **A312** (1992) 457.

[10] S. Burke *et al.*, *Track Finding and Fitting in the H1 Forward Track Detector*, DESY Report, **DESY-95-132**.

[11] H1 Collaboration; I. Abt *et al.*, *Technical Proposal for the Upgrade of the Backward Region of the H1 Detector*, DESY Internal Report, **PRC-93-02**.

[12] D. Perkins, *Introduction to High Energy Physics*, Addison–Wesley (1987).

[13] H1 Calorimeter Group; B. Andrieu *et al.*, *The H1 Liquid Argon Calorimeter System*, NIM, **A336** (1993) 460.

[14] H. Wellisch *et al.*, *Hadronic Calibration of the H1 LAr Calorimeter using Software Weighting Techniques*, H1 Internal Note, **H1-IN-346 (02/1994)**.

[15] H1 Calorimeter Group; B. Andrieu *et al.*, *Beam Tests and Calibration of the H1 Liquid Argon Calorimeter with Electrons*, NIM, **A350** (1994) 57.

[16] H1 Calorimeter Group; B. Andrieu *et al.*, *Results from Pion Calibration Runs for the H1 Liquid Argon Calorimeter and Comparisons with Simulations*, NIM, **A336** (1993) 499.

[17] H1 SpaCal Group; R. D. Appuhn *et al.*, *The H1 Lead/Scintillating–fibre Calorimeter*, NIM, **A386** (1997) 397.

[18] H1 SpaCal Group; T. Nicholls *et al.*, *Performance of an Electromagnetic Lead/Scintillating–fibre Calorimeter for the H1 Detector*, NIM, **A374** (1996) 149.

[19] H1 SpaCal Group; R. D. Appuhn *et al.*, *H1 Backward Upgrade with a SPACAL Calorimeter: The Hadronic Section*, DESY Report, **DESY-96-013**.

[20] H1 SpaCal Group; R. D. Appuhn *et al.*, *Hadronic Response and e/π–Separation with the H1 Lead/Fiber Calorimeter*, NIM, **A382** (1996) 395.

[21] W. Hildesheim *et al.*, *The Plug Calorimeter Users Guide*, H1 Internal Note, **H1-IN-372 (08/1994)**.

[22] J. Ebert, *The H1–Tail Catcher Hardware and Software Performance*, H1 Internal Note, **H1-IN-448 (08/1995)**.

[23] H. Itterbeck *et al.*, *Improvement of the Trigger Timing of the H1 Digital Muon System*, H1 Internal Note, **H1-IN-427 (02/1995)**.

[24] H1 Collaboration; T. Ahmed *et al.*, *The H1 Forward Muon Spectrometer*, NIM, **A340** (1994) 304.

[25] J. Heatherington *et al.*, *Studies on TOF FTDC Data*, H1 Internal Note, **H1-IN-307 (08/1993)**;
J. Heatherington *et al.*, *Analysis of TOF FTDC Data*, H1 Internal Note, **H1-IN-362 (06/1994)**.

[26] H1 Collaboration, *Luminosity Measurement in the H1 Experiment at HERA*, contributed paper to *ICHEP96, Warsaw 1996*, **ICHEP96pa17-026**.

[27] H. Bethe and W. Heitler, *On the Stopping of Fast Particles and on the Creation of Positive Electrons*, Proc. Roy. Soc. Lond. **A146** (1934) 83.

[28] E. Elsen, *The H1 Trigger and Data Acquisition*, contributed paper to *International Symposium on Electronic Instrumentation in Physics, Dubna 1991*, H1 Internal Note, **H1-IN-262 (01/1993)**;
F. Sefkow *et al.*, *Experience with the First Level trigger of H1*, contributed paper to *The 1994 IEEE Nuclear Science Symposium, Virginia 1994*, H1 Internal Note, **H1-IN-407 (11/1994)**.

[29] J. C. Bizot *et al.*, *Status of Simulation for a Topological Level 2 Trigger*, H1 Internal Note, **H1-IN-212 (02/1992)**;
J. C. Bizot *et al.*, *Strategy Studies for the H1 Topological L2–Trigger (L2TT)*, H1 Internal Note, **H1-IN-508 (01/1997)**.

[30] J. H. Köhne *et al.*, *Realization of a Second Level Neural Network Trigger for the H1 experiment at HERA*, H1 Internal Note, **H1-IN-509 (01/1997)**.

[31] H1 Collaboration, *A Fast Track Trigger with High Resolution for H1*, DESY Internal Report, **PRC-99-06**.

[32] H1 Collaboration, *ep Physics Beyond 1999*, H1 Internal Note, **H1-IN-531 (10/1997)**.

[33] H1 Collaboration; S. Aid *et al.*, *H1REC – H1 Reconstruction Program*, H1 Internal Report (1995).

[34] R. Y. Rubinstein, *Simulation and the Monte Carlo Method*, Wiley (1981).

[35] H1 Collaboration; S. Aid *et al.*, *Guide to Simulation Program, H1SIM*, H1 Internal Report (1995).

[36] R. Brun *et al.*, *GEANT3 User's Guide*, **CERN-DD/EE-84-1**.

[37] R. Marshall, Handbook to *High Energy ep Physics*, A postgraduate lecture course given in the Department of Physics and Astronomy at The University of Manchester (2000).

[38] J. D. Bjorken and E. Paschos, *Inelastic Electron–Proton and γ–Proton Scattering and the Structure of the Nucleon*, Phys. Rev. **185** (1969) 1975.

[39] R. Feynman, *Very High Energy Collisions of Hadrons*, Phys. Rev. Lett. **23** (1969) 1415.

[40] H1 Collaboration; C. Adloff *et al.*, *Measurement of Di–jet Cross–Sections in Photoproduction and Photon Structure*, Phys. Lett. **B483** (2000) 36.

[41] B. Heinemann, *Measurement of Charged Current and Neutral Current Cross Sections in Positron–Proton Collisions at* $\sqrt{s} \simeq 300 GeV$, Dissertation, Fachbereich Physik der Universität Hamburg (1999).

[42] G. P. Zeller *et al.*, *A Precise Determination of Electroweak Parameters in Neutrino–Nucleon Scattering*, Phys. Rev. Lett. **88** (2002) No. 9.

[43] H1 Collaboration; V. Andreev *et al.*, *Measurement and QCD Analysis of Inclusive Deep Inelastic Scattering at High* Q^2 *and Large* x, submitted to Eur. Phys. J. **C**.

[44] BCDMS Collaboration; A. C. Benevenuti *et al.*, *Test of QCD and a Measurement of* λ *from Scaling Violations in the Proton Structure Function* $F_2(x, Q^2)$ *at High* Q^2, Phys. Lett. **B223** (1989) 485.

[45] NMC Collaboration; P. Amaudruz *et al.*, *Proton and Deuteron* F_2 *Structure Functions in Deep Inelastic Muon Scattering*, Phys. Lett. **B295** (1992) 159; NMC Collaboration; M. Arneodo *et al.*, *Measurement of the Proton and the Deuteron Structure Functions,* F_2^p *and* F_2^d, Phys. Lett. **B364** (1995) 107.

[46] J. D. Bjorken, *Inequality for Backward Electron–Nucleon and Muon–Nucleon Scattering at High Momentum Transfer*, Phys. Rev. **163** (1967) 1767.

[47] H1 Collaboration; S. Aid *et al.*, *A Direct Determination of the Gluon Density in the Proton at Low* x, Nucl. Phys. **B449** (1995) 3.

[48] G. Altarelli and G. Parisi, *Asymptotic Freedom in Parton Language*, Nucl. Phys. **B126** (1977) 298.

[49] Y. L. Dokshitzer, *Calculation of the Structure Functions for Deep Inelastic Scattering and* e^+ *and* e^- *Annihilation by Perturbation Theory in Quantum*

Chromodynamics, Sov. Phys. JETP **46** (1977) 641;
V. N. Gribov and L. N. Lipatov, *Deep Inelastic ep Scattering in Perturbation Theory*, Sov. J. Nucl. Phys. **15** (1972) 438 and 675.

[50] E. A. Kuraev, L. N. Lipatov and V. S. Fadin, *The Pomeranchuk Singularity in Non–Abelian Gauge Theories*, Sov. Phys. JETP **45** (1977) 199;
I. I. Balitsky and L. N. Lipatov, *The Pomeranchuk Singularity in Quantum Chromodynamics*, Sov. J. Nucl. Phys. **28** (1978) 822.

[51] H1 Collaboration; S. Aid *et al.*, *The Gluon Density of the Proton at Low x from a QCD Analysis of F_2*, Phys. Lett. **B354** (1995) 494.

[52] M. E. Peskin and D. V. Schroeder, *An Introduction to Quantum Field Theory*, Addison–Wesley (1995).

[53] E. Gabrielli, *The Production of Weak Intermediate Bosons in ep Reactions*, Mod. Phys. Lett. **A1** (1986) 465.

[54] U. Baur, J. A. M. Vermaseren and D. Zeppenfeld, *Electroweak Vector Boson Production in High Energy ep Collisions*, Nucl. Phys. **B375** (1992) 3.

[55] C. Diaconu *et al.*, *H1EPVEC – $W^{\pm}$ and Z Production Monte Carlo Generator Based on EPVEC*, CPPM Marseille (1999).

[56] K. P. O. Diener, C. Schwanenberger and M. Spira, *Photoproduction of W Bosons at HERA: Reweighting Method for Implementing QCD Corrections in Monte Carlo Programs*, **hep-ex/0302040**;
K. P. O. Diener, C. Schwanenberger and M. Spira, *Photoproduction of W Bosons at HERA: QCD Corrections*, Eur. Phys. J. **C25** (2002) 405;
P. Nason, R. Rückl and M. Spira, *A Note on W Boson Production at HERA*, J. Phys. **G25** (1999) 1434;
M. Spira, *W Boson Production at NLO*, contributed paper to *Workshop*

on Monte Carlo Generators for HERA Physics, Hamburg 1998, **hep-ph/9905469**.

[57] U. Baur and D. Zeppenfeld, *Measuring the $WW\gamma$ Vertex in Single W Production at ep Colliders*, Nucl. Phys. **B325** (1989) 253.

[58] C. F. von Weizsäcker, *Radiation Emitted in Collisions of Very Fast Electrons*, Zeit. für Physik, **88** (1934) 612;
E. J. Williams, *Nature of the High Energy Particles of Penetrating Radiation and Status of Ionization and Radiation Formulae*, Phys. Review, **45** (1934) 729.

[59] S. D. Drell and T. Yan, *Massive Lepton–Pair Production in Hadron–Hadron Collisions at High Energies*, Phys. Rev. Lett. **25** (1970) 316.

[60] T. Sjöstrand, *High Energy Event Generation with PYTHIA 5.7 and JETSET 7.4*, Comput. Phys. Commun. **82** (1994) 74.

[61] P. Aurenche *et al.*, *Higher Order QCD Corrections to the Photoproduction of a Direct Photon at HERA*, Z. Phys. **C56** (1992) 589.

[62] H. L. Lai *et al.*, *Improved Parton Distributions from Global Analysis of Recent Deep Inelastic Scattering and Inclusive Jet Data*, Phys. Rev. **D55** (1997) 1280.

[63] H1 Collaboration; C. Adloff *et al.*, *W Production in $e^{\pm}p$ Collisions at HERA*, document prepared for *The 19th International Symposium on Lepton and Photon Interactions at High Energies, Stanford 1999.*

[64] G. Frising, *Rare Phenomenon and W Production in Electron Proton Scattering at HERA*, Ph.D. Thesis, RWTH Aachen (in preparation).

[65] D. Waters, *A First Estimate of $\sigma(e^+p \rightarrow e^+W^{\pm}X)$ and Studies of High P_T Leptons with the ZEUS Detector at HERA*, Ph.D. Thesis, University of Oxford (1998).

[66] N. Artega–Romero, C. Carimalo and P. Kessler, *High P_T Lepton Pair Production at ep Colliders: Comparison Between Various Production Mechanisms*, Z. Physics, **C52** (1991) 289.

[67] R. Kerger, *Lepton Flavor Violation at HERA*, contributed paper to *The 8th International Workshop on Deep Inelastic Scattering and QCD, Liverpool 2000*, **hep-ex/0006023**;
H1 Collaboration; C. Adloff *et al.*, *A Search for Leptoquark Bosons and Lepton Flavor Violation in Positron–Proton Collisions at HERA*, Eur. Phys. J. **C11** (1999) 447.

[68] H1 Collaboration, *A Search for Leptoquark Bosons in ep Collisions at HERA*, contributed paper to *The 31st International Conference on High–Energy Physics, Amsterdam 2002*, **Abstract 1027**.

[69] K. Hagiwara, D. Zeppenfeld and S. Komamiya, *Excited Lepton Production at LEP and HERA*, Z. Phys. **C29** (1985) 115.

[70] H1 Collaboration; C. Adloff *et al.*, *A Search for Excited Fermions at HERA*, Eur. Phys. J. **C17** (2000) 567.

[71] H1 Collaboration; C. Adloff *et al.*, *Searches at HERA for Squarks in R–Parity Violating Supersymmetry*, Eur. Phys. J. **C20** (2001) 639;
T. Kon *et al.*, *Single sbottom/scharm Production at HERA in an R–parity Breaking SuperSymmetric Model*, Phys. Lett. **B494** (2000) 280.

[72] T. Kon, T. Kobayashi and S. Kitamura, *Is the High P_T Muon of the $e^+p \to \mu^+X$ Event Observed at HERA a Signature of the Stop?*, Phys. Lett. **B376** (1996) 227.

[73] K. Hagiwara *et al.*, *Probing the Weak Boson Sector in $e^+e^- \to W^+W^-$*, Nucl. Phys. **B282** (1987) 253.

[74] K. J. F. Gaemers and G. J. Gouraris, *Polarisation Amplitudes for $e^+e^- \rightarrow W^+W^-$ and $e^+e^- \rightarrow ZZ$*, Z. Physics **C1** (1979) 259.

[75] The LEP Collaborations ALEPH, DELPHI, L3, OPAL and the LEP TGC Working Group, *A Combination of Preliminary Results on Gauge Boson Couplings Measured by the LEP Experiments*, contributed paper to Summer 2002 Conferences, **LEPEWWG/TGC/2002-02, ALEPH 2002-036 PHYSIC 2002-012, DELPHI 2002-094 PHYS 924, L3 Note 2779, OPAL TN728**.

[76] L. Wolfenstein, *Parameterization of the Kobayashi–Maskawa Matrix*, Phys. Rev. Lett. **51** (1983) 1945.

[77] G. M. de Divitiis, R. Petronzio and L. Silvestrini, *Flavor Changing Top Decays in Supersymmetric Extensions of the Standard Model*, Nucl. Phys. **B504** (1997) 45;
H. Fritzsch and D. Holtmannspötter, *The Production of Single t Quarks at LEP and HERA*, Phys. Lett. **B457** (1999) 186.

[78] H1 Collaboration; V. Andreev *et al.*, *Search for Single Top Quark Production in $e^{\pm}p$ Collisions at HERA*, (in preparation);
J. Kennedy, *A Search for Single Top-Quark Production and Flavour–Changing Neutral Current Interactions at H1*, Ph.D. Thesis, Liverpool University (2002);
H1 Collaboration, *Search for Single Top Production in ep Collisions at HERA*, contributed paper to *International Europhysics Conference on High Energy Physics, EPS2001, Budapest 2001*, **Abstract 824**.

[79] CDF Collaboration; F. Abe *et al.*, *Search for Flavor Changing Neutral Current Decays of the Top Quark in $p\bar{p}$ Collisions at $\sqrt{s}$ = 1.8 TeV*, Phys. Rev. Lett. **80** (1998) 2525.

[80] L3 Collaboration; P. Archard *et al.*, *Search for Single Top Production at LEP* Phys. Lett. **B549** (2002) 290.

[81] H. Jung, *Hard Diffractive Scattering in High Energy ep Collisions and the Monte Carlo Generator RAPGAP*, Comput. Phys. Commun. **86** (1995) 147; See also *http://www.desy.de/~jung/rapgap.html*

[82] G. A. Schuler and H. Spiesberger, *DJANGO: The Interface for the Event Generators HERACLES and LEPTO*, procedings of the workshop *Physics at HERA, Vol. 3*, eds. W. Buchmüller, G. Ingelman, DESY (1991) 1419.

[83] G. Ingelman, J. Rathsman and G. A. Schuler, *AROMA 2.2: A Monte Carlo Generator for Heavy Flavor Events in ep Collisions*, Comput. Phys. Commun. **101** (1997) 135.

[84] H1 Collaboration, *Multi–electron Production at High Transverse Momentum in ep Collisions at HERA*, contributed paper to *The 31st International Conference on High–Energy Physics, Amsterdam 2002*, **Abstract 1019**.

[85] B. Leißner, *Muon Pair Production in Electron–Proton Collisions*, Ph.D. Thesis, RWTH Aachen (2002).

[86] T. Abe *et al.*, *GRAPE–Dilepton (Version 1.0)*, proceedings of the workshop *1998–1999 Monte Carlo Generators for HERA Physics*, eds. A. T. Doyle, G. Grindhammer, G. Ingelman, H. Jung, DESY (1999) 566;
T. Abe, *GRAPE–Dilepton (Version 1.1): A Generator for Dilepton Production in ep Collisions*, Comput. Phys. Commun. **136** (2001) 126.

[87] S. Baranov *et al.*, *LPAIR: A Generator for Lepton Pair Production*, proceedings of the workshop *Physics at HERA, Vol. 3*, eds. W. Buchmüller, G. Ingelman, DESY (1991) 1478;
J. A. M. Vermaseren, *Two Photon Processes at Very High Energies*, Nucl. Phys. **B229** (1983) 347.

[88] H. Jung, *The Monte Carlo Generator EPJPSI for J/ψ Mesons in High Energy Electron Proton Collisions*, proceedings of the workshop *Physics at HERA,*

Vol. 3, eds. W. Buchmüller, G. Ingelman, DESY (1991) 1488;
See also *http://www-h1.desy.de/~jung/epjpsi.html*

[89] A. Mehta, *Z Vertex Determination*, presented talk at H1 HiP Working Group meeting, Hamburg, January 2002.

[90] I. Negri *et al.*, *A Minimal Comprehensive Set of Muon Background Topological Finders for High P_T Physics Analysis*, H1 Internal Note, **H1-IN-498 (10/1996)**;
E. Chabert *et al.*, *QBGFMAR: An Updated Phan Package for Cosmic and Halo Muon Topological Rejection in High P_T Physics Analysis*, H1 Internal Note, **H1-IN-556 (11/1998)**.

[91] A. Schöning, *Untersuchung von Prozessen mit virtuellen und reellen $W^{\pm}$–Bosonen am H1–Detektor bei HERA*, Dissertation, Fachbereich Physik der Universität Hamburg (1996).

[92] F. Keil, *Dijet Production in Charged and Neutral Current e^+p Interactions at High Q^2 at HERA*, Dissertation, Kirchhoff–Institut für Physik, Universität Heidelberg (2001).

[93] J. Rauschenberger, *Prozesse des geladenen Stromes in tief–unelastischer Positron–Proton Streuung bei HERA*, Dissertation, Fachbereich Physik der Universität Hamburg (2002).

[94] A. Baird *et al.*, *A Fast High Resolution Track Trigger for the H1 Experiment*, IEEE Trans. Nucl. Sci. **48** (2001) 1276.

[95] T. Wolff, *Entwicklung, Bau und erste Ergebnisse eines totzeitfreien Spurfinders als Trigger für das H1–Experiment am HERA*, Dissertation, Inst. für Teilchen–physik ETH Zuerich (1993).

[96] C. Wissing, *Fast Track Trigger and its Simulation*, presented talk at Ringberg 2002 Preparatory Meeting, Hamburg, October 2001.

[97] H1 Collaboration, *Addendum to the Proposal "A Fast Track Trigger with High Resolution for H1"*, H1 Internal Note, **H1-IN-576 (09/1999)**.

[98] A. Schöning, *Status of the Fast Track Trigger*, presented talk at the Trigger Plenary, H1 Collaboration Meeting, Hamburg, February 2002.

[99] H1PHAN manual, *version 2.03/11* (1997).

[100] H-C. Schultz–Coulon, *Post–Upgrade Triggering*, presented talk at the Physics Plenary, H1 Collaboration Meeting, Hamburg, February 2002.

[101] Y. Fleming, *An L1 Trigger for a Fast Track Trigger for the H1 Experiment*, Ph.D. Thesis, University of Birmingham (in preparation).

[102] H–C. Schultz–Coulon, Universität Dortmund. *Private communication.*

[103] P. D. Thompson, *The Forward Region*, presented talk at 2nd H1 Ringberg Trigger–Workshop, Ringberg, January 2002.

[104] H1 ToF Group; A. Belgarian *et al.*, *Short Description of the Modifications of the H1 Time–of–Flight System in the Framework of the H1/HERA Upgrade*, (1999).

[105] P. Bruel, *Recherche d'interactions au–delà du Modèle Standard à HERA*, Ph.D. Thesis, Orsay (1998).

[106] H1 Collaboration; C. Adloff *et al.*, *Measurement of Neutral and Charged Current Cross–Sections in Positron–Proton Collisions at Large Momentum Transfer*, Eur. Phys. J. **C13** (2000) 609.

[107] S. Bentvelsen *et al.*, *Reconstruction of (x,Q^2) and Extraction of Structure Functions in Neutral Current Scattering at HERA*, proceedings of the workshop *Physics at HERA, Vol. 1*, eds. W. Buchmüller, G. Ingelman, DESY (1991) 23.

[108] U. Bassler and G. Bernardi, *Some Properties of the Very High Q^2 Events of HERA*, Z. Phys. **C76** (1997) 223.

[109] H1 Collaboration; C. Adloff *et al.*, *Diffractive Dissociation in Photoproduction at HERA*, Z. Phys. **C74** (1997) 221.

[110] S. D. Ellis and D. E. Soper, *Successive Combination Jet Algorithm for Hadron Collisions*, Phys. Rev. **D48** (1993) 3160;
S. Catani *et al.*, *Longitudinally Invariant k(T) Clustering Algorithms for Hadron–Hadron Collisions*, Nucl. Phys. **B406** (1993) 187.

[111] L. Goerlich and H. P. Wellisch, *Documentation of the LAr Clustering*, H1 Internal Note, **H1-IN-204(12/1991)**.

[112] UA2 Collaboration; J. Alitti *et al.*, *An Improved Determination of the Ratio of W and Z Masses at the CERN $\overline{p}p$ Collider*, Phys. Lett. **B276** (1992) 354.

[113] A. Mehta, Liverpool University. *Private communication.*

[114] J. Dingfelder, *Search for Anomalous Production of Single Top Quarks with the H1 Experiment at HERA*, Dissertation, Universität Heidelberg (2003).

[115] C. Diaconu, CPPM Marseille. *Private communication.*

[116] H1 Collaboration; V. Andreev *et al.*, *Observation of Isolated Leptons in Events with Missing P_T and Comparison to Standard Model W Production*, accepted by Phys. Lett. **B**.

[117] ZEUS Collaboration; J. Breitweg *et al.*, *W Production and the Search for Events with an Isolated High–Energy Lepton and Missing Transverse Momentum at HERA*, Phys. Lett. **B471** (2000) 411.

[118] ZEUS Collaboration; J. Breitweg *et al.*, *Search for Events with Isolated High–Energy Leptons and Missing Transverse Momentum at HERA*, contributed

paper to *The 30th International Conference on High–Energy Physics, Osaka 2000*, **Abstract 1041**.

[119] ZEUS Collaboration; S. Chekanov *et al.*, *Search for Single–top Production in ep Collisions at HERA*, (in preparation).

[120] C. Diaconu *et al.*, *High–P_T Leptons and W Production*, J. Phys. **G25** (1999) 1412.

[121] R. Brun and F. Rademakers, *ROOT: An Object Oriented Data Analysis Framework*, NIM, **A389** (1997) 81;
See also *http://root.cern.ch*

[122] M. Rückert, *Diffraktive Elektroproduktion von J/ψ Mesonen in der objekt-orientierten Analyse-Umgebung von H1*, Diploma thesis, Fachbereich Physik der Universität Hamburg (2002);
T. Benisch *et al.*, *New Data Storage Model for H1*, contributed paper to *Computing in High Energy and Nuclear Physics, Padova 2000*, **Abstract C078**.

[123] P. Laycock and D. South, *A Generic OO Framework for Analysis at H1*, (in preparation);
P. Laycock, *A Measurement of the Reduced Diffractive Cross Section $\sigma_r^{D(3)}$ at High Q^2 with the H1 Detector*, Ph.D. Thesis, Liverpool University (in preparation);
M. Beckingham, *Analyses with H1OO*, presented talk at the Physics Plenary, H1 Collaboration Meeting, Lund, October 2002;
D. South, *W analysis in an OO Framework* presented talk at The Crosstalk Workshop–Seminar for H1 PhD and Diploma Students, Hamburg, October 2001;
C. Grab *et al.*, *New Data Analysis Enviroment in H1*, contributed paper to *Computing in High Energy and Nuclear Physics, Padova 2000*, **Abstract F079**.

Appendix A

Event Displays

The 18 data events in the final selection of the results presented in this thesis are illustrated here in chronological order.

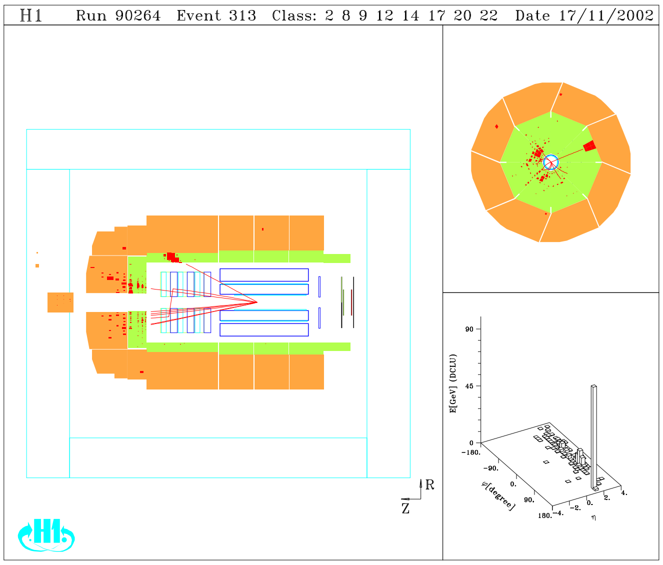

Figure A.1: An electron signal event: Run Number 90264, Event Number 313.

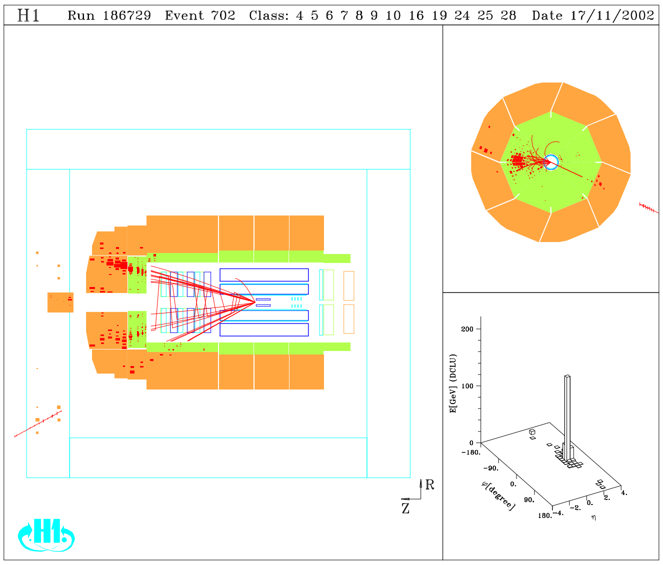

Figure A.2: A muon signal event: Run Number 186729, Event Number 702.

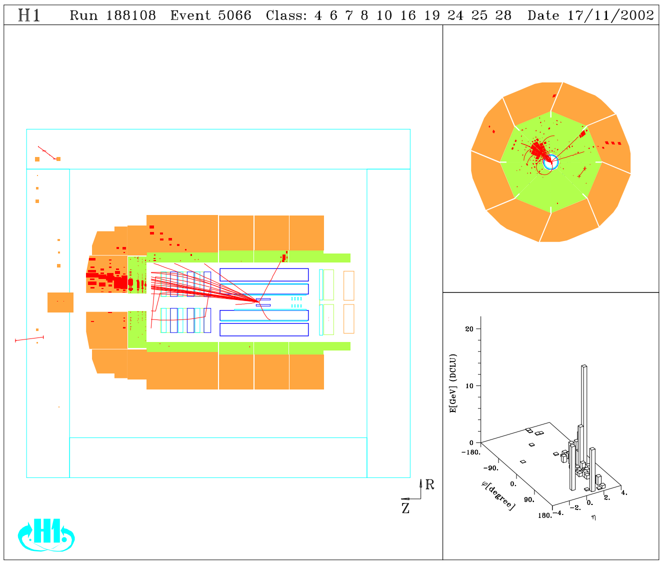

Figure A.3: A muon signal event: Run Number 188108, Event Number 5066.

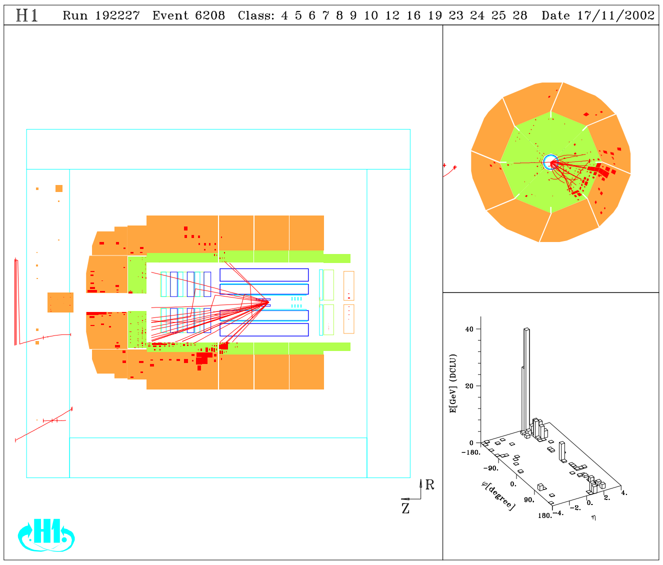

Figure A.4: A muon signal event: Run Number 192227, Event Number 6208.

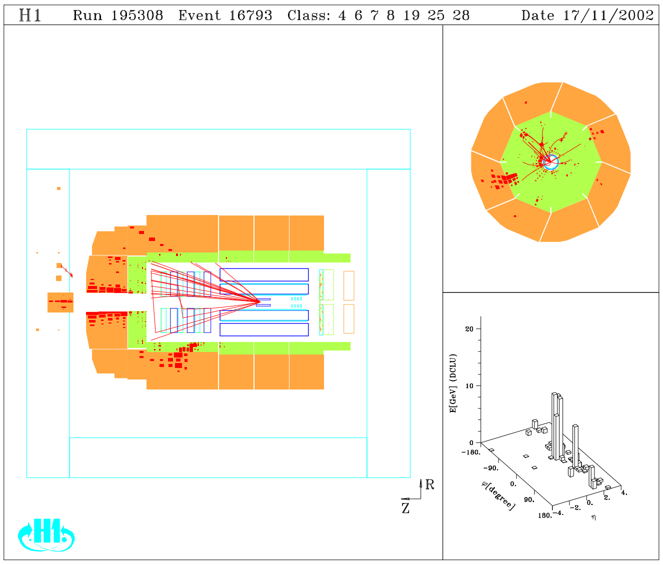

Figure A.5: A muon signal event: Run Number 195308, Event Number 16793.

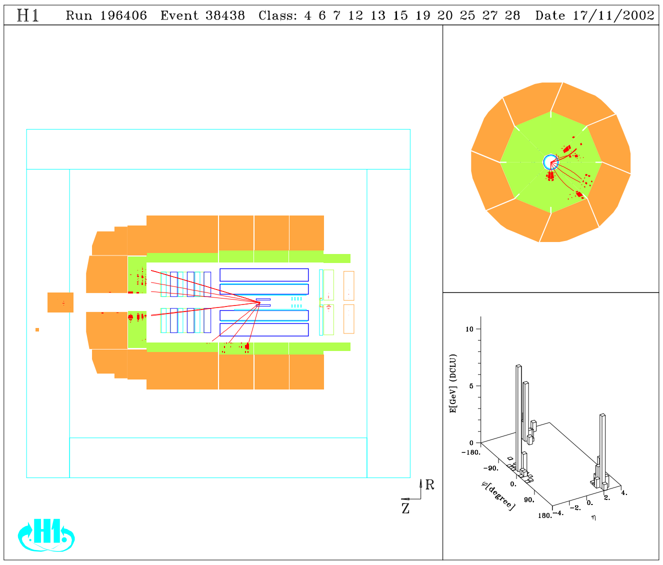

Figure A.6: An electron signal event: Run Number 196406, Event Number 38438.

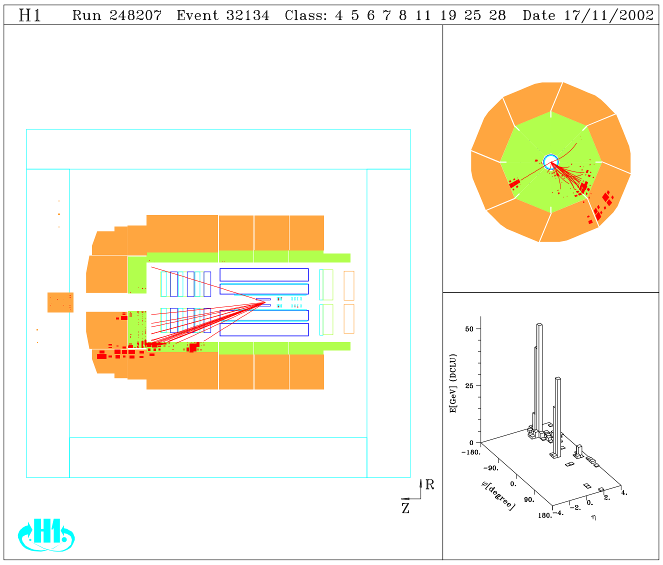

Figure A.7: An electron signal event: Run Number 248207, Event Number 32134.

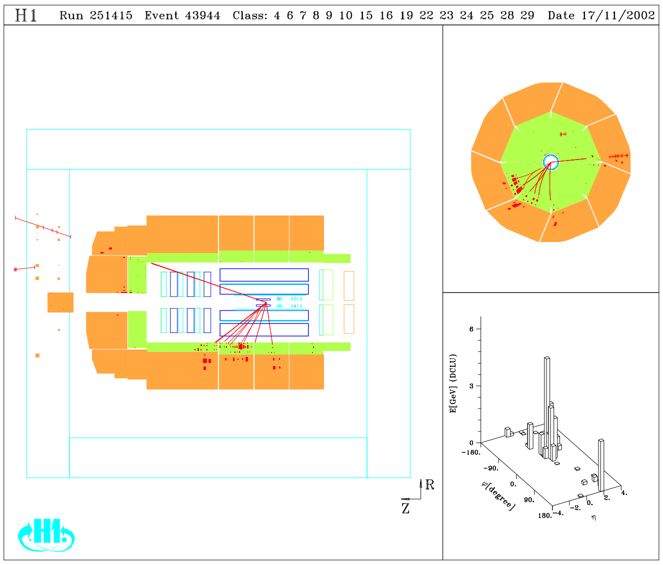

Figure A.8: A muon signal event: Run Number 251415, Event Number 43944.

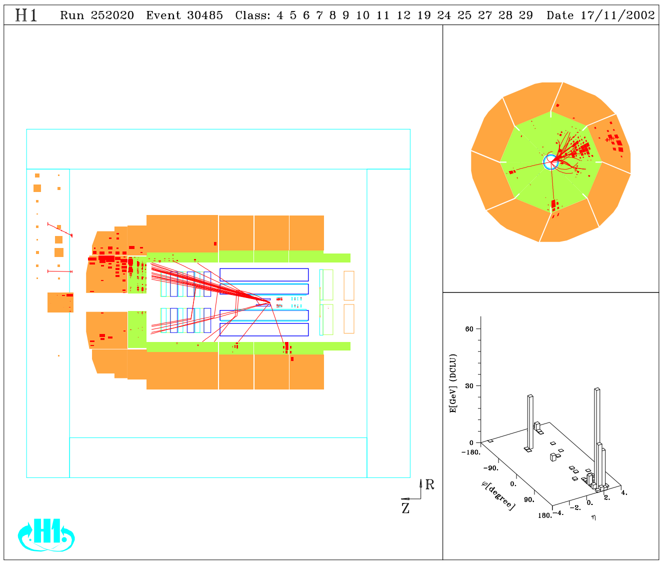

Figure A.9: An electron signal event: Run Number 252020, Event Number 30485.

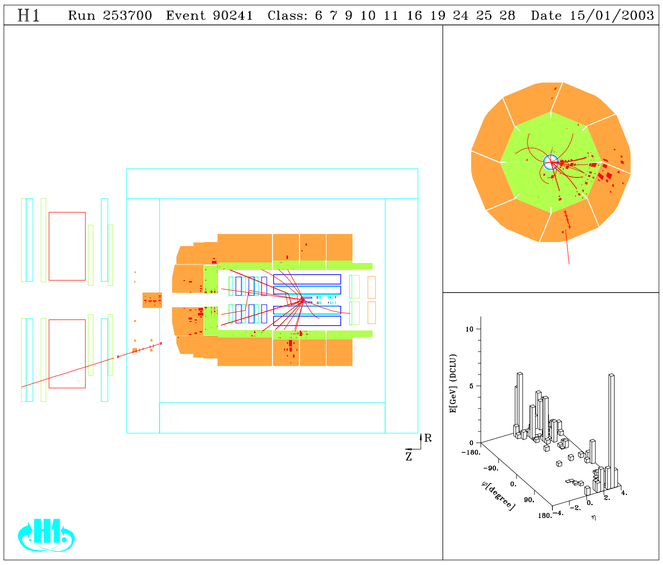

Figure A.10: A muon signal event: Run Number 253700, Event Number 90241.

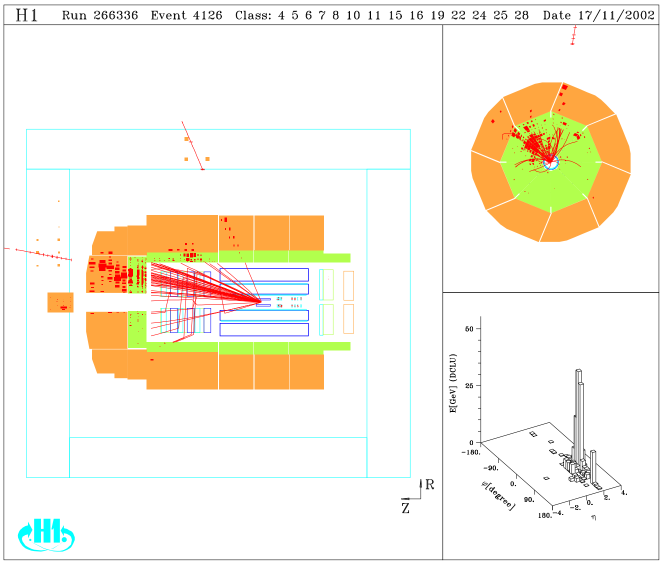

Figure A.11: A muon signal event: Run Number 266336, Event Number 4126.

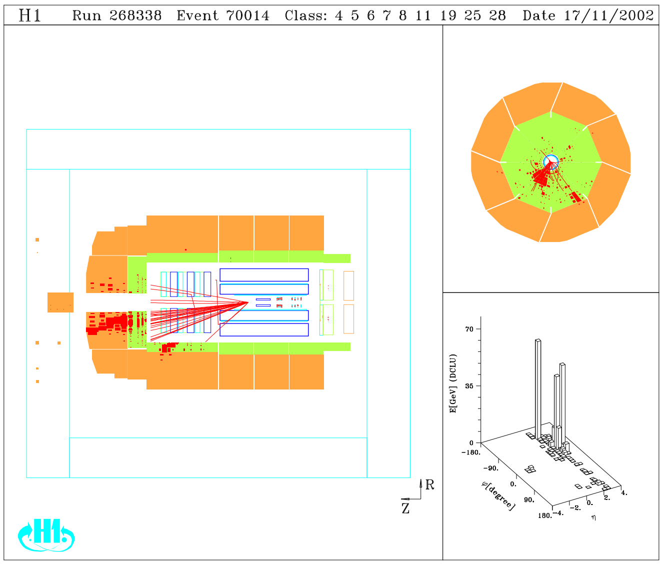

Figure A.12: An electron signal event: Run Number 268338, Event Number 70014.

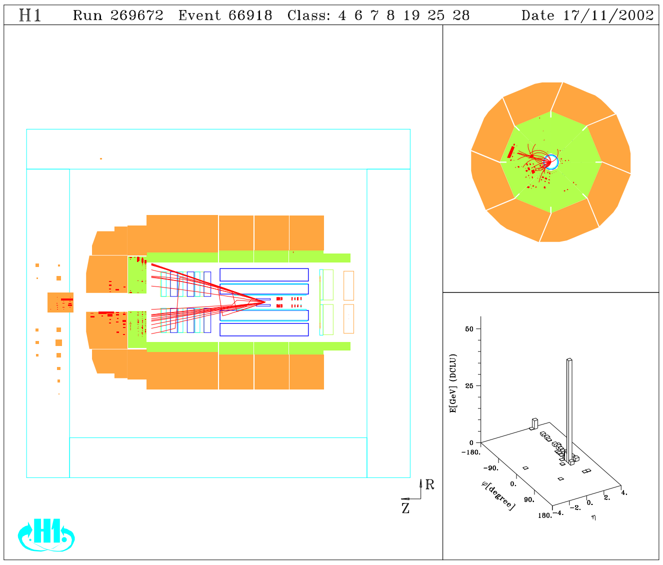

Figure A.13: An electron signal event: Run Number 269672, Event Number 66918.

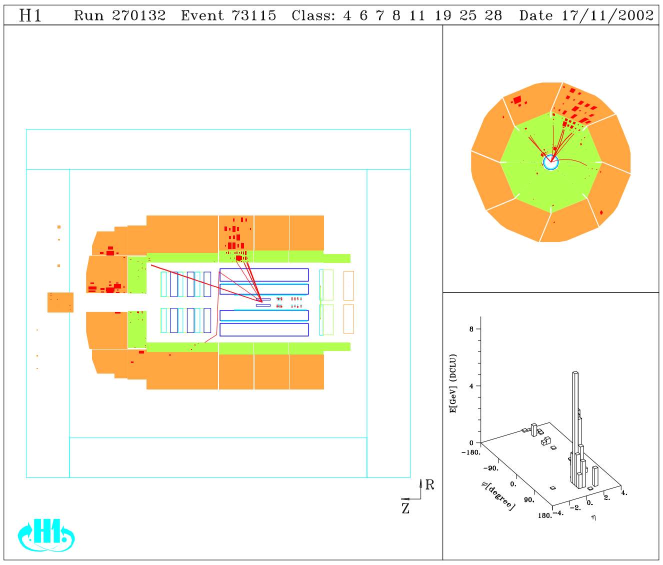

Figure A.14: A muon signal event: Run Number 270132, Event Number 73115.

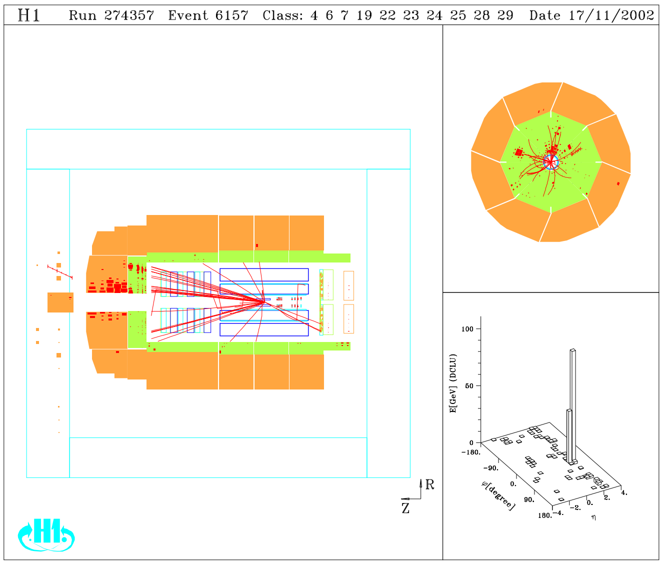

Figure A.15: An electron signal event: Run Number 274357, Event Number 6157.

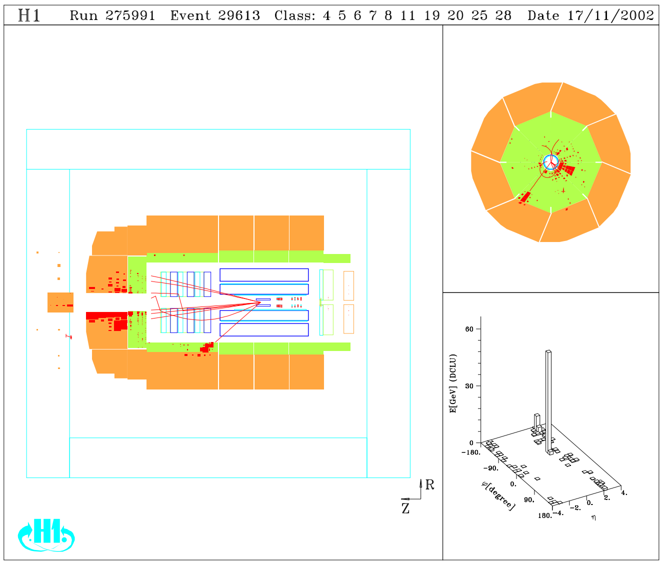

Figure A.16: An electron signal event: Run Number 275991, Event Number 29613.

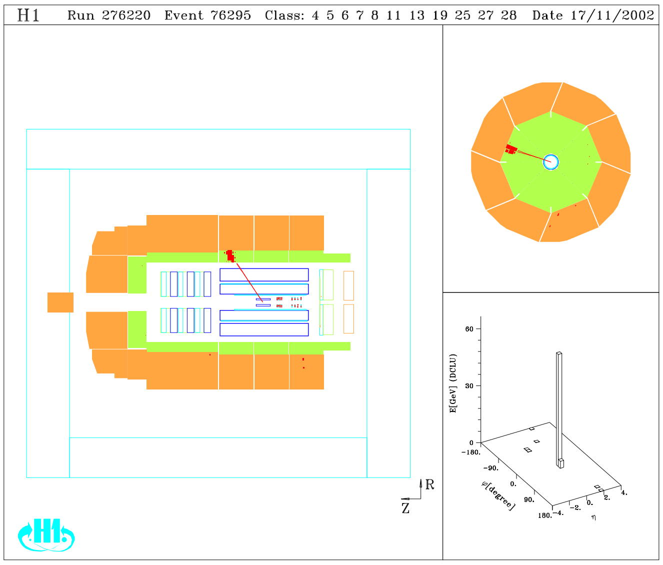

Figure A.17: An electron signal event: Run Number 276220, Event Number 76295.

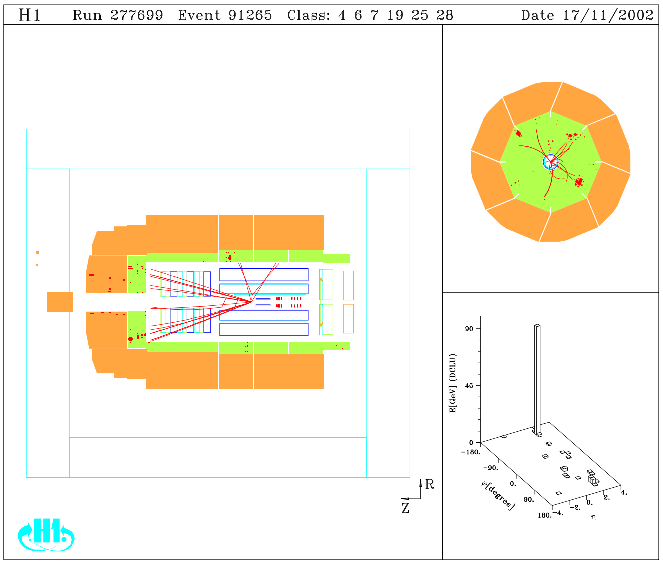

Figure A.18: An electron signal event: Run Number 277699, Event Number 91265.

Appendix B

Tables of Results

Run Event		P_T^l (GeV)	θ_l (°)	ϕ_l (°)	ζ^2 (GeV^2)	P_T^X (GeV)	P_T^{calo} (GeV)	P_T^{miss} (GeV)	γ_h (°)	$\Delta\phi_{l-X}$ (°)	δ_{miss} (GeV)	$M_T^{l\nu}$ (GeV)
90264 313	e^-	$38.9^{+1.4}_{-1.4}$	$27.02^{+0.22}_{-0.22}$	$157.70^{+0.46}_{-0.46}$	8939^{+331}_{-331}	$7.8^{+1.0}_{-1.0}$	$31.7^{+1.7}_{-1.7}$	$32.2^{+1.7}_{-1.7}$	$13.0^{+2.0}_{-2.0}$	$152.9^{+4.9}_{-4.9}$	$45.0^{+0.4}_{-0.4}$	$70.7^{+3.0}_{-3.0}$
186729 702	μ^+	51.2^{+17}_{-10}	$29.83^{+0.26}_{-0.26}$	$-154.65^{+0.09}_{-0.09}$	–	$66.4^{+4.9}_{-4.9}$	$64.5^{+4.9}_{-4.9}$	$28.3^{+7.4}_{-4.9}$	$17.8^{+4.0}_{-4.0}$	$156.4^{+4.8}_{-4.8}$	$31.2^{+4.6}_{-2.8}$	43.7^{+21}_{-13}
188108 5066	μ^-	$41.0^{+5.6}_{-4.4}$	$35.15^{+0.39}_{-0.39}$	$162.54^{+0.06}_{-0.06}$	–	$27.5^{+2.3}_{-2.3}$	$27.8^{+2.3}_{-2.3}$	$45.5^{+4.4}_{-3.5}$	$14.4^{+1.1}_{-1.1}$	$113.8^{+4.8}_{-4.8}$	$27.6^{+2.0}_{-1.6}$	$81.7^{+11}_{-8.3}$
192227 6208	μ^-	$73.1^{+12}_{-9.1}$	$28.58^{+0.26}_{-0.26}$	$-1.71^{+0.09}_{-0.09}$	–	$55.6^{+5.2}_{-5.2}$	$55.6^{+5.2}_{-5.2}$	$25.5^{+8.9}_{-7.1}$	$44.5^{+3.4}_{-3.4}$	$163.4^{+4.8}_{-4.8}$	$13.8^{+3.1}_{-2.4}$	81.4^{+26}_{-20}
195308 16793	μ^+	60.2^{+19}_{-12}	$30.93^{+0.39}_{-0.39}$	$149.01^{+0.06}_{-0.06}$	–	$29.9^{+2.7}_{-2.7}$	$27.5^{+2.7}_{-2.7}$	33.4^{+16}_{-11}	$35.5^{+4.2}_{-4.2}$	$161.0^{+4.8}_{-4.8}$	$29.0^{+5.2}_{-3.2}$	88.8^{+38}_{-24}
196406 38438	e	$14.3^{+0.5}_{-0.5}$	$7.21^{+0.22}_{-0.22}$	$-89.15^{+0.59}_{-0.59}$	12551^{+443}_{-443}	$14.1^{+2.3}_{-2.3}$	$22.9^{+2.0}_{-2.0}$	$23.7^{+2.0}_{-2.0}$	63.4^{+11}_{-11}	$69.6^{+4.9}_{-4.9}$	$21.8^{+1.6}_{-1.6}$	$35.6^{+1.6}_{-1.6}$
248207 32134	e^+	$32.0^{+1.3}_{-1.3}$	$32.41^{+0.25}_{-0.25}$	$-31.00^{+0.30}_{-0.30}$	6082^{+242}_{-242}	$41.3^{+3.9}_{-3.9}$	$43.1^{+2.9}_{-2.9}$	$43.1^{+2.9}_{-2.9}$	$21.1^{+0.6}_{-0.6}$	$109.6^{+4.8}_{-4.8}$	$38.2^{+0.6}_{-0.6}$	$62.8^{+2.3}_{-2.3}$
251415 43944	μ^-	$22.8^{+2.8}_{-2.3}$	$18.75^{+0.20}_{-0.20}$	$174.00^{+0.13}_{-0.13}$	–	$15.9^{+3.0}_{-3.0}$	$15.5^{+3.0}_{-3.0}$	$13.5^{+2.1}_{-1.8}$	$67.2^{+9.3}_{-9.3}$	$144.4^{+4.8}_{-4.8}$	$40.9^{+0.6}_{-0.5}$	$32.6^{+5.7}_{-4.8}$
252020 30485	e^+	$25.6^{+1.3}_{-1.3}$	$110.10^{+0.25}_{-0.25}$	$-94.36^{+0.30}_{-0.30}$	987^{+48}_{-48}	$44.9^{+3.7}_{-3.7}$	$40.8^{+3.1}_{-3.1}$	$42.3^{+3.1}_{-3.1}$	$21.2^{+1.3}_{-1.3}$	$113.1^{+4.8}_{-4.8}$	$10.2^{+1.8}_{-1.8}$	$50.9^{+2.2}_{-2.2}$
253700 90241	μ^+	161.8^{+85}_{-43}	$16.96^{+0.20}_{-0.20}$	$-102.23^{+0.13}_{-0.13}$	–	$21.3^{+2.8}_{-2.8}$	$21.1^{+2.8}_{-2.8}$	172.9^{+85}_{-43}	$63.3^{+8.8}_{-8.8}$	$61.8^{+4.8}_{-4.8}$	$17.9^{+53}_{-6.4}$	334.1^{+171}_{-85}
266336 4126	μ^+	$19.7^{+0.8}_{-0.7}$	$67.35^{+0.39}_{-0.39}$	$101.95^{+0.06}_{-0.06}$	–	$52.1^{+4.1}_{-4.1}$	$50.1^{+4.1}_{-4.1}$	$68.4^{+4.0}_{-4.0}$	$21.0^{+1.3}_{-1.3}$	$50.3^{+4.8}_{-4.8}$	$31.7^{+0.6}_{-0.5}$	$70.3^{+2.6}_{-2.5}$
268338 70014	e^+	$31.6^{+1.2}_{-1.2}$	$29.57^{+0.22}_{-0.22}$	$-124.90^{+0.46}_{-0.46}$	6661^{+260}_{-260}	$45.5^{+3.2}_{-3.2}$	$63.1^{+3.1}_{-3.1}$	$65.7^{+3.1}_{-3.1}$	$20.2^{+1.7}_{-1.7}$	$39.7^{+4.9}_{-4.9}$	$38.5^{+0.3}_{-0.3}$	$86.2^{+2.9}_{-2.9}$
269672 66918	e	$17.5^{+0.7}_{-0.7}$	$18.76^{+0.22}_{-0.22}$	$14.49^{+0.59}_{-0.59}$	5837^{+236}_{-236}	$3.8^{+0.5}_{-0.5}$	$19.0^{+0.7}_{-0.7}$	$19.3^{+0.7}_{-0.7}$	$21.7^{+7.0}_{-7.0}$	$14.6^{+4.9}_{-4.9}$	$51.6^{+0.2}_{-0.2}$	$36.6^{+1.4}_{-1.4}$
270132 73115	μ	64.0^{+101}_{-37}	$18.46^{+0.20}_{-0.20}$	$48.34^{+0.13}_{-0.13}$	–	$27.2^{+3.9}_{-3.9}$	$27.5^{+3.9}_{-3.9}$	78.8^{+101}_{-35}	$66.3^{+7.2}_{-7.2}$	$66.7^{+4.8}_{-4.8}$	27.0^{+420}_{-30}	140.2^{+204}_{-75}
274357 6157	e	$40.4^{+1.4}_{-1.4}$	$15.03^{+0.22}_{-0.22}$	$15.93^{+0.59}_{-0.59}$	16889^{+575}_{-575}	$6.2^{+0.7}_{-0.7}$	$39.5^{+1.4}_{-1.4}$	$38.7^{+1.4}_{-1.4}$	$134.5^{+6.6}_{-6.6}$	$109.5^{+4.9}_{-4.9}$	$35.0^{+1.6}_{-1.6}$	$78.9^{+2.7}_{-2.7}$
275991 29613	e^+	$37.8^{+1.5}_{-1.5}$	$41.76^{+0.25}_{-0.25}$	$-53.23^{+0.30}_{-0.30}$	5467^{+219}_{-219}	$26.9^{+1.8}_{-1.8}$	$40.0^{+1.4}_{-1.4}$	$40.7^{+1.4}_{-1.4}$	$6.9^{+0.4}_{-0.4}$	$104.6^{+4.8}_{-4.8}$	$28.3^{+1.1}_{-1.1}$	$73.7^{+2.9}_{-2.9}$
276220 76295	e^-	$52.2^{+2.0}_{-2.0}$	$55.13^{+0.25}_{-0.25}$	$18.30^{+0.30}_{-0.30}$	5525^{+216}_{-216}	$0.0^{+0.0}_{-0.0}$	$52.2^{+2.0}_{-2.0}$	$52.2^{+2.0}_{-2.0}$	$0.0^{+0.0}_{-0.0}$	$0.0^{+0.0}_{-0.0}$	$27.9^{+1.1}_{-1.1}$	$104.5^{+4.1}_{-4.1}$
277699 91265	e	$28.2^{+1.0}_{-1.0}$	$17.56^{+0.22}_{-0.22}$	$-143.90^{+0.59}_{-0.59}$	10059^{+367}_{-367}	$3.7^{+0.8}_{-0.8}$	$25.8^{+1.3}_{-1.3}$	$24.8^{+1.3}_{-1.3}$	101.1^{+19}_{-19}	$151.8^{+4.9}_{-4.9}$	$46.4^{+0.8}_{-0.8}$	$52.8^{+2.2}_{-2.2}$

Table B.1: The main kinematic properties of the 18 events in the final selection. The quoted errors are the resolution and systematic errors combined in quadrature. The charge of the isolated lepton is also displayed, determined from the curvature of the track. The charge of electrons produced in the forward region is not measured due to the electron showering in the tracking detectors (see section 6.1.1). The kinematic quantity ζ^2 (see section 6.3.3) is only relevant to electron events.

P_T^X (GeV)	σ (pb)	δ_{stat} [%]	δ_{sys} [%]	δ_{tot} [%]	δ_{E_e} [%]	δ_{θ_e} [%]	δ_{ϕ_e} [%]	δ_{ε_e} [%]	δ_{E_μ} [%]	δ_{θ_μ} [%]	δ_{ϕ_μ} [%]	δ_{ε_μ} [%]	δ_{E_h} [%]	δ_{γ_h} [%]	δ_{ϕ_h} [%]	$\delta_{\frac{V_{ap}}{V_p}}$ [%]	δ_{trig} [%]	$\delta_{\varepsilon_{tr}}$ [%]	δ_{lumi} [%]	δ_{model} [%]	δ_{bg} [%]
< 25	0.141	57.8	19.6	61.0	0.99	0.03	0.01	1.79	0.10	0.00	0.03	0.63	1.08	2.33	0.05	0.89	0.61	3.00	1.50	10.0	16.2
> 25	0.166	33.0	16.8	37.0	0.39	0.14	0.01	1.02	0.49	0.01	0.10	2.94	5.80	11.1	0.03	0.94	1.66	3.00	1.50	10.0	1.20
Total	0.308	32.0	13.3	34.6	0.88	0.05	0.01	1.65	0.17	0.00	0.04	1.05	0.18	0.14	0.05	0.89	0.80	3.00	1.50	10.0	7.69

Table B.2: The measured cross section for signal events, calculated in the kinematical region defined in table 9.6 and at $\sqrt{\mathrm{s}} = 312$ GeV, with the corresponding statistical error (δ_{stat}), systematic error (δ_{sys}) and total error (δ_{tot}). Also given are the individual contributions to the systematic error from the experimental uncertainties described in section 9.1: the electron energy scale (δ_{E_e}), the electron polar angle (δ_{θ_e}), the electron azimuthal angle (δ_{ϕ_e}), the electron identification efficiency (δ_{ε_e}), the muon energy scale (δ_{E_μ}), the muon polar angle (δ_{θ_μ}), the muon azimuthal angle (δ_{ϕ_μ}), the muon identification efficiency (δ_{ε_μ}), the hadronic energy scale (δ_{E_h}), the hadronic polar angle (δ_{γ_h}), the hadronic azimuthal angle (δ_{ϕ_h}), the ratio $\frac{V_{ap}}{V_p}$ ($\delta_{\frac{V_{ap}}{V_p}}$), the trigger efficiency (δ_{trig}), the track-cluster link requirement ($\delta_{\varepsilon_{tr}}$) and the luminosity uncertainty (δ_{lumi}). The model uncertainty is given by δ_{model}. The statistical and systematic uncertainty on the background contribution to the cross section are given by δ_{bg} and included in the total systematic error.

Appendix C

Analysis Comparisons

The analysis described throughout this thesis has been performed using the new H1OO software environment based on the analysis package `ROOT` [121] and written in the `C++` programming language. The analysis framework consists of a new data storage system [122] and a series of generic analysis packages [123]. The results presented in this thesis have provided an important cross-check to those recently published by H1 [116]. The main results of the two analyses are compared below.

The results of the final event selection as reported in [116] are presented in table C.1, which may be compared directly to table 9.5. All numbers agree very well, at a much higher precision than the quoted total errors. Only the expectation from other SM processes in the lowest P_T^X bin exhibits a significant difference, which is mainly due to the photoproduction reweight performed as described in section 6.4. The measured cross section reported in [116] of 0.31 $\pm$ 0.10 $\pm$ 0.04 pb also agrees very well with the cross section measured by this analysis, which is detailed in table 9.7. The predicted cross section from the SM expecation of each analysis is identical.

The new data storage model and analysis framework employed by this analysis is independent of the structure used in [116] above the DST level (see section 2.8). The level of agreement of the two analyses not only verifies the results presented in [116], but also provides a measure of the success of the H1OO project.

P_T^X (GeV)	Data	SM Expectation	Signal	Other SM processes
< 12	5	6.40 ± 0.79	4.45 ± 0.70	1.95 ± 0.36
12 - 25	3	3.08 ± 0.43	2.40 ± 0.40	0.68 ± 0.14
25 - 40	4	1.83 ± 0.27	1.59 ± 0.26	0.24 ± 0.06
> 40	6	1.08 ± 0.22	0.96 ± 0.22	0.12 ± 0.04
Total	18	12.40 ± 1.69	9.40 ± 1.60	3.00 ± 0.53

Table C.1: Observed and predicted event rates in the combined (electron and muon) final selection in bins of P_T^X for the complete HERA I e^+p H1 data set from the analysis published in [116]. Presented are the observed data events, the total expectation from all SM processes, and the prediction from the signal and background components. Also given are the total errors (statistical and systematic) combined in quadrature.

Appendix D

Probability Calculations

Probability calculations are performed for a given number of observed events, compared with an expectation both with and without the associated uncertainty on the expectation. Poisson statistics are assumed to be a good approximation in cases where the expectation is less than 20 events (as is the case in this analysis).

The probabability calculated is defined as that of an expectation N_{Exp} fluctuating up to equal or more than an observation N_{Obs}. This probability may be calculated in the two cases of including and ignoring the uncertainty σ_{Exp} on N_{Exp}.

The probability without the uncertainty is defined as:

$$\mathcal{P}_{\mathcal{WO}} = 1 - e^{-N_{Exp}} \sum_{i=0}^{N_{Obs}-1} \frac{N_{Exp}^{i}}{i!} \tag{D.1}$$

The probability with the uncertainty is defined as:

$$\mathcal{P}_{\mathcal{W}} = \int_{N_{Exp}-3\sigma_{Exp}}^{N_{Exp}+3\sigma_{Exp}} \mathcal{P}_{\mathcal{WO}}(x) \frac{1}{\sqrt{2\pi}\sigma_{Exp}} e^{\frac{(x-N_{Exp})^2}{2\sigma_{Exp}^2}} dx \tag{D.2}$$

Acknowledgements

Firstly, I would like to thank my supervisor Robin Marshall for not only providing me with advice and support throughout my Ph.D but also giving me the freedom to pursue the analysis of my choice. I'd also like to thank Fred Loebinger and Keith Stephens for their encouragement and enthusiasm during my time in Manchester.

Special thanks go to Nick Malden and Andrew Mehta. Much of this work would not have been possible without their expert knowledge of the analysis. I am also grateful to Nick for proof reading this thesis countless times, especially the anlaysis [sic] discussion.

Many other people have spent time helping me with various facets of the analysis: Paul Laycock in particular deserves a mention, especially for all things OO; Paul Newman for his advice on the FTT and other things more general; André Schöning and Hans-Cristian Schultz–Coulon for their useful trigger discussions; Eckhard Elsen for spending the time when he probably didn't have it; Terry Sloan for his help with the resolution errors by providing me with an old software routine with a rather curious name; Christian Schwanenberger for his time and patience when discussing the NLO corrections; Cristi Diaconu and Mireille Schneider for their efforts to answer all my questions and finally Christian Veelken for steering me in the right direction at the bitter end.

There are many people from H1 and the other place who have made Hamburg a fun place to live over the last three years. In particular, I would like to thank Matthew Beckingham, Stewart Boogert, James Ferrando, Yves Fleming, Claire Gwenlan, Steve Hanlon, Eileen Heaphy, Beate Heinemann, Oliver Henshaw, John Kennedy, John Loizides, Matt Lightwood, Eram Rizvi, Steve Robins, Mark Sutton, Alex Tapper, Paul Thompson, Jon Turney, Rod Walker, Ben Waugh, Nicole Werner, Matt Wing, Ethan Woehrling and Angela Wyatt.

In Ottensen and beyond: Carmen, Michael, Sophie and everyone else at the Innsbeth, Jenny and all at the Aurel, Jannine at the Blaues Haus, Laura at Kick & Company, Andy and Eve at Murphys, Mike and Tanya at Titanic and finally Audrey, Bart, Kenny, Paul and countless others at Finnegans Wake.

Many thanks to all of my friends in the UK, in particular Charles Filtness, John Levon, Jon Wakely, Paul Wright and those back home in Morpeth: Ed Copeland, Oliver Court, Matt Forster, Clare Hargreaves, Katie McBryde, Andrew McCarthy, David McKenna, Heather Wade, Steven Ward and everyone else who has kept in touch over the last few years. Thanks also to Steven Patrick and Jason Pierce for providing inspiration when it was needed.

To Andrea, for having an endless amount of love, patience and understanding. Danke Kleine, ich liebe dich ganz doll. x

Finally, thanks to my parents for their constant support throughout my schooling and to Vera Harrison, my grandmother, to whom this thesis is dedicated for starting me off on this road many years ago.